SAPIENZA
UNIVERSITÀ DI ROMA

Doctoral course in Aeronautical and Space Engineering

Department of Mechanical and Aerospace Engineering

32nd Cycle

Doctoral Thesis

Development of nanocomposite coatings for spacecraft components

Coordinator:	**Ph.D. candidate:**
Prof. Mauro Valorani	Marialaura Clausi

Tutor:

Dr. Susanna Laurenzi

Co-tutor:

Dr. Maria Gabriella Santonicola

Table of Contents

<u>Chapter 3</u> - *Spray coating process of MWCNT/epoxy nanocomposite films for aerospace applications: effects of process parameters on surface electrical properties*……………………………………………………...71

<u>Chapter 6</u> - *Hydrophobic multi-layered graphene-based nanocomposite films spray-coated on textured aluminum substrate with high thermal conductivity*……..…......................................157

Aknowledgements

I would first like to thank my parents for supporting my decisions and supporting me while I attained by goals and all of the friends who’ve come and gone throughout my years of PhD course.

My advisor Dr. Susanna Laurenzi and co-advisor Dr. Maria Gabriella Santonicola have also guided and helped me through the years of my PhD work.

I would like to thank Prof. Valeria La Saponara for giving me the opportunity to join her laboratory ACRES at the University of California Davis and work on an exciting project that is beneficial to existing NASA grant.

I would also like to acknowledge Dr. Antonia Simone and Eng. Marco Nebiolo that gave me the opportunity to continue my PhD research at Thales Alenia Space in Turin.

And last but not least, I am also thankful to Dr. Ilker Bayer and Dr. Athanassia Athanassiou for offering me the work opportunity in Italian Institute of Technology (iit) in Genoa and leading me working on different exciting projects.

Introduction

Space is known as a very aggressive and hostile environment and its effects on spacecrafts can compromise the success of the entire mission. During last decades, the degradative effects on the spacecraft materials were studied and carefully measured in order to find solutions to protect or isolate the spacecraft components from the operating environment without however compromising its operation.

A few types of space weather impacts on spacecrafts have been detected and the main ones are for example: space-plasma that causes surface charging on the structures with consequently biasing of instrument and physical damages; microparticles and space debris which can cause abrasions on surfaces and structural damages; UV radiation, galactic cosmic rays and solar particle events that lead to a thermal, electrical, optical and structural integrity degradation of materials and many damages in the electronic components; large gradients of temperature when, for example, space vehicles are illuminated or not by sunlight lead to a degradation of polymeric materials as well as the presence of atomic oxygen, especially in LEO orbit, that corrodes the exposed polymeric material surfaces [1-4].

It is therefore necessary to provide and find solution to protect and properly isolate the spacecraft components from the external space environment. Multifunctional coatings could play a key-role in protecting and safeguarding the various spacecraft components, of different nature, from the surrounding environment.

For example, one of the major technical challenges in telecommunication satellites is to maintain different equipment working in different bands uncontaminated by neighboring antennas, feeds, and thermal hardware such as multi-layer insulation (MLI). It is a known [5, 6] fact that MLI causes unwanted interference and even passive intermodulation products problems due to its high radio frequency reflectivity (RF) in the specular direction. Usually, in the RF design of antenna payloads, this is accounted for by representing the MLI as a perfectly flat conducting ground plane (this is the standard practice in the industry). In reality, the MLI is not a perfectly flat surface and in some cases the outer layer is perforated to allow for venting of the MLI during ascent. The perforation pattern works as a frequency selective surface and it may be the cause of passive intermodulation products. In such cases, this is avoided by having the outer layer unperforated, and therefore venting has to be achieved in another location. In addition to this unwanted effect in the antenna performance, thermal blankets may also originate passive intermodulation products. Passive intermodulation products are caused as the MLI is illuminated by several antennas that may be even operating in multiple bands and with high power.

The nonlinear nature of the MLI details, such as its shape, finishing details, grounding hardware and perforation patterns, as well as the nonlinear response of metallic contact points, contribute to passive intermodulation products. This continues to be a significant risk for advanced communication satellites: the measurements made at ESA High Power RF Laboratory in Valencia in 2010 for Alphasat mission showed that little or nothing can be done in terms of design and manufacturing methods to reduce the MLI RF reflectivity. For these reasons, ESA has recently funded research projects (Artes 5.1 and 5.2) to find a solution for this problem. One of the most promising concepts is the use of frequency selective surfaces as layers of the MLI [7]. This is accomplished by using nanostructured carbon-based films on membranes, which can also improve the protection of the payload by the MLI (and in general by flexible membranes) with respect to space radiations and impact events.

Nowadays, technological developments, in the field of ultralight structures, have provided new possibilities for obtaining answers to the need for large-scale structures in low-cost and low-weight space, alternatives to traditional deployment systems, by developing for example Gossamer structures. Recently, NASA-LaRC developed, with a view to Gossamer deployment, novel polyimide films reinforced with a small amount of SWNTs to enhance its electrical conductivity with the aim to mitigate electrostatic charge build-up on the polymeric films in-orbit [8].

Multifunctional films containing carbon nanoparticles are currently investigated also to create sensors for monitoring the radiation absorbed by astronauts during extra vehicular activities (EVA) [9-11] or as new and advanced grounding systems to mitigate plasma-induced spacecrafts charging [12].

In addition, these films could be useful in interplanetary missions in which solar sail thrust propulsion can be enhanced using carbon nanotubes (CNTs) as photonic materials in the back side of the polymer membrane [11, 13]. Further novel space-based applications of carbon-based multifunctional films are future membrane reflector spacecraft. These ones are a promising key technology to deliver cost-effective space-based applications such as communication antennae, optical telescopes and solar energy collectors.

The main objectives of my Ph.D. research are to design and realize carbon-based nanocomposite coatings with tailored multifunctional properties for spacecraft components. The research was focused on the development and design of nanocomposite films containing carbon nanoparticles, namely carbon nanotubes and graphene nanoplatelets, which have unique multifunctional properties, with the aim, on one side, to protect and safeguard the various spacecraft components from the surrounding hostile space environment, especially from ultraviolet UV-C radiation and electrically charged particles coming from space-plasma, and on the other side to increase the heat transfer coefficients, thanks to the application of efficient nanocomposite coatings, improving so the energy efficiency of heat exchangers widely used in the aerospace field to control, for example, the temperature of on-board electronic components.

The development of polymeric nanocomposites films with tailored excellent and multifunctional mechanical, electrical, thermal and hydrophobic properties depends on the properties and geometrical features of the nanofillers, CNTs or graphene, their grade of dispersion within the polymeric matrix as nano-reinforcements, their interaction with the polymeric matrix and the alignment of the nanofillers in the matrix [14, 15] as well as the fabrication process of films. For these reasons, the definition of the carbon nanoparticles and their concentration in the polymer matrix, in order to optimize the multifunctional properties of the film, was an important preliminary step of my PhD research. The selection of the carbon nanotubes (SWCNTs and MWCNTs), graphene nanoplatelets or a hybrid of both, in terms of functionalization and structure, was established in order to find an optimal balance among all the required multifunctional properties, and the fabrication aspects.

After that, the selected carbon nanoparticles were added to different types of aerospace-grade polymer matrices at several concentrations. Nanocomposite films will be fabricated on different types of substrates like Mylar sheets, carbon-fibers reinforced polymer (CFRP) composite laminates or metal substrates that are widely used in spacecraft sub-systems.

An important step was, also, the optimization of the nanoparticles dispersion in the polymer matrices since the performance of final nanocomposite films is strictly related to this aspect. In fact, the most common problem encountered in reinforcing a polymer matrix by carbon nanoparticles is to obtain a homogeneous dispersion avoiding agglomerate structures that can act as localized defect points. What makes nanoparticle dispersion extremely difficult is their large specific surface area and large aspect ratio. In addition, for carbon nanoparticles their mutual attraction due to van der Waals forces drives their aggregation into clusters, even after using mechanical disentanglement processes during fabrication. In order to overcome these problems, different approaches and dispersion technique have been developed.

Different deposition processes of the fabricated nanocomposite films were investigated with the aim to study the effects of the different process parameters on the multifunctional properties of the film. In this context, also different deposition techniques were studied, investigated and optimizated for the fabrication of multifunctional films on a large scale for potential uses in real space applications.

In particular, my PhD research can be subdivided in 5 main research activities:

1. Analysis of UV-C effects on the surface properties of epoxy/graphene nanocomposite films on Mylar substrate

During space missions, aerospace components are continuously exposed to radiations, which can degrade their optical, electrical, thermal and structural performance or permanently damage them. In particular, polymer-based materials in space exhibit larger degradation effects due to the combination of energetic UV radiations, vacuum, atomic oxygen, as well as large temperature gradients, which degrade their multifunctional properties. The possibility to deposit carbon-based nanocomposite coatings on polymer-based membranes is currently investigated with the aim to protect the surfaces, by exploiting the excellent properties of carbon nanomaterials, by space environmental exposure, including UV radiations.

The main objective of this work is to investigate the effects of space-abundant UV-C radiation on carbon-based nanocomposite films deposited on flexible Mylar substrates. The choice of Mylar, which is already widely used in spacecraft sub-systems (e.g. MLI for satellites, electrostatic shells for equipment, Gossamer structures), will allow to directly test applications of the carbon nanocomposite flexible membrane in spacecraft vehicles.

For this study, we fabricated nanocomposite films with different types of graphene nanoparticles embedded in epoxy resin by spin-coating process following our previous investigations [16]. Finally, the effects of UV-C exposure on the different types of nanocomposite film samples were investigated in terms of surface electrical properties and surface hydrophobicity/hydrophilicity, which is a relevant parameter to assess the level of moisture absorption by the films.

2. *Spray coating process of MWCNT/epoxy nanocomposite films for aerospace applications: effects of process parameters on surface electrical properties*

Nanocomposite coatings on flexible membranes possess many interesting properties useful in aerospace applications, such as thermal blankets and charging mitigation layers. However, their fabrication is not trivial and the overall performance is strongly dependent on the manufacturing process, since it influences the filler distribution and so the homogeneity of the coated film. The main objective of this research is to study the spray coating deposition process and to investigate the role of its working parameters in setting the morphology and the electrical performance of MWCNT-based nanocomposite films.

It was chosen a flexible Mylar membrane as substrate for the nanocomposites because, as above-mentioned, it is largely used in many spacecraft subsystems [17-19] (Gossamer structures, MLI etc.). In particular the fabrication of uniformly electrically-conductive coatings on Mylar substrate can allow the mitigation of electromagnetic interferences [20] and charging [21], that are problems related to the dielectric nature of MLI, including Mylar, which are a serious risk for the spacecraft operation and integrity. In this context, exploiting the well-known electromagnetic absorption and electrical conductive properties of CNT-based material [22], MWCNT-based nanocomposite films were fabricated on Mylar membrane, with the possibility to be easily integrated with MLIs.

The air spraying was investigated, so, in order to fabricate multifunctional coatings on a large scale for potential uses in real space applications and to understand how the different parameters influence the range and quality of the deposited nanocomposite coatings. Finally, the morphological and electrical properties of the deposited nanocomposite films on Mylar substrate are investigated in relation to the spraying process parameters.

3. Design of nanocomposite coatings by bar-coating process on CFRP structures for electrostatic charging mitigation for spacecraft

In this study, the effects of UV-C radiations, high humidity level and thermal gradients were investigated on the electrical properties of carbon nanofillers (CNT, GNP) /epoxy resin coatings realized on carbon fiber/epoxy resin composite laminate (CFRP) substrates, which are typically used in the aeronautical and space fields. In particular, the fabrication of uniformly electrically-conductive coatings can allow the mitigation of ESC buid-up and/or provide paths with low DC-electrical resistance to units positioned on structures that could be not or partially conductive with the aim to realize new and innovative advanced grounding systems to mitigate plasma-induced spacecrafts charging. Typically, in telecommunication satellites are used metallic ground plane or aluminum grounding rails on CFRP to provide a common electrical grounding to all conductive components to minimize potential differences between them [23]. The drawback is that they are heavy and bulky, not meeting so the needs of mass, volume and energy saving. In this context carbon-based nanocomposite films fabricated on CFRP represent a tempting solution, because of the well-known electrical conductive properties of carbon-based materials, to provide high electrically-conducive paths with weight saving [12, 23].

In this work, nanocomposite films, with different concentrations, different types of carbon nanoparticles and also with hybrid network of CNTs and GnPs, were fabricated on CFRP by bar coating process. Thermo-analysis will be performed to evaluate the effects of carbon nanofillers (CNT, GNP) on thermal properties of final nanocomposites. The addition of nanofillers to a polymer matrix greatly affects the polymerization phase in terms of kinetics and glass transition temperature, so this aspect must be studied. As the polymerization grade is strictly related to the stiffness of the polymer, thermo-analysis have helped to set the process parameters. The coatings were irradiated at given UV-C dose, subjected to humidity and thermal cycles and electrical surface and volume conductivities were performed on untreated and irradiated/aged samples.

4. Direct effects of UV irradiation on the developed graphene-based nanocomposite coating sensors revealed by electrical resistance tomography (ERT)

In this research activity, it was investigated and exploited the electrical resistance tomography (ERT) technique to identify the damaging effects of UV-C radiation on fabricated graphene nanoplatelets (GnPs)/ deoxyribonucleic acid component in a poly(3,4-ethylene dioxythiophene):poly(styrene sulfonate) (DNA-PEDOT:PSS) nanocomposite coatings applied on carbon fiber/epoxy (CFRP) laminates, which are composite structures that are typically used in the aerospace field. The DNA-functionalized GNPs were chosen for their sensitivity to UV radiation, and the PEDOT:PSS matrix was selected to enhance the electrical conductivity of the overall nanocomposite.

It was fabricated a 16-electrode scheme, as required by ERT technique, and it was applied along the edges of the nanocomposite sensor coatings. The maps of electrical conductivity changes, after UV-C irradiation on nanocomposite sensors, were reconstructed (ERT analysis and image reconstruction) through the code developed using open-source MATLAB-based software suite Electrical Impedance Tomography and Diffuse Optical Tomography Reconstruction Software (EIDORS).

This is the first report of the application of the ERT technique to the detection of surface conductivity changes induced by UV exposure. This technique in combination with the UV-sensitive coatings containing DNA-functionalized graphene can provide a health monitoring method for composite materials and structures that are exposed to damaging levels of UV radiation.

5. Hydrophobic multi-layered graphene-based nanocomposite films spray-coated on textured aluminum substrate with high thermal conductivity to improve the efficiency of thermal power generation

The main objective of this work is to fabricate promising hydrophobic graphene-based nanocomposite films on aluminum substrate with high thermal conductivity and evaluate the effects of thermal annealing on its surface hydrophobicity and thermal properties that are relevant parameters to improving the efficiency of thermal power generation. Aluminum was chosen as substrate for the nanocomposite films as it is a metal largely used in several industrial sectors, as well as the aerospace one, especially in the heat exchangers [24]. The long-term vision is to develop solutions related to the use of water for a significant improvement in terms of efficiency of thermal energy generation and water collection for its possible re-use. The main purpose is to achieve thermal performance of the unit increased over time, resulting in an ideal design of heat exchangers, used for example in the aerospace sector to control the temperature of on-board electronic components, thanks to the application of efficient nanocomposite coatings. It’s well-known, in fact, that dropwise condensation (DWC) as opposed to filmwise (FWC) condensation can lead to much higher heat transfer coefficients [25-28], improving so the energy efficiency in a large variety of engineering applications. The main idea of this research, so, is to fabricate hydrophobic and, in the same time, thermal conductive nanocomposite coatings applied on aluminum substrate that can reduce the filmwise condensation encouraging the dropwise one.

For this study, we fabricated multi-layered nanocomposite films deposited on aluminum substrates, with graphene nanoplatelets embedded in polyvinylidene fluoride (PVDF) thermoplastic polymer - N,N-Dimethylacetamid (DMAc) solvent solution, by spray-coating process. We performed, at last, thermal annealing treatment on all nanocomposite coatings fabricated and we investigated the effect of it on morphology, surface texture properties, hydrophobicity and thermal properties of graphene-based nanocomposite films on aluminum substrate.

References

[1] TRIBBLE A. The space environment and its impact on spacecraft design. 31st Aerospace Sciences Meeting1993. p. 491.

[2] Silverman EM. Space environmental effects on spacecraft: LEO materials selection guide, part 1. 1995.

[3] Dever J, Banks B, de Groh K, Miller S. Degradation of spacecraft materials. Handbook of environmental degradation of materials 2005:465-501.

[4] Hastings D, Garrett H. Spacecraft-environment interactions: Cambridge university press; 2004.

[5] Costa F, Monorchio A, Carrubba E, Zolesi V. Low RF reflectivity spacecraft thermal blanket by using high-impedance surface absorbers. 2012 ESA Workshop on Aerospace EMC: IEEE; 2012. p. 1-5.

[6] Mazzinghi A, Sabbadini M, Freni A. Enhanced rf behavior multi-layer thermal insulation. Scientific reports 2018;8:91.

[7] Micheli D, Apollo C, Pastore R, Morles RB, Laurenzi S, Marchetti M. Nanostructured composite materials for electromagnetic interference shielding applications. Acta Astronautica 2011;69:747-57.

[8] Delozier D, Connell J, Smith J, Watson K. Preparation and characterization of space durable polymer nanocomposite films from functionalized carbon nanotubes. 2003.

[9] Santonicola MG, Laurenzi S, Marchetti M. DNA-based sensors integrated in composite polymeric materials for monitoring radiation damage in space environment. 61st International Astronautical Congress 2010, IAC 20102010.

[10] Santonicola MG, Laurenzi S, Schön PM. Self-assembled carbon nanotube-DNA hybrids at the nanoscale: Morphological and conductive properties probed by atomic force microscopy. MRS Online Proceedings Library Archive 2014;1700:47-52.

[11] Johnson L, Young R, Montgomery E, Alhorn D. Status of solar sail technology within NASA. Advances in Space Research 2011;48:1687-94.

[12] Smith Jr J, Connell J, Delozier D, Lillehei P, Watson K, Lin Y, et al. Space durable polymer/carbon nanotube films for electrostatic charge mitigation. Polymer 2004;45:825-36.

[13] Vulpetti G, Santoli S, Mocci G. Preliminary investigation on carbon nanotube membranes for photon solar sails. Journal of the British Interplanetary Society 2008;61:284-9.

[14] Xie X-L, Mai Y-W, Zhou X-P. Dispersion and alignment of carbon nanotubes in polymer matrix: a review. Materials Science and Engineering: R: Reports 2005;49:89-112.

[15] Song YS, Youn JR. Influence of dispersion states of carbon nanotubes on physical properties of epoxy nanocomposites. Carbon 2005;43:1378-85.

[16] Clausi M, Santonicola MG, Laurenzi S. Fabrication of carbon-based nanocomposite films by spin-coating process: An experimental and modeling study of the film thickness. Composites Part A: Applied Science and Manufacturing 2016;88:86-97.

[17] Finckenor M, Dooling D. Multilayer insulation material guidelines. 1999.

[18] Stiles LA, Schaub H, Maute KK, Moorer DF. Electrostatically inflated gossamer space structure voltage requirements due to orbital perturbations. Acta Astronautica 2013;84:109-21.

[19] Kleiman J, Iskanderova Z, Perez F, Tennyson R. Protective coatings for LEO environments in spacecraft applications. Surface and Coatings Technology 1995;76:827-34.

[20] Woods A, Wenaas E. Spacecraft discharge electromagnetic interference coupling models. Journal of Spacecraft and Rockets 1985;22:265-81.

[21] Catani J-P, Payan D. Electrostatic behaviour of materials in a charging space environment. Proceedings of the 2004 IEEE International Conference on Solid Dielectrics, 2004 ICSD 2004: IEEE; 2004. p. 917-27.

[22] Rawal S, Brantley J, Karabudak N. Development of carbon nanotube-based composite for spacecraft components. 2013 6th International Conference on Recent Advances in Space Technologies (RAST): IEEE; 2013. p. 13-9.

[23] Nicoletto M, Boschetti D, Savi P. High Speed Digital Lines routed on non-metallic Spacecraft structures. 2014 International Symposium on Electromagnetic Compatibility: IEEE; 2014. p. 785-9.

[24] Harris C, Despa M, Kelly K. Design and fabrication of a cross flow micro heat exchanger. Journal of Microelectromechanical Systems 2000;9:502-8.

[25] Ma X-H, Zhou X-D, Lan Z, Yi-Ming L, Zhang Y. Condensation heat transfer enhancement in the presence of non-condensable gas using the interfacial effect of dropwise condensation. International Journal of Heat and Mass Transfer 2008;51:1728-37.

[26] Wu Y-T, Yang C-X, Yuan X-G. Drop distributions and numerical simulation of dropwise condensation heat transfer. International Journal of Heat and Mass Transfer 2001;44:4455-64.

[27] Rose J. Dropwise condensation theory and experiment: a review. Proceedings of the Institution of Mechanical Engineers, Part A: Journal of Power and Energy 2002;216:115-28.

[28] Peng B, Ma X, Lan Z, Xu W, Wen R. Analysis of condensation heat transfer enhancement with dropwise-filmwise hybrid surface: Droplet sizes effect. International Journal of Heat and Mass Transfer 2014;77:785-94.

Chapter 1 – *Nanocomposite films*

1.1 Carbon-based nanocomposite materials

Nanotechnology is a rapidly evolving field of research based on the control and manipulation of matter on a nanometric scale and on the design and construction of devices on this scale [1, 2]. It is applicable in several research fields, from engineering to chemistry, from biology to medicine and from physics to materials science. In particular, the polymeric materials in which nanometric inorganic particles with at least a size of 10-100 Å (1 A = 0.1 nm) are typically dispersed, are called polymeric nanocomposites which can potentially have multifunctional superior properties to those of the neat polymeric matrix [3-6]. Their excellent multifunctional properties are attributed to the fact that when the size of the reinforcements is on the order of nanometers, the percentage of surface atoms with respect to the total number of atoms becomes more significant and so the interfacial region, which represents the zone of "communication" between matrix and nano-reinforcement, increases considerably; this phenomenon is called ‘nano-effect’ and the resulting material is a nanocomposite [7]. It consists of an ultra-fine dispersion in which the contact area between the matrix and the nanofiller is enormous, and so very small quantities of nanofillers are needed to obtain significant increases in the polymer performance, further minimizing undesired effects such as the increase in density, the decreased workability and alteration of impact resistance properties. For example, to guarantee comparable reinforcement performance, 5-6 wt.% of nanofiller is sufficient, respect to the, typically used, higher percentages of ~20 wt.% for a classic filler. Over the years, materials with high Young modulus, heat resistance, high electrical and thermal conductivity, increased gas impermeability, flame resistance and increased biodegradability of polymers have been obtained. Nanocomposites have attracted significant attention as multifunctional materials with given thermal, electrical, optical properties, that can bring relevant progress in a wide range of technological applications, from aerospace to chemical industry.

One of the most widely studied classes of nanofillers is that of carbon nanoparticles (CNP): this class includes carbon nanotubes (CNT), carbon nanofibers (CNF) and graphene. In particular, carbonaceous nanofillers such as carbon nanotubes (CNTs) and graphene have a very promising role due to their excellent structural and multifunctional properties such as high proportion, high mechanical strength and high electrical and thermal properties [8-11].

In this PhD research, I focused on nanocomposites in which different types of CNT and graphene nanofillers are dispersed in the polymer matrix. The development of polymeric nanocomposites with tailored excellent and multifunctional properties depends on the properties and geometrical features of the nanofillers, CNTs or graphene, their grade of dispersion within the polymeric matrix as nano-reinforcements, their interaction with the polymeric matrix and the alignment of the nanofillers in the matrix [12-15].

1.1.1 Carbon nanotube (CNT)

Carbon nanotubes were discovered in 1991 by Japanese researcher Sumio lijima, who observed their presence among the secondary products of fullerene production, and can be seen as one of the allotropic forms of carbon [16]. It is possible to classify the carbon nanotubes into two large families: single-walled nanotubes (SWNTs) and multi-walled nanotubes (multi-walled nanotubes, MWNTs). An ideal SWNT is described as a carbon tube formed by a layer of graphite rolled up on itself to form a cylinder, closed at both ends by two hemispherical caps. The body of the nanotube is formed only by hexagons, while the end structures are composed by hexagons and pentagons, like the normal fullerenes. The very high ratio between length and diameter of SWNTs allows them to be considered as one-dimensional nanostructures. The MWNTs are nanotubes formed by several concentric SWNTs, and for that reason they are called multiple-walled nanotubes; there are often bonds between the various walls (lip-lip interaction) that stabilize the growth of the nanotube itself.

Carbon nanotubes possess higher mechanical and functional characteristics [17], associated with a specific weight much lower than that of most metals. To break a defect-free nanotube it is necessary to break all the strong carbon-carbon covalent bonds in it, so that it results in a very high mechanical strength. It has been calculated that the theoretical Young modulus of a nanotube can reach up to 1 TPa [18, 19], and its tensile strength should be around 150 GPa (100 times greater than that of steel, but compared to a weight 6 times lower) [19]. The nanotubes are not only resistant to breakage by traction, but they are also very flexible [18], and can be bent up to about 90° without breaking or being damaged. The extreme resistance, combined with flexibility, makes these materials ideal for use as reinforcement in polymeric matrices, producing high-performance nanocomposites [14, 15]. The use of nanotubes in fiber production can lead to the creation of much stronger composites than current ones based on traditional carbon fibers.

Regarding their higher electrical properties [20, 21], carbon nanotubes can behave both as conductors and as semiconductors depending on the way they are built. This feature is very important for applications in the electronics field: they could replace the traditional conductors and semiconductors in the microchips [22, 23].

Finally, due to their tubular shape, the nanotubes show strong capillary properties, and their large surface/weight ratio makes them theoretically ideal for the absorption of gases [24, 25].

1.1.2 Graphene

The graphene [8] is a material consisting of a single layer of sp^2 hybridized carbon atoms (that is, it has a thickness equivalent to the size of a single atom), bound by strong bonds σ and arranged so as to form hexagons with angles of 120°, with a distance between atoms equal to ~0.2 nm. The properties of graphene are mainly determined by its structural conformation, in particular by two unique characteristics that influence its properties and make it an extraordinary material. The first is structural perfection: it consists solely of carbon atoms joined together by strong and at the same time flexible bonds, which form a practically perfect crystalline structure, completely free of defects. The second peculiarity is that the electrons behave like massless particles, like photons, with very high electron mobility (μ), equal to 15000 $cm^2\ V^{-1}\ s^{-1}$ at room temperature. This makes this nanomaterial unique and suitable for many innovative applications. With a Young's modulus of 1 TPa and a breaking load of 130 GPa (smilar to that one of carbon nanotubes), graphene is one of the strongest and most resistant materials ever tested [26, 27]. For example, if compared to steel, graphene is 100 times stronger.

The thermal conductivity of graphene is very high and equal to 5000 W/m·K [28, 29], much higher than traditional materials such as copper equal to 401 W/m·K.

The electrical properties constitute one of the most studied aspect of the graphene. Given the extreme speed of the electrons, the electrical conductivity is very high, with a value of ~6000 S/cm [30]. The absence of a band-gap in graphene justifies the behavior of this as a metallic material. This is true as long as the graphene layer is in the order of a few microns or hundreds of nanometers. In fact, it is possible to have a different band-gap if the size of the graphene is reduced in sheets with a width of 1-2 nm, thus obtaining semiconductive graphene with potential applications in microelectronics [31].

The theoretical surface area of graphene is very high equal to 2630 m^2/g, while the experimental values found by BET analysis are in the range between 270 and 1550 m^2/g, and so it is impermeable to standard gases including helium [32] and is able to absorb and desorb on its surface different atoms and molecules [33].

1.2 Nanocomposite films

The deposition of nanocomposite films is the process that allows the application on a surface of layers of materials, with thickness that varies between fractions of nanometers to a few microns. Nanometric engineering of surfaces and layers helps to obtain, with the modification of the surface of the substrate, materials with particular surface properties and functionalities.

It is possible to obtain nanocomposite surfaces resistant to abrasion, corrosion, with high hydrophobic or hydrophilic properties, surfaces with anti-reflective and antiscratch properties and nanocoated surfaces with specific electrical and thermal properties. The development of nanocomposite coatings needed to define deposition techniques suitable for the production of coatings.

1.2.1 Deposition processes of nanocomposite films

The deposition techniques studied and investigated in this PhD research are: Spin-Coating, Drop casting, Spray-Coating and Bar-Coating processes.

1.2.1.1 Spin Coating

Spin-Coating (Fig.1) is a process used to apply a homogeneous and uniform film on a solid and flat substrate [34]. During this process, a defined quantity of a

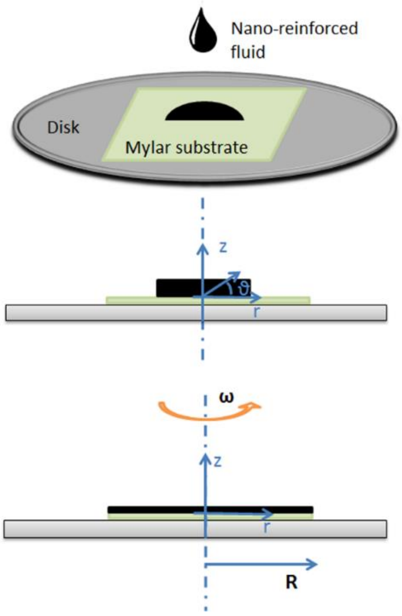

Fig. 1. Schematic of spin-coating process for the fabrication of nano-reinforced thin composite films [35]

dilute solution (for example, within that research thesis, a nanocomposite blend) is deposited on the substrate, which is subsequently put into rapid rotation by a rotating disk in order to spread the fluid on the substrate to effect of centrifugal force. The solvents used are usually very volatile, so the film thins out during the process also due to the evaporation of the solvent. The rotation is stopped as soon as the desired thickness is reached. The spin-coating technique is used, as mentioned above, to prepare homogeneous and uniform polymeric films and the unique limit is represented by the fact that it’s possible to obtain smaller coatings in terms of covered area on substrate. Many studies have been carried out concerning the effects of spin-coating on the properties of polymeric films based on carbon nanotubes and graphene.

I previously investigated [35], for example, the effects of spin-coating parameters on the final nanocomposite film thicknesses obtained by considering the rheological nature of MWCNTs/xGnPs-based nanocomposite blends prepared. The experimental results were in good agreement with the developed analytical model for the final film thickness and in particular, from a rotational speed of 3000 rpm for the rotating disk it’s possible to obtain films with uniform thickness. Schmidt et al. [36] studied the possibility to fabricate MWCNTs-based nanocomposite films obtained by spic-coating process to replace indium tin oxide (ITO) thin-film. The blend was prepared by using a low volatility solvent, a thermoplastic polymer matrix and multi-walled carbon nanotubes: the obtained nanocomposite films show good electrical behavior and optical transparency for very low concentrations of multi-walled carbon nanotubes exploiting the geometrical nature of those nanofillers and its high aspect ratio.

1.2.1.2 Drop Casting

Drop Casting is a very simple process and it consists in casting a homogeneous nanocomposite blend by dropping it on a target substrate. During this process, a defined quantity of a well-dispersed solution is deposited on the substrate by using a syringe or pipette, subsequently, after the evaporation of the solvents used in the mixture, at the end of curing process in oven or in air for a given time and temperature depending on thermal properties of the solution, the final film is obtained. In that case the final film thickness can be regulated by the quantity of casted solution and by the dimension of the substrate.

1.2.1.3 Spray-Coatinq

The spray coating process [37, 38] (Fig.2) consists in applying an external pressure which permits the exit of the (nanocomposite) solution through the exit nozzle of an aerograph. During this deposition process, a defined quantity of a dilute nanocomposite ink is sprayed on the substrate at fixed spraying distance and time. Many solvents can be used and, in connection with this, the temperature of the substrate is selected to allow the evaporation of the solvent. From the depositions of numerous small droplets on the target substrate the final film is formed. In this way, it’s possible also to deposit a different number of layers of solution on the substrate and to control the quality of the final films and its thicknesses by varying the feeding rate, the applied pressure, the spraying distance, the spraying time, the direction of the spraying, the nozzle diameter of the aerograph as well as the composition and so the viscosity of the sprayed mixture.

The spray-coating technique, as opposed to the spin-coating one, allows to fabricate larger polymeric coatings in terms of covered area on planar and not substrates, becoming an attractive method for large scale production of coatings.

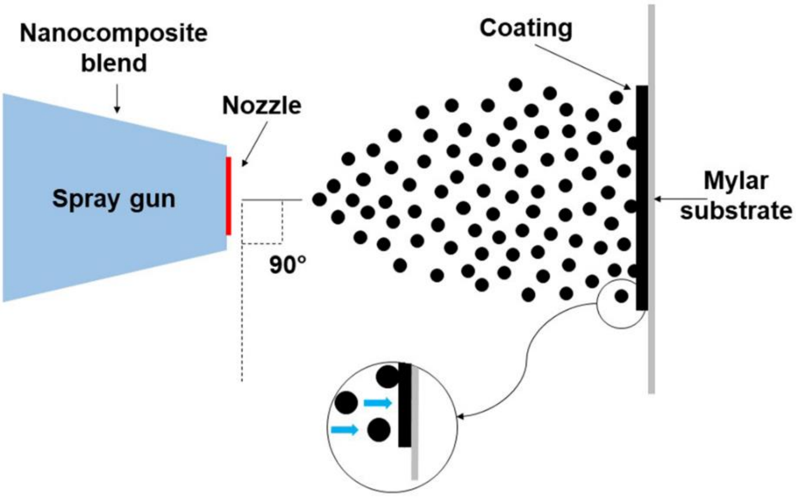

Fig. 2. Schematic of spin-coating process for the fabrication of nano-reinforced thin composite films [37]

1.2.2 Bar-Coatinq

Bar coating process [39] consists in a first step of drop casting in which a fixed amount of nanocomposite mixture is dropped in different spots in orderly sequence on the top of the substrate and subsequently, by using a wire bar coater, the casted solution is spread on the substrate in a constant direction. At the end of curing process the final film is obtained, with a thickness controlled by the area of groove between the coils of wire. In this PhD research, bar-coating technique was used to fabricate larger polymeric coatings due to the high viscosity nature of the aerospace-grade structural adhesives used as matrices becoming an attractive method for industrial production of coatings.

1.3 Nanocomposite coatings in the aerospace sector

It’s well known that the hostile space environment causes larger degradation effects on polymer-based material used on the exterior of the spacecrafts due to the combination of ultraviolet UV radiations, vacuum, atomic oxygen, plasma, surface charging, charged particle radiation, orbital debris as well as large temperature gradients, which can compromise the success of the entire mission [40-43]. Depending on the specific characteristics of the mission including the duration, the operational altitude and inclination, the orbital parameters as well as the solar cycle and the view angle of spacecraft surfaces to the sun, the magnitude of space weather impacts on spacecraft components vary greatly and in particular, the choice of the various materials has to be taken into account for spacecraft construction to guarantee a longer operability [43]. Fig.3 summarizes pictorially many space hazards that must be considered during space mission design to guarantee the correct operability of the spacecraft.

Radiation and neutral O-atoms damage, for example, can lead to surface erosion of the spacecraft, causing deterioration of thermal/electrical/optical properties, degradation of the structural integrity and decreasing of power output of the solar arrays as well. In particular, it’s well-known that the UV-C radiation damages polymer-based materials by breaking polymer chains causing degradation in material properties. In the Low Earth Orbit (LEO) environment, in which the International Space Station (ISS) and most communication satellites are located, approximately the 0.8% of the solar irradiance value is in the UV-C region, in particular 1.30 mW/cm^2 at the wavelength of 254 nm [44].

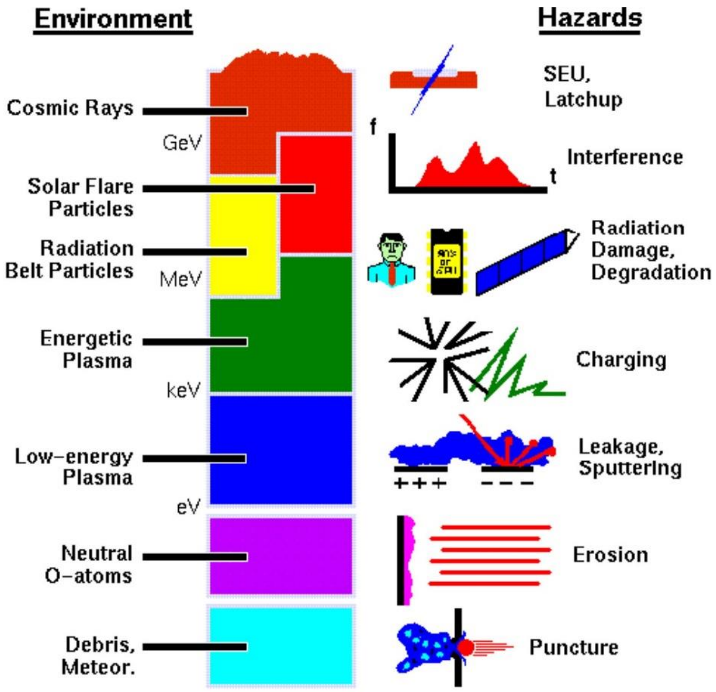

Fig. 3. Hazards and risks from the space environment (Source: European Space Agency, Space Environment and Effects Analysis Section- ESA/ESTEC/TEC-EES)

UV radiation, also, under high vacuum can also generate oxygen holes in oxides, leading to color changes.

In LEO orbit, also, the solar UV ionizes the ambient neutrals producing so energetic plasma, with a peak density at about 300 km of distance where the photoionization is the most relevant mechanism. Space plasma can charge the spacecraft to high and different electrical potentials due to the different electrical conductivity nature of the various elements of spacecraft, which can lead to arc discharcing that can damage permanently the spacecraft subsystem and interfere with electronic components, as well as dielectric breakdown. NASA identified different guidelines to control and minimize plasma-induced spacecraft charging, including grounding all conductive and partially conductive elements of spacecraft to a common ground or making the exterior spacecraft surfaces partially conductive in order to minimize potential differences and so the charging [43].

It is evident, so, that it’s necessary to find solutions to protect or isolate the spacecraft components from the operating environment without however compromising its operation. In particular, multifunctional coatings, to be applied to the traditional spacecraft materials, are taken into account of carrying out this function. Such coatings must respect some requirements: for example they have to guarantee specific mechanical, electrical or thermal performance, the adhesion between coating and substrate has to be strong to be resistant to the stresses that act on the overall assembly. Poor adhesion, in fact, can lead to peeling off and breakup of the coatings [45]. Moreover, the coating must ensure high properties of flexibility, since it must be able to accommodate any bending of the base without damaging itself and must not present too high dimensional variations.

The development of carbon-based multifunctional films on polymer membranes, which combine mechanical flexibility with given thermal, electrical, optical and electromagnetic characteristics, is a promising approach that can bring relevant progress in aerospace missions and accomplishment of many space projects that could strongly imprint human life and vision.

For example, one of the major technical challenges in telecommunication satellites is to reduce many problems due to electromagnetic interference (EMI) by developing innovative systems for electromagnetic shielding (EM). The choice of the most appropriate material for electromagnetic shielding is based on several factors which include: the degree of shielding required (measured in dB), physical aspects (for example the material can be exposed to high shear or compression forces), environmental factors, and possibly resistance to high temperatures and corrosion. In particular, traditional metals, due to their high electrical conductivity, are ideal candidates as materials for EM-RF (radio frequency) shielding [46]. However, since they present limits due to their high density and the possibility of corroding in aggressive environments and also they tend to wear and tear, other types of material suitable for EMI shielding are being considered. In particular, carbon-based polymer films (namely with CNT and graphene), due to their low weight, corrosion resistance and the excellent electrical and thermal properties, with nanoparticles dispersed in precise concentrations inside the insulating matrix, which induce the absorption of power of the radiation and its dissipation within the nanocomposite, while reducing the total reflection of the wave on the surface, could represent ideal candidates for shielding applications (EMI) [47-49]. Yan et al. [50] for example, fabricated porous graphene-polystirene composites with an average EMI shielding efficiency (SE) of around 29 dB with potential spacecraft applications. Li et al. [51] obtained higher values, higher of 20 dB, of EMI shielding efficiency by introducing SWNTs in different polymer matrices.

The space environment, as mentioned above, is very critical: in particular, due to the extreme temperatures to which the structures of space systems are subjected, appropriate insulation systems and thermal protection are required. The heat sources to which a satellite in orbit around the earth is subjected are mainly four:

solar thermal radiation and its reflection by the earth's atmosphere (albedo), the infrared radiation emitted by the earth and the internal dissipation of the various electronic components. The function of the thermal control systems is essentially to maintain the temperature of all the structural, mechanical and electronic components within specific limits during the whole operating life of the spacecraft. In the aerospace field, passive thermal control systems are of great importance in order to comply with the constraints imposed by requirements of weight and bulk as much as possible. In the following, reference will be made in particular to the multi-layer insulation blankets (MLI), for the isolation of sensitive components, which make it possible to optimize the ratios between the flow of heat absorbed, radiated and transmitted in thermal control systems of satellites and vehicles in space. The MLI are made up of a certain number of layers of plastic material, usually a layer of Kapton for the external covering and Mylar for the inner sheets, coated with aluminum on one or both sides and separated by networks of grocers, generally of Dracon, which allow to minimize the heat transmitted by conduction between the layers. However, due to their high reflectivity, traditional MLI blankets tend to generate passive intermodulation products (PIM) and mutual coupling effects between the antennas present on communication satellites and on all space planes in general. In this regard, to try to reduce these problems as much as possible, innumerable studies have been conducted on the possibility of making MLI blankets with a low RF reflectivity index by inserting a thin layer of carbon nanoparticle-based composite (CNT), having a high absorbance, inside them. In particular, Costa et al. [52] have developed an innovative MLI by replacing the last inner layer with a thin layer of highly absorbent material and have analyzed the performance of the structure made in terms of its absorption field in relation to an incident radiation both normal and oblique to the surface. One of the most promising concepts to reduce RF reflectivity is the use of frequency selective surfaces as layers of the MLI [53]. This is accomplished by using nanostructured carbon-based films on membranes, which can also improve the protection of the payload by the MLI (and in general by flexible membranes) with respect to space radiations and impact events.

In satellite and space applications in general there is a need to use large functional elements, such as antennas, reflectors, solar panels, solar sails etc. These components must be stored in limited spaces, during transport and be deployed in their operational configuration once the working position is reached. Generally, this operation is carried out by means of mechanical deployment systems (Fig.4). Recent technological developments, in the field of ultralight structures, have provided new possibilities for obtaining answers to the need for large-scale structures in low-cost and low-weight space, alternatives to traditional deployment systems. For the general use of ultra-light membranes and components, this category of structures is called gossamer: they have the great advantage of being able to be enclosed in a small space with great cost savings [54-57]. The gossamer structures consist of membrane structures, therefore characterized by limited flexural rigidity and inability to sustain compressive loads. They are often produced using thin, highly flexible, low elastic modulus and light polymeric films: in particular, currently, among the most widely used materials there are Mylar, Kapton and polyimide films with thin metallic coatings. Recently, NASA-LaRC developed, with a view to Gossamer deployment, novel polyimide films reinforced with a small amount of SWNTs to enhance its electrical conductivity with the aim to mitigate electrostatic charge build-up on the polymeric films in-orbit [54, 55].

(a) Launch configuration (b) During deployment

(c) Deployed (d) Deployed and mechanisms jettisoned

Fig. 4. Gossamer-1satellite: controlled and autonomous deployment (in LEO) sequence [58].

Multifunctional nanocomposite films are currently investigated also in the aerospace field to create UV-sensors [59-61] with the aim, for example, to monitor the radiation absorbed by the astronauts during extra vehicular activities (EVA), to monitor the health status of spacecraft composite structures, or as new and advanced grounding systems to mitigate plasma-induced spacecrafts charging [62].

In addition, these nanocomposite films could be useful in interplanetary missions that are conceived to be realized exclusively using solar sailing. Solar photon sailing is a revolution in space propulsion, offering a continuous low-thrust propellant-less driving mode, which can act for any mission-required time length. On the other hand, in order to obtain the necessary thrust with the current technology, the solar sail membrane must have huge dimensions (approximately a standard football field). The solar sail thrust propulsion can be enhanced using carbon nanotubes (CNTs) as photonic materials in the back side of the polymer membrane [59, 63].

1.4 References

[1] Dowling AP. Development of nanotechnologies. Materials Today 2004;7:30-5.

[2] Roco MC. The vision and strategy of the US national nanotechnology initiative. Nanotechnology: Global Strategies, Industry Trends and Applications (J Schulte, ed), John Wiley & Sons, Ltd 2005:79-94.

[3] Rafiee MA, Rafiee J, Wang Z, Song H, Yu Z-Z, Koratkar N. Enhanced mechanical properties of nanocomposites at low graphene content. ACS nano 2009;3:3884-90.

[4] Guo Z, Pereira T, Choi O, Wang Y, Hahn HT. Surface functionalized alumina nanoparticle filled polymeric nanocomposites with enhanced mechanical properties. Journal of Materials Chemistry 2006;16:2800-8.

[5] Rafiee MA, Yavari F, Rafiee J, Koratkar N. Fullerene–epoxy nanocomposites-enhanced mechanical properties at low nanofiller loading. Journal of Nanoparticle Research 2011;13:733-7.

[6] Boček J, Matějka L, Mentlík V, Trnka P, Šlouf M. Electrical and thermomechanical properties of epoxy-POSS nanocomposites. European Polymer Journal 2011;47:861-72.

[7] Crosby AJ, Lee JY. Polymer nanocomposites: the “nano” effect on mechanical properties. Polymer reviews 2007;47:217-29.

[8] Aliofkhazraei M, Ali N, Milne WI, Ozkan CS, Mitura S, Gervasoni JL. Graphene science handbook: electrical and optical properties: CRC press; 2016.

[9] Balandin AA, Ghosh S, Bao W, Calizo I, Teweldebrhan D, Miao F, et al. Superior thermal conductivity of single-layer graphene. Nano letters 2008;8:902-7.

[10] Popov VN. Carbon nanotubes: properties and application. Materials Science and Engineering: R: Reports 2004;43:61-102.

[11] Terrones M. Science and technology of the twenty-first century: synthesis, properties, and applications of carbon nanotubes. Annual review of materials research 2003;33:419-501.

[12] Xie X-L, Mai Y-W, Zhou X-P. Dispersion and alignment of carbon nanotubes in polymer matrix: a review. Materials Science and Engineering: R: Reports 2005;49:89-112.

[13] Song YS, Youn JR. Influence of dispersion states of carbon nanotubes on physical properties of epoxy nanocomposites. Carbon 2005;43:1378-85.

[14] Wang Q, Dai J, Li W, Wei Z, Jiang J. The effects of CNT alignment on electrical conductivity and mechanical properties of SWNT/epoxy nanocomposites. Composites science and technology 2008;68:1644-8.

[15] Prashantha K, Soulestin J, Lacrampe M-F, Krawczak P, Dupin G, Claes M. Masterbatch-based multi-walled carbon nanotube filled polypropylene nanocomposites: Assessment of rheological and mechanical properties. Composites science and technology 2009;69:1756-63.

[16] Delgado JL, Herranz MÁ, Martin N. The nano-forms of carbon. Journal of Materials Chemistry 2008;18:1417-26.

[17] Salvetat J-P, Bonard J-M, Thomson N, Kulik A, Forro L, Benoit W, et al. Mechanical properties of carbon nanotubes. Applied Physics A 1999;69:255-60.

[18] Yakobson BI, Avouris P. Mechanical properties of carbon nanotubes. Carbon nanotubes: Springer; 2001. p. 287-327.

[19] Choi BK, Yoon GH, Lee S. Molecular dynamics studies of CNT-reinforced aluminum composites under uniaxial tensile loading. Composites Part B: Engineering 2016;91:119-25.

[20] Ebbesen T, Lezec H, Hiura H, Bennett J, Ghaemi H, Thio T. Electrical conductivity of individual carbon nanotubes. Nature 1996;382:54.

[21] Kong J, Zhou C, Morpurgo A, Soh H, Quate C, Marcus C, et al. Synthesis, integration, and electrical properties of individual single-walled carbon nanotubes. Applied Physics A 1999;69:305-8.

[22] Collins PG, Avouris P. Nanotubes for electronics. Scientific american 2000;283:62-9.

[23] Mogensen KB, Chen M, Molhave K, Boggild P, Kutter JP. Carbon nanotube based separation columns for high electrical field strengths in microchip electrochromatography. Lab on a Chip 2011;11:2116-8.

[24] Ong KG, Zeng K, Grimes CA. A wireless, passive carbon nanotube-based gas sensor. IEEE Sensors Journal 2002;2:82-8.

[25] Calbi MM, Toigo F, Cole MW. Dilation-induced phases of gases absorbed within a bundle of carbon nanotubes. Physical review letters 2001;86:5062.

[26] Frank I, Tanenbaum DM, van der Zande AM, McEuen PL. Mechanical properties of suspended graphene sheets. Journal of Vacuum Science & Technology B: Microelectronics and Nanometer Structures Processing, Measurement, and Phenomena 2007;25:2558-61.

[27] Bu H, Chen Y, Zou M, Yi H, Bi K, Ni Z. Atomistic simulations of mechanical properties of graphene nanoribbons. Physics Letters A 2009;373:3359-62.

[28] Jauregui LA, Yue Y, Sidorov AN, Hu J, Yu Q, Lopez G, et al. Thermal transport in graphene nanostructures: Experiments and simulations. Ecs Transactions 2010;28:73-83.

[29] Balandin AA, Ghosh S, Nika D, Pokatilov E. Extraordinary thermal conductivity of graphene: possible applications in thermal management. ECS Transactions 2010;28:63-71.

[30] Yang Z, Gao R, Hu N, Chai J, Cheng Y, Zhang L, et al. The prospective two-dimensional graphene nanosheets: preparation, functionalization and applications. Nano-Micro Letters 2012;4:1-9.

[31] Sinitskii A, Tour JM. Patterning graphene through the self-assembled templates: toward periodic two-dimensional graphene nanostructures with semiconductor properties. Journal of the American Chemical Society 2010;132:14730-2.

[32] Nair R, Wu H, Jayaram P, Grigorieva I, Geim A. Unimpeded permeation of water through helium-leak–tight graphene-based membranes. Science 2012;335:442-4.

[33] Ko G, Kim H-Y, Ahn J, Park Y-M, Lee K-Y, Kim J. Graphene-based nitrogen dioxide gas sensors. Current Applied Physics 2010;10:1002-4.

[34] Tyona M. A theoritical study on spin coating technique. Advances in materials Research 2013;2:195-208.

[35] Clausi M, Santonicola MG, Laurenzi S. Fabrication of carbon-based nanocomposite films by spin-coating process: An experimental and modeling study of the film thickness. Composites Part A: Applied Science and Manufacturing 2016;88:86-97.

[36] Schmidt RH, Kinloch IA, Burgess AN, Windle AH. The effect of aggregation on the electrical conductivity of spin-coated polymer/carbon nanotube composite films. Langmuir 2007;23:5707-12.

[37] Laurenzi S, Clausi M, Zaccardi F, Curt U, Santonicola MG. Spray coating process of MWCNT/epoxy nanocomposite films for aerospace applications: Effects of process parameters on surface electrical properties. Acta Astronautica 2019;159:429-39.

[38] Van Steenkiste TH, Smith JR, Teets RE, Moleski JJ, Gorkiewicz DW. Kinetic spray coating method and apparatus. Google Patents; 2000.

[39] Ichikawa K, Nishino G, Kaneko N. Bar coating apparatus and bar coating method. Google Patents; 2004.

[40] Dever J, Banks B, de Groh K, Miller S. Degradation of spacecraft materials. Handbook of environmental degradation of materials 2005:465-501.

[41] Dever JA, Miller SK, Sechkar EA, Wittberg TN. Space environment exposure of polymer films on the materials international space station experiment: results from MISSE 1 and MISSE 2. High Performance Polymers 2008;20:371-87.

[42] Hastings D, Garrett H. Spacecraft-Environment Interactions. Cambridge: Cambridge University Press; 1996.

[43] TRIBBLE A. The space environment and its impact on spacecraft design. 31st Aerospace Sciences Meeting1993. p. 491.

[44] Gueymard CA. The sun's total and spectral irradiance for solar energy applications and solar radiation models. Solar energy 2004;76:423-53.

[45] Qiu N, Wang L, Wu S, Likhachev DS. Research on cavitation erosion and wear resistance performance of coatings. Engineering Failure Analysis 2015;55:208-23.

[46] Tzeng S-S, Chang F-Y. EMI shielding effectiveness of metal-coated carbon fiber-reinforced ABS composites. Materials Science and Engineering: A 2001;302:258-67.

[47] Rawal S, Brantley J, Karabudak N. Development of carbon nanotube-based composite for spacecraft components. 2013 6th International Conference on Recent Advances in Space Technologies (RAST): IEEE; 2013. p. 13-9.

[48] Pourzahedi L, Zhai P, Isaacs JA, Eckelman MJ. Life cycle energy benefits of carbon nanotubes for electromagnetic interference (EMI) shielding applications. Journal of cleaner production 2017;142:1971-8.

[49] Al-Saleh MH, Saadeh WH, Sundararaj U. EMI shielding effectiveness of carbon based nanostructured polymeric materials: a comparative study. Carbon 2013;60:146-56.

[50] Yan D-X, Ren P-G, Pang H, Fu Q, Yang M-B, Li Z-M. Efficient electromagnetic interference shielding of lightweight graphene/polystyrene composite. Journal of Materials Chemistry 2012;22:18772-4.

[51] Li N, Huang Y, Du F, He X, Lin X, Gao H, et al. Electromagnetic interference (EMI) shielding of single-walled carbon nanotube epoxy composites. Nano letters 2006;6:1141-5.

[52] Costa F, Monorchio A, Carrubba E, Zolesi V. Low RF reflectivity spacecraft thermal blanket by using high-impedance surface absorbers. 2012 ESA Workshop on Aerospace EMC: IEEE; 2012. p. 1-5.

[53] Micheli D, Apollo C, Pastore R, Morles RB, Laurenzi S, Marchetti M. Nanostructured composite materials for electromagnetic interference shielding applications. Acta Astronautica 2011;69:747-57.

[54] Camargo PHC, Satyanarayana KG, Wypych F. Nanocomposites: synthesis, structure, properties and new application opportunities. Materials Research 2009;12:1-39.

[55] Delozier D, Connell J, Smith J, Watson K. Preparation and characterization of space durable polymer nanocomposite films from functionalized carbon nanotubes. 2003.

[56] Jenkins CH. Gossamer spacecraft: membrane and inflatable structures technology for space applications: American Institute of Aeronautics and Astronautics; 2001.

[57] Ruggiero EJ, Inman DJ. Gossamer spacecraft: recent trends in design, analysis, experimentation, and control. Journal of Spacecraft and Rockets 2006;43:10-24.

[58] Seefeldt P, Spietz P, Sproewitz T, Grundmann JT, Hillebrandt M, Hobbie C, et al. Gossamer-1: Mission concept and technology for a controlled deployment of gossamer spacecraft. Advances in Space Research 2017;59:434-56.

[59] Johnson L, Young R, Montgomery E, Alhorn D. Status of solar sail technology within NASA. Advances in Space Research 2011;48:1687-94.

[60] Santonicola MG, Laurenzi S, Schön PM. Self-assembled carbon nanotube-DNA hybrids at the nanoscale: Morphological and conductive properties probed by atomic force microscopy. MRS Online Proceedings Library Archive 2014;1700:47-52.

[61] Munakata N, Makita K, Bolsée D, Gillotay D, Horneck G. Spore dosimetry of solar UV radiation: applications to monitoring of daily irradiance and personal exposure. Advances in Space Research 2000;26:1995-2003.

[62] Smith Jr J, Connell J, Delozier D, Lillehei P, Watson K, Lin Y, et al. Space durable polymer/carbon nanotube films for electrostatic charge mitigation. Polymer 2004;45:825-36.

[63] Vulpetti G, Santoli S, Mocci G. Preliminary investigation on carbon nanotube membranes for photon solar sails. Journal of the British Interplanetary Society 2008;61:284-9.

Chapter 2 - *Analysis of UV-C effects on the surface properties of epoxy/graphene nanocomposite films on Mylar substrate* [1]

---

[1] Taken from the publication: ‘Analysis of ultraviolet exposure effects on the surface properties of epoxy/graphene nanocomposite films on Mylar substrate, Acta Astronautica, vol.134, 307-313, 2017 (doi.org/10.1016/j.actaastro.2017.02.017)’.

Abstract

Epoxy/graphene nanocomposite films were fabricated on Mylar substrate at different nanoparticle loadings using spin-coating process. The effects of UV-C radiations on the wettability and the electrical characteristics of graphene/epoxy films were investigated. The specimens were irradiated at given UV-C dose, and electrical resistance as well as, contact angle analysis were performed on untreated and irradiated samples.

2.1 Introduction

Space is well recognized as a hostile environment for spacecrafts [1], affecting on-board electronics and structural components, as well as for human life [2]. Indeed, the presence of electromagnetic radiations [3], charged particles coming from stars, large gradients of temperature, micro-meteorites and space debris [4] are known to compromise the functionality of aerospace components in a significant way. In particular, space conditions lead to a degradation of polymeric materials altering the electrical, thermal and optical properties of the materials [5, 6].

Polymer membranes are widely used in the aerospace sector when it is necessary to obtain specific optical and thermal properties combined with lightweight and structural flexibility, in particular in multi-layer insulation (MLI) blankets for satellites [7, 8] and in propulsion systems for solar sails [9-11]. To achieve multifunctional properties of the polymer-based membranes, the deposition of nanostructured coatings, in particular carbon-based nanocomposite films as an alternative to conventional silicon-based micro/nano-structured surfaces [12], is currently investigated with the aim to protect the surfaces by space environmental exposure, including UV radiations [13], vacuum [14], atomic oxygen [15], and to confer specific properties at the same time. For example, solar sailing, which is based on phonons acting on large thin membranes, is expected to be a revolution in space propulsion, due to its continuous low-thrust propellant-less mode that can act for any mission time length. For such application, the membrane general performance, at both optical and electromagnetic level, can be improved by coating the membranes with a thin layer of material containing carbon nanoparticles [16, 17].

In the family of carbon nanoparticles, graphene nanoplatelets (GnP) are one of the most promising nano-reinforcements for novel protection materials, due to their superior electrical, mechanical, thermal and magnetic properties [18-20]. As with carbon nanotubes (CNT), the geometric features of graphene nanoplatelets are known to be crucial parameters that affect the functional and structural properties of the resulting composite material [21-23]. Despite their exceptional features on Earth, the applicability of carbon-based nanocomposite films in space environment needs to be thoroughly investigated to understand how these elements can be implemented in the real spacecraft design.

The main objective of this work is to investigate the effects of space-abundant UV-C radiation on carbon-based nanocomposite films deposited on flexible Mylar substrates, which are commonly used in multi-layer insulations for satellites. For this study, we fabricated nanocomposite films with graphene nanoparticles embedded in epoxy resin by spin-coating process following our previous investigations [24, 25]. Three different grades of commercial graphene nanoplatelets (xGnP, grades C750, M5 and H5) were dispersed homogenously at different weight percentages, ranging from 0.5 to 7 wt%, into the epoxy matrix. The effects of UV-C exposure on the different types of nanocomposite film samples were investigated in terms of surface electrical properties and surface hydrophobicity/hydrophilicity, which is a relevant parameter to assess the level of moisture absorption by the films.

2.2 Experimental

2.2.1 Materials

Epoxy/graphene nanocomposite films were fabricated by incorporating xGnP nanoplatelets purchased from XG Sciences Inc. (USA) in an epoxy polymer film. The graphene nanoplatelets were of grades C750 (particle diameter of less than 2 μm), M5 (particle diameter of 15 μm) and H5 (particle diameter of 15 μm) with average thickness of 2 nm, 7 nm, and 15 nm, and specific surface areas of 750 m^2/g, 120 m^2/g and 70 m^2/g, respectively. The resin Prime 20 LV manufactured by Gurit (UK) was selected for the epoxy matrix. Mylar thin membranes with 15 μm thickness were used as substrate of the nanocomposite films.

2.2.2 Fabrication of epoxy/graphene nanocomposite films

Epoxy/graphene nanocomposite films were manufactured by spin-coating process following the procedure described in our previous works [24, 25]. Typically, the first step of the process consisted of preparing a homogeneous fluid mixture adding the nanoplatelets at a given weight percentage to the epoxy matrix. The mixture was mechanically stirred for 20 min and then kept in ultrasonic bath for 60 min. After sonication, the curing agent was gently added to the blend in the ratio of 100:26 by weight with respect to the epoxy base component. This procedure was repeated for each type of xGnP at concentrations of 0.5 wt%, 1 wt%, 3 wt%, 5 wt%, and 7 wt%.

For the spin-coating process, a fixed amount of fluid mixture was dropped at the center of a Mylar substrate (60 mm × 60 mm) positioned on the spin coater disk. The spin coater used was the CaLCTec FR10KPA equipped with a microporous chuck to guarantee a flat surface of the flexible Mylar membrane avoiding local wrinkles. Nanocomposite films were spin-coated at angular velocity of 3000 rpm, and then cured in oven at 50 °C for 16 h. The final average thicknesses of the epoxy/xGnP films after cure were measured using a micrometer screw gauge (accuracy 1 μm). Thickness measurements were repeated in quintuplicate across a sample area and values were averaged. Film thicknesses were in the range 15 - 40 μm depending on nanoplatelets grade and concentration.

2.2.3 Experimental characterization

Surface wettability was characterized by measuring water contact angles (WCA) on the basis of the sessile drop method using a DataPhysics OCA15 Pro analyzer (DataPhysics Instruments, Germany). Ultrapure Milli-Q water was dispensed through a gas-tight Hamilton syringe of 0.5-mL volume. The values of contact angles were obtained by fitting the data using the Young-Laplace equation. A minimum of five drops (volume of 4 μl and dosing rate of 0.3 μl/s) in different spots of the sample surface were analyzed.

Electrical characterization of the nanocomposite films was carried out at various frequencies in electrical impedance spectroscopy (EIS) using an Agilent E4980A Precision LCR Meter. The samples were contacted by means of flat copper bars, which were pressed and kept parallel to each other using the text fixture shown in Fig. 1.

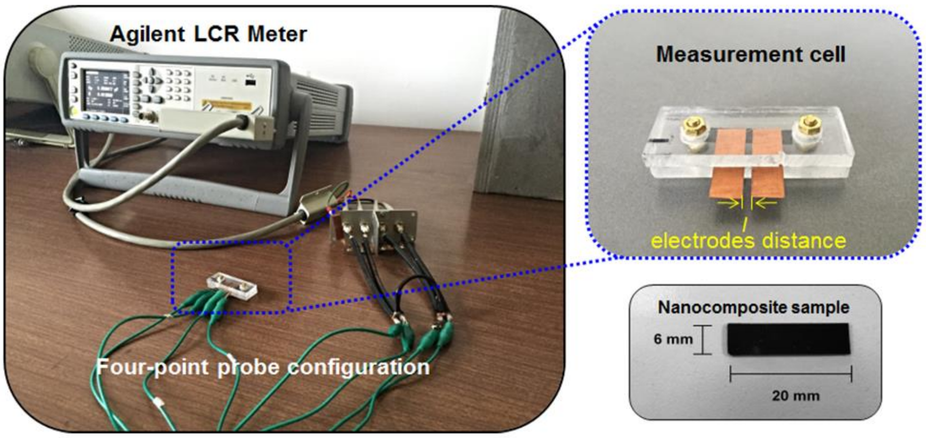

Fig. 1. Experimental set-up for electrical measurements on nanocomposite films deposited by spin-coating on Mylar thin membranes.

Impedance measurements were performed under the parallel circuit model. Specifically, the results reported in Section 3.2 are based on the equivalent parallel resistance (R_P), as provided by the instrument. In order to analyze the effects of UV-C radiation on the nanocomposite films, the surface electrical properties of the samples were characterized before and after the UV-C exposure tests. The R_P measurements were normalized with respect to the distance *l* between the two copper electrodes ($R_P^* = R_P/l$). The normalized resistance change over the course of the radiation exposure was calculated according to the following formula:

$$\Delta R^*_{normalized} = (R_p^* - R_{p,0}^*) / R_{p,0}^* \quad (1)$$

where $R_{p,0}^*$ is the resistance of the non-irradiated samples normalized with respect to the distance between the electrodes. A minimum of twenty measurements were performed for each nanocomposite sample at each exposure time. The surface resistivity (ρ_S) and the surface conductivity (σ_s) of the nanocomposite films were calculated as:

$$\rho_S = R_p \times D/l \quad (2)$$

$$\sigma_s = 1/\rho_S \quad (3)$$

where D is the length of the electrodes in contact with the sample surface. UV-C irradiation tests on the nanocomposite films were conducted using a low-pressure UV lamp (8 W, multi-wavelength handheld lamp 3UV-38, UVP LLC, USA) at fixed wavelength of 254 nm. Specimens were placed in a closed chamber and radiated at 3.765 W/m^2 for 1, 2, 3, 4, 5, 7 and 9 h. The irradiance was measured and controlled using a photo-radiometer by Delta OHM equipped with a combined probe for UV-C radiation. Fig. 2 shows the UV irradiation set-up with the chamber containing the nanocomposite sample and the UV sensor probe for irradiance measurement.

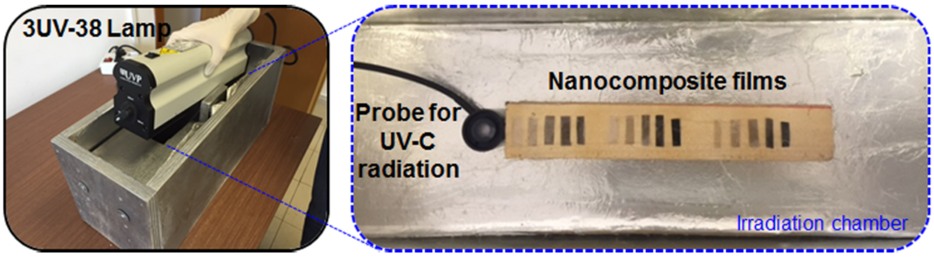

Fig. 2. UV irradiation set-up with inner view of the chamber containing the nanocomposite sample and the UV sensor probe for irradiance measurement.

2.3 Results and discussion

2.3.1 Surface wettability of epoxy/graphene nanocomposite films

The contact angle analysis using water as testing fluid was conducted to obtain information on the surface hydrophobicity/hydrophilicity of the epoxy/xGnP nanocomposite films, and how this property is affected by exposure to UV-C radiation. Fig. 3 compares the water contact angle (WCA) values at equilibrium for the nanocomposite films at 0.5, 3 and 7 wt% of the three different grades of xGnP (C750, M5, H5), before and after 9 h of exposure to UV-C radiation. The neat epoxy is a highly hydrophobic material with a water contact angle of 99° ± 2.3°. For all grades of xGnP, the presence of graphene nanoplatelets decreases the value of the contact angle at the nanocomposite surface, and the value decreases further as the concentration of xGnP becomes higher.

After exposure to UV-C radiation, the contact angle of epoxy/xGnP-C750 nanocomposite films remains substantially constant. This result is more evident in Fig. 4, which shows the contact angle values at equilibrium for the epoxy/xGnP-

C750 films as a function of nanoplatelets loading, before and after 9 h of UV-C exposure.

Before exposure, the average WCA values at different loadings (0.5, 1, 3, 5 and 7 wt%) are in the range of 85.3° - 89.6° with standard deviations in the range of 0.9° - 3.1°. After 9 h of UV-C exposure, the WCA values remain broadly unchanged, within the standard deviation limits, at concentrations from 1 wt% to 5 wt% of nanofiller. Only at concentrations of 0.5 wt% there is a measurable difference of water contact angle values before and after UV-C radiation, passing from 89.4 ± 3.1° pre UV-C to 83.8 ± 2.3° post UV-C. These results indicate that the hydrophobic nature of the surface of epoxy/xGnP-C750 nanocomposite films remains almost unaffected by the exposure to UV-C.

On the other hand, different results were obtained for the nanocomposite films fabricated with thicker graphene nanoplatelets, such as grades M5 and H5. In these cases, the water contact angle at equilibrium tends to increase after 9 hours of UV-C exposure time, especially at higher concentrations (3-7 wt%). Further, it can be noted that with the increase of the nanoplatelets thickness, the difference of WCA before and after ultraviolet radiation increases. Such difference becomes even larger at higher graphene nanoplatelet concentration. In particular, this effect is most evident for the thicker M5 and H5 graphene nanoplatelets at 7 wt% concentration.

The above results from the water contact angle analysis can be explained considering the chemical and physical changes of the nanocomposite films due to the interaction with UV-C light. The epoxy matrix under UV-C exposure

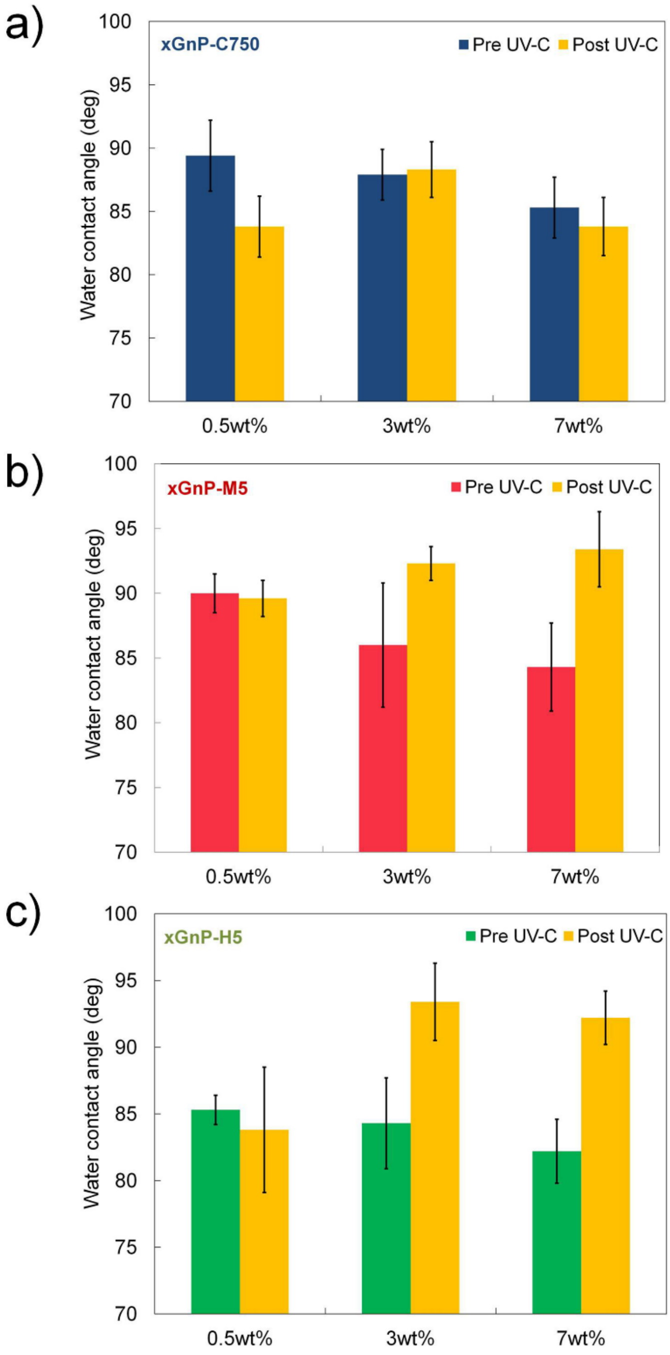

Fig. 3. Water contact angle values at equilibrium for epoxy/xGnP nanocomposite films before and after UV-C exposure. Nanocomposite films with different concentrations of xGnP (0.5, 3, and 7 wt%) and different nanoplatelets grades: (a) epoxy/xGnP-C750; (b) epoxy/xGnP-M5; (c) epoxy/xGnP-H5.

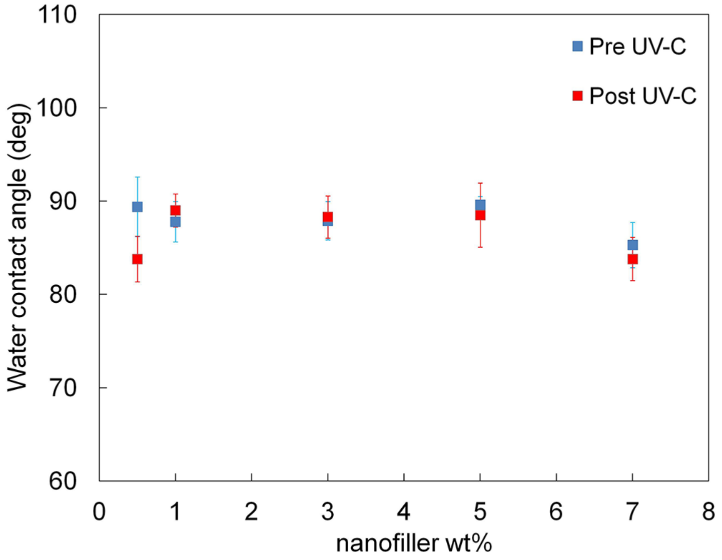

Fig. 4. Water contact angle values at equilibrium on epoxy/xGnP-C750 nanocomposite films with different nanoplatelet loading, before and after 9 h exposure to UV-C radiation.

undergoes a photo-chemical degradation that occurs by cleavage of the covalent bonds to form highly reactive radicals [26, 27]. After the photolysis, the free radicals can react with oxygen forming peroxy radicals. In the presence of graphene nanoplatelets, the number of the possible chemical reactions with the free radicals increases and the interaction with the water drop can vary strongly [28]. Furthermore, the UV-C rays are capable of realizing a physical etching of the nanocomposite surface. As for the size of xGnPs, smaller graphene nanoplatelets tend to disperse better in the host matrix making the nanocomposite mixture more homogeneous. On the contrary, larger nanoplatelets tend to re-agglomerate creating significant graphene-bundles embedded in the matrix. As a consequence, in the case of small nanofillers, such as xGnP-C750, the surface roughness of the film after radiation exposure is almost unchanged and, therefore, the water contact angle remains nearly constant. For the other two grades, xGnP-M5 and xGnP-H5, the surface roughness is expected to be greater, and consequently the water contact angle increases.

2.3.2 Electrical measurements of epoxy/xGnP films

Fig. 5 shows the change of normalized electrical resistance ($\Delta R^*_{normalized}$) of nanocomposite films deposited on Mylar substrate at different concentrations of graphene nanoplatelets (xGnP) as a function of the UV-C exposure time. In all cases, the measured resistance R_p^* decreases with the exposure time, and so the electrical resistance variation tends to become more negative. This effect is more significant for those films with the lower concentration of graphene nanoplatelets, whereas films at 7 wt% loading of xGnP (all three types tested in this work) show the lowest variation of electrical resistance over the UV-C exposure. This can be attributed to the fact that nanocomposite films with lower xGnP concentrations have a lower content of nanoparticles in the epoxy matrix and so the degradation at the level of the matrix is the predominant effect under UV-C radiation. In addition, results in Fig. 4 indicate that the nanocomposite films show the largest decrease in electrical resistance during the first 4 hours of exposure. After this time range, the values of $\Delta R^*_{normalized}$ decrease more slowly, reaching an equilibrium value at which the different effects of polymer degradation and UV-induced chemical reactions at the interface between polymer and graphene surface are less evident.

Fig. 6 shows the surface conductive of the nanocomposite films as a function of the nanofiller concentration, before and after 9 h exposure to UV-C radiation. As expected, the surface conductivity of the as-prepared films increases with the loading of graphene nanoplatelets for all types of nanoparticles. After UV-C irradiation, there is a consistent increase of surface conductivity at all xGnP concentrations. This result is in agreement with the above considerations related to the wettability of the films before and after UV-C exposure, that is the polymer matrix of the nanocomposites is preferentially degraded with respect to the nanofillers. In fact, the erosion of the resin results in a more conductive surface of the nanocomposites due to the exposure of the graphene nanoplatelets.

Results from measurements of electrical impedance spectroscopy are in Fig. 7, where the surface resistivity of nanocomposite films with different types of xGnP (concentrations of 0.5 and 7 wt%) is plotted as a function of the testing frequency, before and after 9 hours of UV-C exposure. For all films, the surface resistivity decreases with the testing frequency following a linear trend both before and after radiation exposure. In particular, the surface resistivity after UV-C is smaller than that before exposure, and the difference is larger at the lowest frequencies. This trend is particularly evident at xGnP concentration of 0.5 wt% and frequency of 1 kHz, where the surface resistivity reduces of about two order of magnitude.

2.4 Conclusions

Epoxy/graphene nanocomposite films were fabricated by spin-coating process using Mylar as substrate and the effects of UV-C radiation on the surface properties were investigated in terms of wettability and electrical properties. In particular, three different grades of xGnP were used for the film fabrication at different loadings by weight. It was observed that the wettability of the nanocomposite films increases when adding the graphene nanoplatelets for all grades of xGnP. After exposure to UV-C, the average water contact angle of the irradiated nanocomposite films depends on the geometrical characteristics of the nano-reinforcement. In the case of the thinner graphene nanoplatelets (xGnP-C750), the WCA values remain almost constant even after 9 hours of UV-C exposure. On the contrary, in case of the thicker graphene nanoplatelets (grades M5 and H5), it was observed that the water contact angle at equilibrium increases after 9 hours of UV-C exposure, and the difference becomes larger as the thickness of graphene flakes increases. These results show that the hydrophobic nature of the epoxy/graphene nanocomposite films tends to increase after exposure to UV-C radiation.

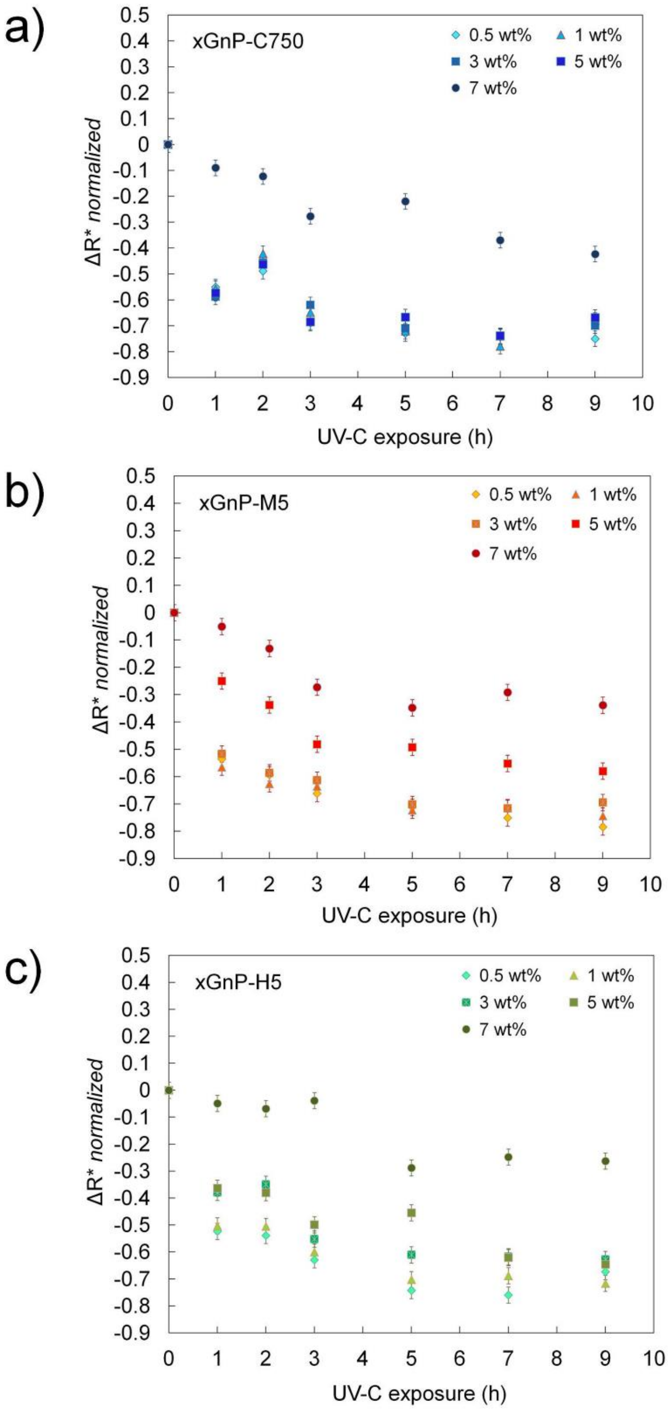

Fig. 5. ΔR**normalized* values for epoxy/xGnP films as a function of exposure time to UV-C radiation. Nanocomposite films with different concentrations of xGnP (0.5, 1, 3, 5 and 7 wt%) and different nanoplatelets grades: (a) epoxy/xGnP-C750; (b) epoxy/xGnP-M5; (c) epoxy/xGnP-H5.

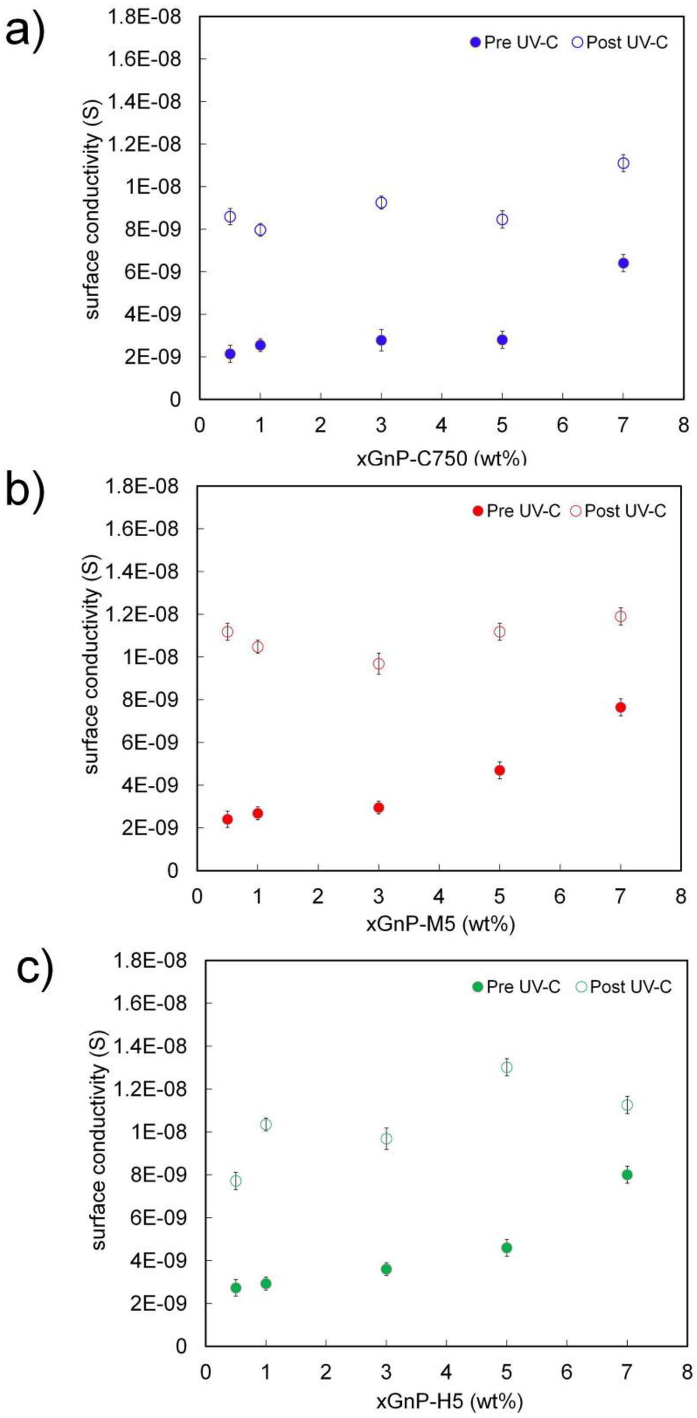

Fig. 6. Surface conductivity values of epoxy/xGnP films before and after 9 h exposure to UV-C radiation as a function of graphene nanoplatelets concentration (0.5, 1, 3, 5 and 7 wt%) and different grades: (a) epoxy/xGnP-C750; (b) epoxy/xGnP-M5; (c) epoxy/xGnP-H5.

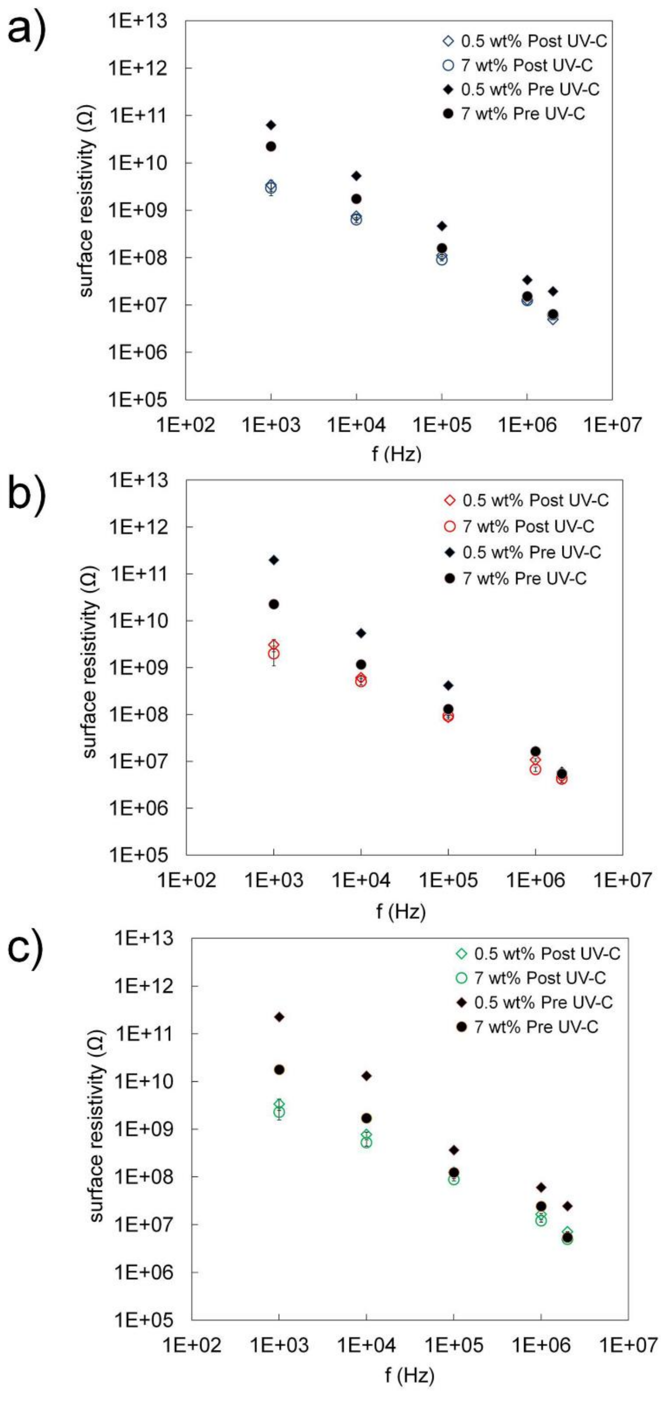

Fig. 7. Surface resistivity values of epoxy/xGnP films at concentration of graphene nanoplatelets of 0.5 and 7 wt%, before and after 9 hours of UV-C exposure, as a function of frequency and different grades: (a) epoxy/xGnP-C750; (b) epoxy/xGnP-M5; (c) epoxy/xGnP-H5.

When looking at the electrical properties of the nanocomposite films, the surface electrical resistivity decreases with the increasing of nanofiller loadings, as it would be expected, and also during exposure to the UV-C radiation. This latter effect is more significant for films with lower concentration of graphene nanoplatelets, whereas films at 7 wt% loading of xGnP (all three types tested in this work) show the lowest variation of electrical resistance over the UV-C exposure. This phenomenon can be related to the higher content of polymer, for the nanocomposites at lower concentration of xGnP, as the polymer matrix erosion contributes to create a more conductive surface due to the exposure of graphene nanoplatelets. Results from the electrical impedance spectroscopy experiments showed that the surface resistivity decreases with the testing frequency following a linear trend both before and after radiation exposure, and that this behavior is common for all nanocomposite films. Further, the surface resistivity of the films after UV-C irradiation is always smaller than that before exposure regardless of the xGnP size, confirming that the dominant effect of the UV-C radiation is a selective polymer matrix erosion that gives rise to an increase of the electrical conductivity at the film surface.

2.5 References

[1] Choi HS, Lee J, Cho KS, Kwak YS, Cho IH, Park YD, et al. Analysis of GEO spacecraft anomalies: Space weather relationships. Space Weather 2011;9.

[2] Thirsk R, Kuipers A, Mukai C, Williams D. The space-flight environment: the International Space Station and beyond. Canadian Medical Association Journal 2009;180:1216-20.

[3] Hastings D, Garrett H. Spacecraft-environment interactions: Cambridge university press; 2004.

[4] Belk CA, Robinson JH, Alexander MB, Cooke WJ, Pavelitz SD. Meteoroids and orbital debris: effects on spacecraft. NASA Technical Report1997.

[5] Dever J, Banks B, de Groh K, Miller S. Degradation of spacecraft materials. Handbook of environmental degradation of materials 2005:465-501.

[6] Dever JA, Miller SK, Sechkar EA, Wittberg TN. Space environment exposure of polymer films on the materials international space station experiment: results from MISSE 1 and MISSE 2. High Performance Polymers 2008;20:371-87.

[7] Miyakita T, Hatakenaka R, Sugita H, Saitoh M, Hirai T. Development of a new multi-layer insulation blanket with non-interlayer-contact spacer for space cryogenic mission. Cryogenics 2014;64:112-20.

[8] Xie T, He Y-L, Tong Z-X. Analysis of insulation performance of multilayer thermal insulation doped with phase change material. International Journal of Heat and Mass Transfer 2016;102:934-43.

[9] Johnson L, Young R, Montgomery E, Alhorn D. Status of solar sail technology within NASA. Advances in Space Research 2011;48:1687-94.

[10] Peloni A, Barbera D, Laurenzi S, Circi C. Dynamic and structural performances of a new sailcraft concept for interplanetary missions. The Scientific World Journal 2015;2015.

[11] Laurenzi S, Pizzurro S, Circi C. Solar sails: A comparative study between kapton HN and kapton B membranes. Proceedings of the International Astronautical Congress, IAC2014. p. 6161-6.

[12] Sotgiu G, Schirone L. Microstructured silicon surfaces for field emission devices. Applied Surface Science 2005;240:424-31.

[13] Asmatulu R, Mahmud GA, Hille C, Misak HE. Effects of UV degradation on surface hydrophobicity, crack, and thickness of MWCNT-based nanocomposite coatings. Progress in Organic Coatings 2011;72:553-61.

[14] Laurenzi S, Sirilli M, Albano M, Marchetti M. Outgassing in carbon nanostructured films on mylar substrate. International Astronautical Federation, IAF2014.

[15] Banks BA, De Groh KK, Miller SK. Low earth orbital atomic oxygen interactions with spacecraft materials. Materials Research Society Symposium Proceedings2005. p. 331-42.

[16] Vulpetti G, Santoli S, Mocci G. Preliminary investigation on carbon nanotube membranes for photon solar sails. Journal of the British Interplanetary Society 2008;61:284-9.

[17] Vulpetti G. Reaching extra-solar-system targets via large post-perihelion lightness-jumping sailcraft. Acta Astronautica 2011;68:636-43.

[18] Soldano C, Mahmood A, Dujardin E. Production, properties and potential of graphene. Carbon 2010;48:2127-50.

[19] Balandin AA. Thermal properties of graphene and nanostructured carbon materials. Nat Mater 2011;10:569-81.

[20] Novoselov KS, Falko VI, Colombo L, Gellert PR, Schwab MG, Kim K. A roadmap for graphene. Nature 2012;490:192-200.

[21] Fernandez M, Shi H, Barnard AS. Geometrical features can predict electronic properties of graphene nanoflakes. Carbon 2016;103:142-50.

[22] Ansari S, Giannelis EP. Functionalized graphene sheet—Poly (vinylidene fluoride) conductive nanocomposites. Journal of Polymer Science Part B: Polymer Physics 2009;47:888-97.

[23] Eda G, Chhowalla M. Graphene-based composite thin films for electronics. Nano Letters 2009;9:814-8.

[24] Clausi M, Santonicola MG, Laurenzi S. Fabrication of carbon-based nanocomposite films by spin-coating process: An experimental and modeling study of the film thickness. Composites Part A: Applied Science and Manufacturing 2016;88:86-97.

[25] Clausi M, Santonicola MG, Laurenzi S. Steady-shear rheological properties of graphene-reinforced epoxy resin for manufacturing of aerospace composite films. VIII International Conference on “Times of Polymers and Composites: From Aerospace to Nanotechnology": AIP Publishing; 2016. p. 020024.

[26] Nikafshar S, Zabihi O, Ahmadi M, Mirmohseni A, Taseidifar M, Naebe M. The effects of UV light on the chemical and mechanical properties of a transparent epoxy-diamine system in the presence of an organic UV absorber. Materials 2017;10:180.

[27] Yousif E, Haddad R. Photodegradation and photostabilization of polymers, especially polystyrene. SpringerPlus 2013;2:398.

[28] Toto E, Palombi M, Laurenzi S, Santonicola MG. Functional nanocomposites with graphene-DNA hybrid fillers: Synthesis and surface properties under UV irradiation. Ceramics International 2019;45:9631-7.

Chapter 3 - *Spray coating process of MWCNT/epoxy nanocomposite films for aerospace applications: effects of process parameters on surface electrical properties* [2]

---

[2] Taken from the publication: 'Spray coating process of MWCNT/epoxy nanocomposite films for aerospace applications: effects of process parameters on surface electrical properties', Acta Astronautica, vol. 159, 429-439, 2019 (doi.org/10.1016/j.actaastro.2019.01.043)'.

Abstract

Nanocomposite coatings on flexible membranes possess many interesting properties useful in aerospace applications, such as thermal blankets and charging mitigation layers. However, their fabrication is not trivial and the overall performance is strongly dependent on the manufacturing process, since it influences the filler distribution and so the homogeneity of the coated film. In this work, carbon nanotube/epoxy nanocomposite films were deposited on Mylar substrates by spray coating process. The effects of the process parameters on the morphology and on the electrical properties of the nanocomposite films were investigated. In particular, the influence of the nozzle diameters and the distance between the nozzle and the target substrate, as well as the concentration of the multiwalled carbon nanotubes (MWCNT) were studied. The electrical properties of the MWCNT/epoxy nanocomposite surfaces were determined using impedance spectroscopy in the frequency range from 20 Hz to 2 MHz. The analysis was performed on samples extracted from different regions of the nanocomposite films, in order to assess their property homogeneity.

3.1 Introduction

Carbon-based nanocomposite films are extensively studied due to their exceptional multifunctional properties [1-5]. In the aerospace field, the manufacturing of nanocomposite films is primarily focused on achieving superior properties of the engineered materials with significant weight saving and surpassing the electrical, thermal and mechanical properties of traditional materials. Possible applications of nanocomposite films include radiation protective and thermo-optical coatings [6-8], UV sensors [4, 9, 10], radar absorbing and electromagnetic interference shields [11-13]. The functional properties of the nanocomposite films are determined by the type of embedded carbon nanoparticles, and they are highly influenced by the selected manufacturing process [14-16]. Depending on the scope, various types of carbon nanoparticles with different thicknesses, specific surface areas and aspect ratios have received great attention as fillers in modern composite manufacturing in order to increase the electrical and thermal conductivity, and mechanical properties of the resulting composite materials [17-19]. The dispersion of carbon nanoparticles in the polymer matrix [20, 21] and the film deposition process [22, 23] are important steps of the manufacturing, which need to be carefully designed in order to obtain homogeneous and uniform nanocomposite films, and so to improve their functional properties. Spray coating is a deposition technique that has been adopted in the manufacturing industry to replace the spin coating process, with the advantage to obtain coatings on larger and non-planar surfaces [24-27]. The spray coating process consists in applying an external pressure (usually up to a maximum of 3.5 bar), which forces the resin (printing ink) through the exit nozzle of an aerograph. Yet, another interesting feature of spray coating is that the process involves numerous depositions of small droplets, while other printing/coating methods deposit a solution in a single step to form a film. In this way, the spray coating provides a method to attain innovative structures as it allows to deposit finely tuned layers by controlling the feeding rate, the applied pressure, the spraying distance, as well as the composition of the sprayed mixture. Vak [28] recognizes two classification types of spray coating, wet and dry. The wet spray coating can be distinguished by the existence of a fluid layer of resin on the substrate during and shortly after the spraying, which can be achieved either with a slow rate/longer exposure time of the substrate to the jet, or by not applying heat to it. On the other hand, the dry spray coating technique consists in short jets of resin on a heated substrate.

The main objective of the present work is to investigate the role of spray coating parameters in setting the morphology and the electrical performance of MWCNT-based nanocomposite films. The films were fabricated on Mylar substrate with epoxy resin reinforced with carbon nanoparticles at different loadings, in the range 0.5-2 wt%, followed by a heat cure cycle. A flexible Mylar membrane was chosen as substrate for the nanocomposites because it is largely used in many spacecraft subsystem [29-31], especially as thermal barriers [32-34]. The realization of an electrically-conductive coating on Mylar substrate can help to mitigate several detrimental effects due to interaction of the subsystem, for example a multi-layer-insulation (MLI), with the aerospace environments. Indeed, the major problems related to the dielectric nature of MLI, including Mylar, are electromagnetic interferences [35] and charging phenomenon [36], which are a serious risk for the spacecraft operation and integrity. In this context, CNT-based nanocomposite films fabricated on Mylar, which can be easily integrated with MLIs, represent a tempting solution because of the well-known electromagnetic absorption and electrical conductive properties of CNT-based materials [8, 37].

In a first step, the spraying process will be investigated in order to understand how the different parameters influence the range and quality of the deposited coatings. Two different nozzle diameters of the spray gun, which are typically used in industrial processing, different target spraying distances and concentration of carbon nanotubes will be investigated. Further, the electrical properties of the deposited nanocomposite films on Mylar substrate are investigated in relation to the spraying process parameters. In particular, we analyzed the uniformity of the surface electrical conductivity by comparing samples extracted from the sprayed nanocomposite films at different locations.

3.2 Experimental

3.2.1 Materials

The carbon nanotubes used in this study were pristine MWCNTs (NC7000 series) from Nanocyl S.A. (Belgium), which were synthesized via the catalytic chemical vapor deposition process. MWCNTs were of purity 90%, with average outer diameter of 9.5 nm, average length of 1.5 µm, and specific surface area in the range of 250-300 m^2/g, as specified by the supplier. Prime 20LV epoxy resin with slow hardener supplied by Gurit (UK) was chosen as the polymer matrix. Mylar sheets (43 cm × 35 cm) with thickness of 130 µm were used as substrates for the nanocomposite films deposition.

3.2.2 Fabrication of carbon nanotube/epoxy nanocomposite films

Carbon nanocomposites films were prepared by spray coating the mixture of MWCNT and epoxy resin, followed by thermal curing in oven at 50 °C for 16 h. Nano-reinforced epoxy mixtures with MWCNTs at 0.5 wt%, 1 wt%, and 2 wt% were used. The mixtures were mechanically stirred for 15 min at room temperature. After the mixing, in order to further improve the filler dispersion in the resin, the blends were sonicated with a VCX 500 ultrasonic probe (Ultra-Cell, Sonics & Materials Inc., USA) equipped with a titanium alloy probe of 13-mm tip diameter (40% energy, 2-s on/off pulses for 1 min). The blends were additionally sonicated in an ultrasonic water bath (FALC Instruments, Italy) for 60 min at 40 °C. Next, the curing agent was gently added to the blend in the ratio of epoxy-to-curing agent of 100:26 by weight.

The spraying process was carried out according to the scheme in Fig. 1. All spraying tests were conducted using a perpendicular arrangement with respect to the surface target (Mylar substrate). In order to investigate the effects of the nozzle diameter on the spray-coated films, two different nozzle diameters were used: 1.2 mm (nozzle 1) and 1.5 mm (nozzle 2). The distance between the nozzle and the Mylar substrate (named target distance hereafter) was fixed at 10 cm, 15 cm, or 20 cm. The spraying time was set at 15 s after conducting preliminary tests with the unloaded resin, and observing that this time guarantees that the covered area does not change in time and the thickness is uniform. Regarding the pressure applied to the resin bucket, this was fixed at 3 bar as recommended by the manufacturer and as typically used in industrial processes.

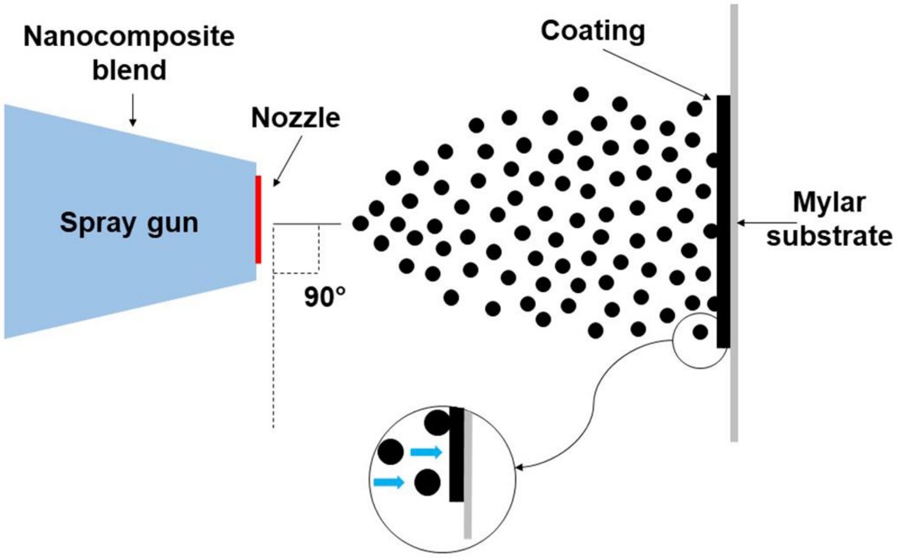

Fig. 1. Schematic of spray coating process for the fabrication of MWCNT/epoxy nanocomposite films on Mylar substrate.

3.2.3 Characterization methods

The rheological properties of the nanocomposite epoxy fluids were measured at room temperature (25 °C) using a rotational, concentric cylinder viscometer (Visco Star plus, Fungilab, Spain). Viscosity measurements were repeated at different rotational velocities and in triplicates.

Electrical impedance spectroscopy (EIS) in the frequency range from 20 Hz to 2 MHz was carried out using an Agilent E4980A Precision LCR Meter (Agilent Technologies, USA) in a two-electrode configuration on the nanocomposite surface (Fig. 2).

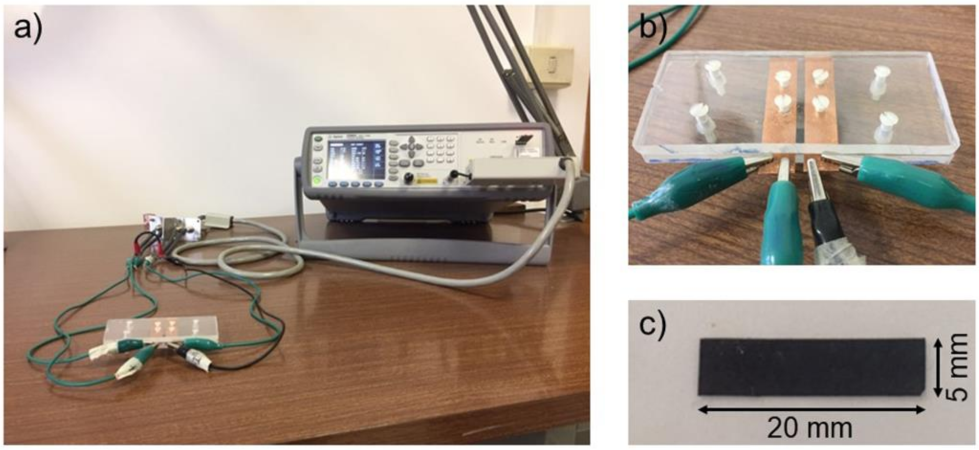

Fig. 2. Set-up for electrical measurements: a) LCR instrument used for the electrical measurements; view of a nanocomposite sample (c) placed between two tightly screwed insulating plates with two copper plates used as electrodes (b).

The measurement cell was custom-made and consisted of two tightly screwed insulating plates (Plexiglas), with two parallel copper electrodes (1-cm wide) positioned at a distance l from each other and fixed onto one side of the cell (Fig. 2b). Nanocomposite coatings on Mylar were cut to strips of size 20 mm x 5 mm (Fig. 2c). The thickness of the nanocomposites films (t) was measured using a digital caliper with accuracy of 0.01 mm, after subtracting the substrate thickness. The measured electrical impedance (Z) was normalized with respect to the film thickness ($Z_{normalized} = Z/t$). In addition, the electrical resistance values (R_p) were directly measured with the LCR meter setting the parallel-equivalent circuit model. The impedance (Z) and the resistance values (R_p) reported are the mean values of at least twenty measurements. The surface conductivity (σ_s) of the nanocomposite films was determined as:

$$\sigma_s = 1/\rho_s \qquad (1)$$

where ρ_s is the surface resistivity calculated according to the ASTM D257-07 standard:

$$\rho_s = R_p \cdot P/l \qquad (2)$$

with P as the electrode effective perimeter and l the distance between the two electrodes.

In order to investigate the homogeneity of the surface electrical properties, five samples were taken in different regions of the manufactured coatings and tested. Fig. 3 shows the extrapolation scheme for the five strips that were analyzed for each nanocomposite film. The top, bottom, right and left strips were cut at a distance of 30 mm from the central strip.

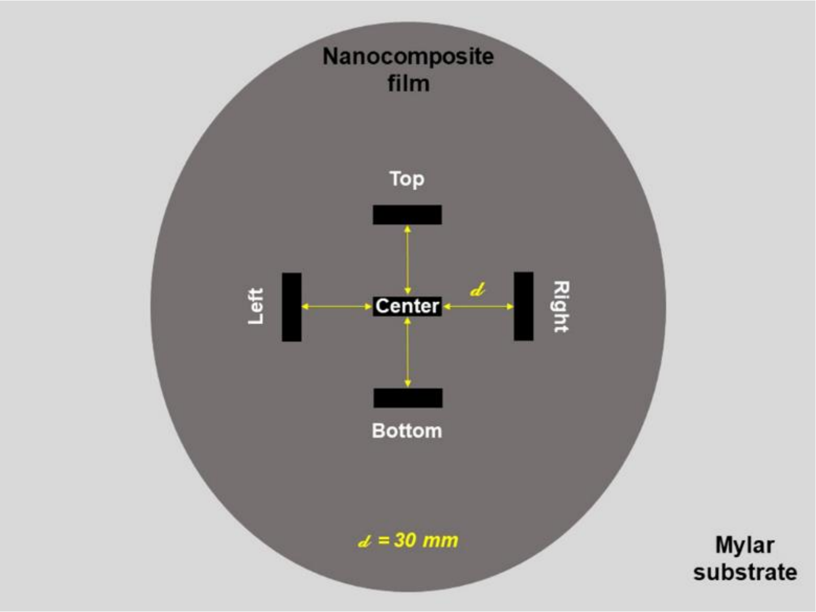

Fig. 3. Position and labeling of MWCNT/epoxy samples extracted from the sprayed nanocomposite film.

3.3 Results and discussion

Many process variables can influence the features of films deposited using the spraying coating technique. Some variables are related to the spray gun assembly, such as its diameter and shape of the nozzle, whereas others are linked to the process parameters and to the nature of both nanocomposite blend and substrate onto which the film is deposited. The process parameters are the air pressure, the spraying time, the distance and direction of the nozzle from the target surface. One major property that affects the spraying process is the viscosity of the blend. In the case of nanocomposites, the blend viscosity is strongly dependent on the concentration of the nanoparticles [15, 38], and can be highly influenced by their degree of dispersion inside the resin matrix. In this work, we investigated the effects of the above-mentioned parameters on the morphology of the spray-coated nanocomposite films, in terms of covered area, thickness and uniformity. Finally, the homogeneity of the nanocomposite films was investigated with respect to their surface electrical properties.

3.3.1 Influence of spray coating parameters on film morphology

The viscosity of the MWCNT/epoxy nanocomposites blends was measured as a function of the carbon nanotube concentration (Fig. 4). The viscosity is strongly dependent on the filler content, increasing exponentially with it and reaching the value of 3000 mPa.s already at 2.5 wt% of MWCNTs. Based on these results, concentrations up to 2 wt% were considered in this study.

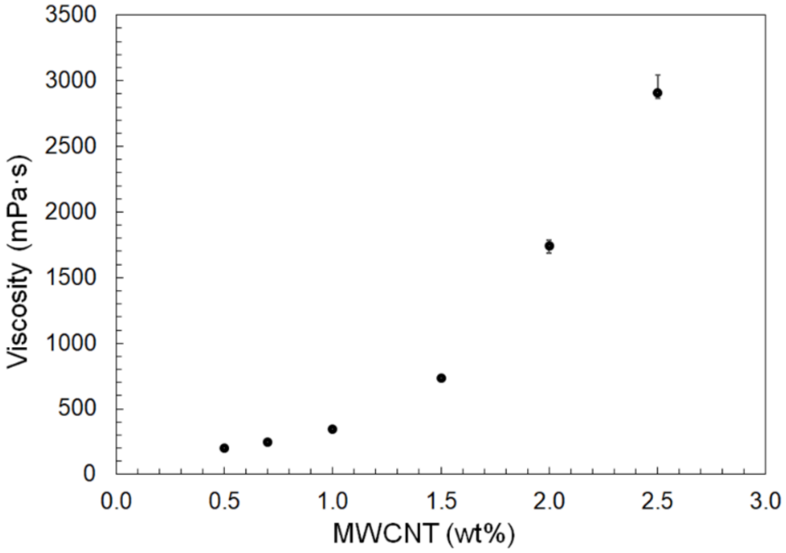

Fig. 4. Mean values of viscosity for MWCNT/epoxy nanocomposite blends at different filler loadings.

Fig. 5 shows the mean values of covered area by the sprayed MWCNT/epoxy nanocomposite films (average of 12 sprayed films per type) as a function of the target distance, for different concentrations of MWCNT (0.5, 1 , and 2 wt%) and for both nozzle types, nozzle 1 and nozzle 2 with diameter of 1.2 mm and 1.5 mm, respectively.

These nozzles allowed to obtain quasi-circular or elliptical depositions, with a covered area that tends to decrease upon increase of the target distance and upon increase of the MWCNT concentration. Results show that for a fixed distance and for a given MWCNT concentration, nozzle 2 produced larger covered areas than those realized with nozzle 1. This result is quite intuitive because the flow rate of the nanocomposite blends is proportional to the diameter of the nozzle. The effect of the nozzle diameter on the covered area is more evident at 0.5 wt% of MWCNT, which corresponds to lowest blend viscosity (about 200 mPa·s).

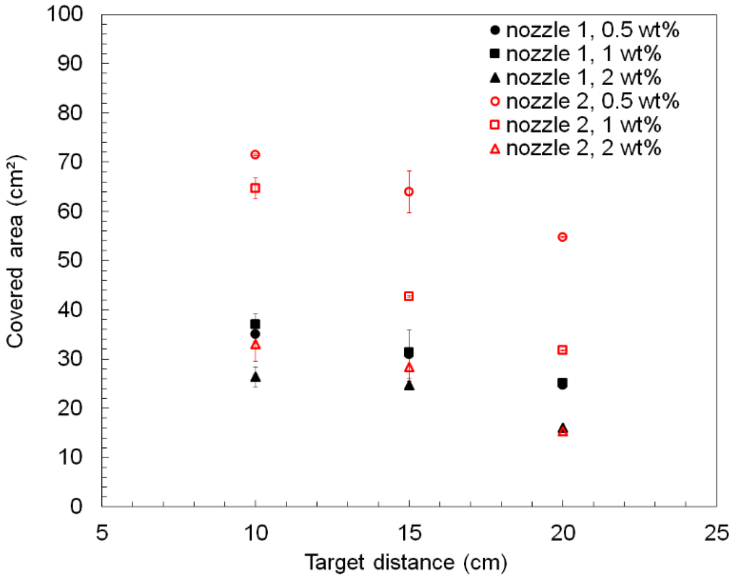

Fig. 5. Mean values of covered area for sprayed MWCNT/epoxy films at loadings of 0.5, 1 and 2 wt% of MWCNTs, as a function of target distances (10 cm, 15 cm, and 20 cm) for nozzle 1 (diameter 1.2 mm) and nozzle 2 (diameter 1.5 mm). Data shown are the average of 12 nanocomposite films per type.

For each fixed distance, the covered areas obtained using nozzle 2 are about 50% larger than those fabricated with nozzle 1. With the increase of the concentration of nanofillers, which means an increase of blend viscosity, the differences between the covered areas realized with the two nozzles decreases. Further, such differences decrease upon increasing the distance between the nozzle and the target substrate. At a nozzle-to-target distance of 20 cm, the difference between the covered areas deposited with the two nozzles becomes not detectable for the nanocomposites with 2 wt% of MWCNT. Indeed, we observed that the diameter of the nozzle significantly influences the extension of the covered area only at low concentrations of nanofiller, when the viscosity is sufficiently low. This behavior can be explained with the increase of the flow rate due to the larger diameter. In addition, if the blend has a low viscosity, there will be a high flow rate due to a lower degree of interaction among particles, and the fluid will flow more freely. As a consequence, the covered area fabricated with a blend with lower viscosity is larger than one obtained at higher viscosity, especially at short distance of the nozzle from the target.

Tables 1-3 summarize the thicknesses of the MWCNT/epoxy nanocomposite films extracted from the spray-coated samples at different positions, for the MWCNT concentrations (0.5, 1, 2 wt%) and nozzle-to-target distances (10, 15, 20 cm) considered in this investigation. Results are reported for both nozzles, nozzle 1 (diameter 1.2 mm) and nozzle 2 (diameter 1.5 mm). From Table 1, which refers to the nanocomposite films with 0.5 wt% of MWCNT, it is noted that the average thickness value is of the order of 250 µm with a variation of few tens of microns. The film thickness is quite similar regardless of the location of the extracted

Table 1. Thicknesses of MWCNT/epoxy nanocomposite films with 0.5 wt% of MWCNT fabricated by nozzle 1 (diameter 1.2 mm) and nozzle 2 (diameter 1.5 mm) at different target distance.

	Thickness (mm) / Nozzle 1			**Thickness (mm) / Nozzle 2**		
Sample position	**10 cm**	**15 cm**	**20 cm**	**10 cm**	**15 cm**	**20 cm**
Top	0.23± 0.02	0.21± 0.04	0.18± 0.03	0.24± 0.03	0.28± 0.02	0.25± 0.02
Bottom	0.28± 0.03	0.24± 0.06	0.22± 0.03	0.22± 0.01	0.31± 0.05	0.28± 0.01
Center	0.24± 0.01	0.24± 0.01	0.19± 0.02	0.22± 0.02	0.31± 0.01	0.27± 0.02
Right	0.26± 0.01	0.24± 0.03	0.17± 0.01	0.24± 0.01	0.30± 0.02	0.26± 0.03
Left	0.25± 0.02	0.25± 0.01	0.24± 0.03	0.26± 0.03	0.29± 0.04	0.22± 0.01

Table 2. Thicknesses of MWCNT/epoxy nanocomposite films with 1 wt% of MWCNTs fabricated by nozzle 1 (diameter 1.2 mm) and nozzle 2 (diameter 1.5 mm) at different target distance.

	Thickness (mm) / Nozzle 1			**Thickness (mm) / Nozzle 2**		
Sample position	**10 cm**	**15 cm**	**20 cm**	**10 cm**	**15 cm**	**20 cm**
Top	0.30± 0.01	0.30± 0.01	0.25± 0.01	0.26± 0.04	0.19± 0.04	0.18± 0.01
Bottom	0.30± 0.02	0.29± 0.01	0.25± 0.01	0.27± 0.01	0.22± 0.08	0.20± 0.01
Center	0.31± 0.01	0.33± 0.03	0.26± 0.01	0.23± 0.02	0.20± 0.04	0.19± 0.01
Right	0.32± 0.02	0.30± 0.01	0.21± 0.02	0.24± 0.03	0.18± 0.04	0.18± 0.02
Left	0.30± 0.01	0.34± 0.01	0.20± 0.02	0.25± 0.01	0.21± 0.03	0.22± 0.04

Table 3. Thicknesses of MWCNT/epoxy nanocomposite films with 2 wt% of MWCNTs fabricated by nozzle 1 (diameter 1.2 mm) and nozzle 2 (diameter 1.5 mm) at different target distance.

	Thickness (mm) / Nozzle 1			**Thickness (mm) / Nozzle 2**		
Sample position	**10 cm**	**15 cm**	**20 cm**	**10 cm**	**15 cm**	**20 cm**
Top	0.45± 0.06	0.35± 0.01	0.19± 0.02	0.36± 0.03	0.27± 0.02	0.22± 0.01
Bottom	0.40± 0.08	0.24± 0.02	0.18± 0.01	0.39± 0.03	0.30± 0.01	0.19± 0.02
Center	0.44± 0.05	0.30± 0.03	0.26± 0.03	0.33± 0.04	0.34± 0.03	0.23± 0.04
Right	0.42± 0.02	0.23± 0.02	0.20± 0.02	0.32± 0.04	0.27± 0.01	0.19± 0.02
Left	0.40± 0.10	0.24± 0.04	0.18± 0.01	0.38± 0.04	0.27± 0.02	0.20± 0.04

samples, indicating a high uniformity of the spray-coated films. This result was obtained for each target distance, and for all films fabricated with both nozzles. In the case of nozzle 1, we can observe a slight decrease of the film thickness with the increasing of the target distance, which can be explained by the fact that the inertia of the droplets is not sufficient for the entire jet to reach the surface of the substrate. This result is consistent with the reduction of the covered area, as noted also in Fig. 5. In the case of nozzle 2, which has a larger diameter than nozzle 1, the film thickness appears to be quite independent from the target distance. The increment of both flow rate and jet diameter allows to obtain films with constant thickness in relation to the target distances considered in this study, even if the covered area during the process decreases (Fig. 5).

Upon increasing the concentration of MWCNTs, hence the viscosity of the nanocomposite blends, the film thickness tends to increase (Tables 2 and 3). Table

2 reports the film thicknesses measured for the nanocomposite films at 1 wt% of MWCNTs. In this case, we observe an increment of the thicknesses with respect to the lower concentration (0.5 wt%) of MWCNTs, and the effects of the nozzle diameter on the film thickness are less evident than for the previous case. In particular, in the case of nozzle 1, no significant differences can be detected in the thicknesses of films fabricated adopting 10 cm and 15 cm target distances, whereas a thickness reduction of about 10% is observable for a target distance of 20 cm. At MWCNT concentration of 1 wt%, the nozzle 2 produces films with smaller thickness than those realized with nozzle 1, and the thickness is roughly the same at target distances of 15 cm and 20 cm. The same trend of film thicknesses was obtained for the nanocomposite films at 2 wt% of MWCNTs (Table 3). As for the previous case, the larger thickness is obtained for the films fabricated using nozzle 1 at a target distance of 10 cm, reaching an average value of 420 µm. In all other cases, the film thickness is comparable to that of the films at 1wt% of MWCNTs fabricated using equivalent conditions.

3.3.2 Analysis of electrical properties of spray-coated nanocomposites

The electrical properties of the MWCNT/epoxy nanocomposite films deposited by spray coating were investigated using electrical impedance spectroscopy (EIS) in the frequency range 20 Hz – 2 MHz, considering samples extracted from the entire covered area as previously illustrated (Fig. 3). All reported impedance data were normalized with respect to the nanocomposite film thickness. Fig. 6 shows the mean values of the normalized impedance ($Z_{normalized}$) of the nanocomposite samples fabricated at fixed 10-cm target distance, using both nozzles and different

MWCNT loadings. It is noted that at 0.5 wt% of MWCNTs (Fig. 6a-b), the $Z_{normalized}$ is almost independent from the diameter of nozzle used for the processing. In both cases, the normalized electrical impedance decreases linearly with the frequency. The same trend is obtained for samples fabricated with the nozzle 1 (diameter 1.2 mm) and loaded with 1 wt% of MWCNTs (Fig. 6c). On the other hand, the equivalent samples fabricated using nozzle 2 (Fig. 6d) are characterized by impedance values that are constant up to 10 kHz, and start to decrease at higher frequencies. In general, for all the nozzle-to-target distances that we investigated, the slope of the $Z_{normalized}$ curves tends to decrease as the MWCNT concentration increases, with an overall decrease of the impedance values in the lower frequency region, which is in agreement with an increase of the nanocomposites electrical conductivity at higher MWCNT concentrations (Fig. 6e and Fig. 6f).

The behavior described above can be explained with the concurrence of two phenomena, deep bed filtration and cake filtration [39], which are amplified when the nozzle diameter is smaller. During the spraying process, the nanoparticles embedded in the resin are gradually captured by the walls of the nozzle, even if the nanoparticles are smaller than the channel (deep bed filtration). The continuous capture of nanoparticles narrows the available nozzle diameter, and may ultimately result in cake filtration. This latter process occurs when the particle size is larger than the nozzle diameter. In addition, the unavoidable nanoparticle entanglements, that are a consequence of the surface interactions and van der Waals forces among the carbon nanotubes, contribute to enhance filtration phenomena. It is noted that for the nanocomposite samples with larger impedance values at low frequencies (0.5 wt% of MWCNTs with both types of nozzle, and 1 wt% of MWCNT with nozzle 1), the EIS data were acquired only in the frequency range above 150 Hz (Fig. 6a, 6b, and 6c). This was due to the presence of large errors in the impedance values being near the instrument measurement limit.

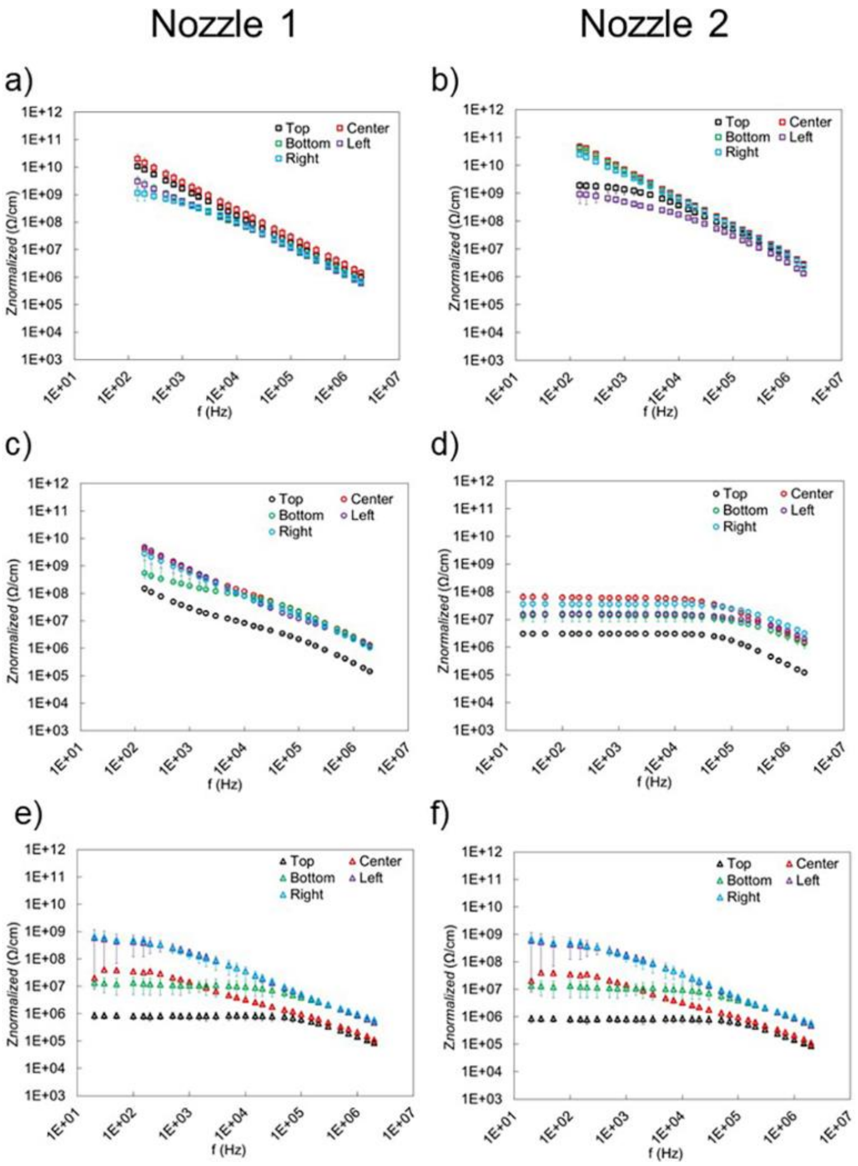

Fig. 6. Z$_{normalized}$ values obtained for nanocomposite films with different filler loadings at 10-cm target distance using nozzle 1 (diameter 1.2 mm) and nozzle 2 (diameter 1.5 mm). MWCNT loadings: (a, b) 0.5 wt%; (c, d) 1 wt%; (e, f) 2 wt%.

Fig. 7 and Fig. 8 show the normalized impedance values obtained for the MWCNT/epoxy nanocomposite films fabricated at nozzle-to-target distances of 15 and 20 cm, respectively. In the case of nanocomposite films deposited at a target distance of 15 cm (Fig. 7), the same considerations as for the 10-cm-sprayed films can be applied. Samples extracted from films with 0.5 wt% of MWCNTs (both nozzles) and with 1 wt% of MWCNTs (nozzle 1) are characterized by a typical capacitor behavior with high impedance values at low frequencies. On the other hand, samples from films fabricated at 1 wt% of MWCNTs with nozzle 2 (Fig. 7d) have lower impedance values that are constant up to 10 kHz and then decrease at higher frequencies. Further, the nanocomposite films deposited at these conditions are characterized by the highest level of homogeneity across the film surface, as indicated by the closer values of the EIS data for samples extracted at different locations. Such result is lost at higher loadings (2 wt%) of MWCNTs with both nozzles (Fig. 7e and 7f), likely due to a lower degree of dispersion of the filler in the resin. For such MWCNT concentrations of the nanocomposite, we found that the best results, in terms of uniformity of the electrical properties across the sprayed area, were obtained using nozzle 1 at a target distance of 20 cm (Fig. 8e).

The surface conductivity values of the nanocomposite films were calculated from Eq. (1) starting from the measured resistance values (R_p), considering different concentration of MWCNTs. In particular, the data collected from samples located in the center of the films, deposited at different target distances and for both nozzles, are reported in Fig. 9. For samples fabricated using nozzle 1, the conductivity curves are sufficiently close to each other to conclude that the effects of the target distance are negligible at all investigated concentrations (Fig. 9a, 9c, and 9e).

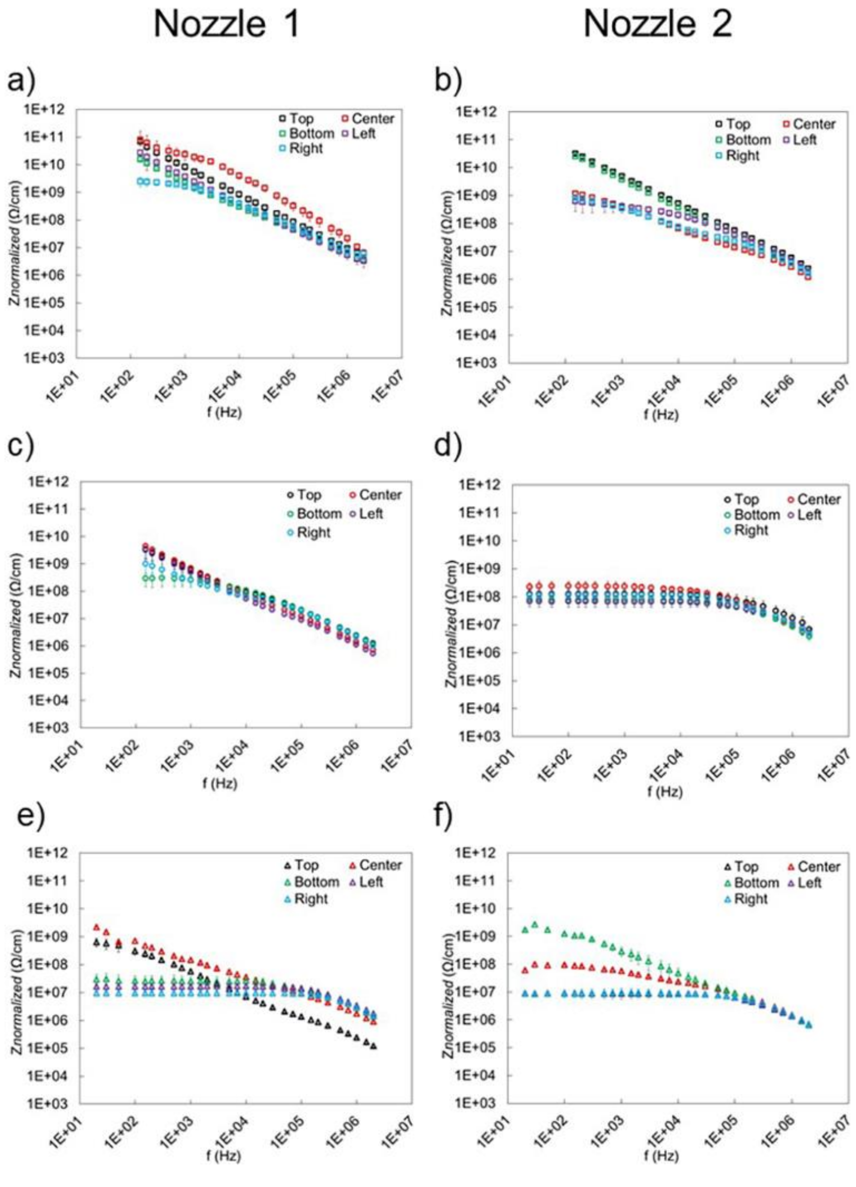

Fig. 7. Z*normalized* values obtained for nanocomposite films with different filler loadings at 15-cm target distance using nozzle 1 (diameter 1.2 mm) and nozzle 2 (diameter 1.5 mm). MWCNT loadings: (a, b) 0.5 wt%; (c, d) 1 wt%; (e, f) 2 wt%.

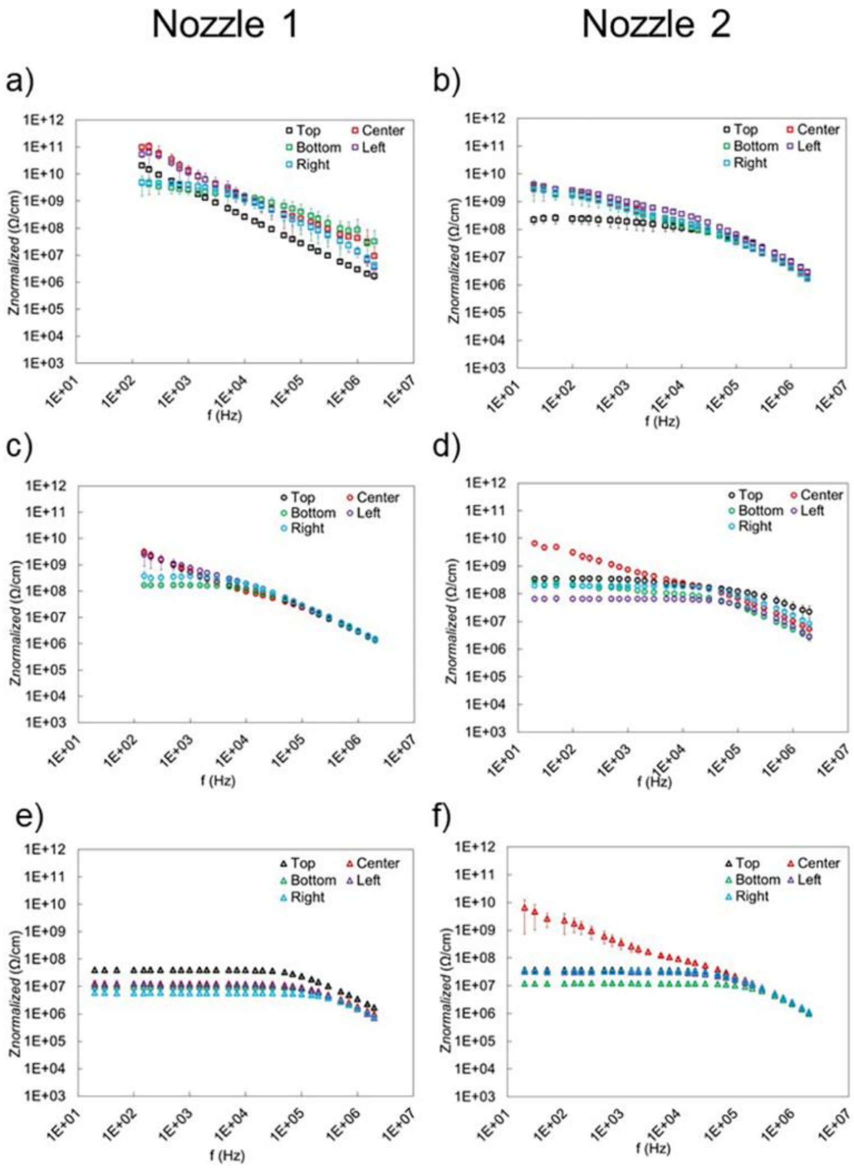

Fig. 8. $Z_{normalized}$ values obtained for nanocomposite films with different filler loadings at 20-cm target distance using nozzle 1 (diameter 1.2 mm) and nozzle 2 (diameter 1.5 mm). MWCNT loadings: (a, b) 0.5 wt%; (c, d) 1 wt%; (e, f) 2 wt%.

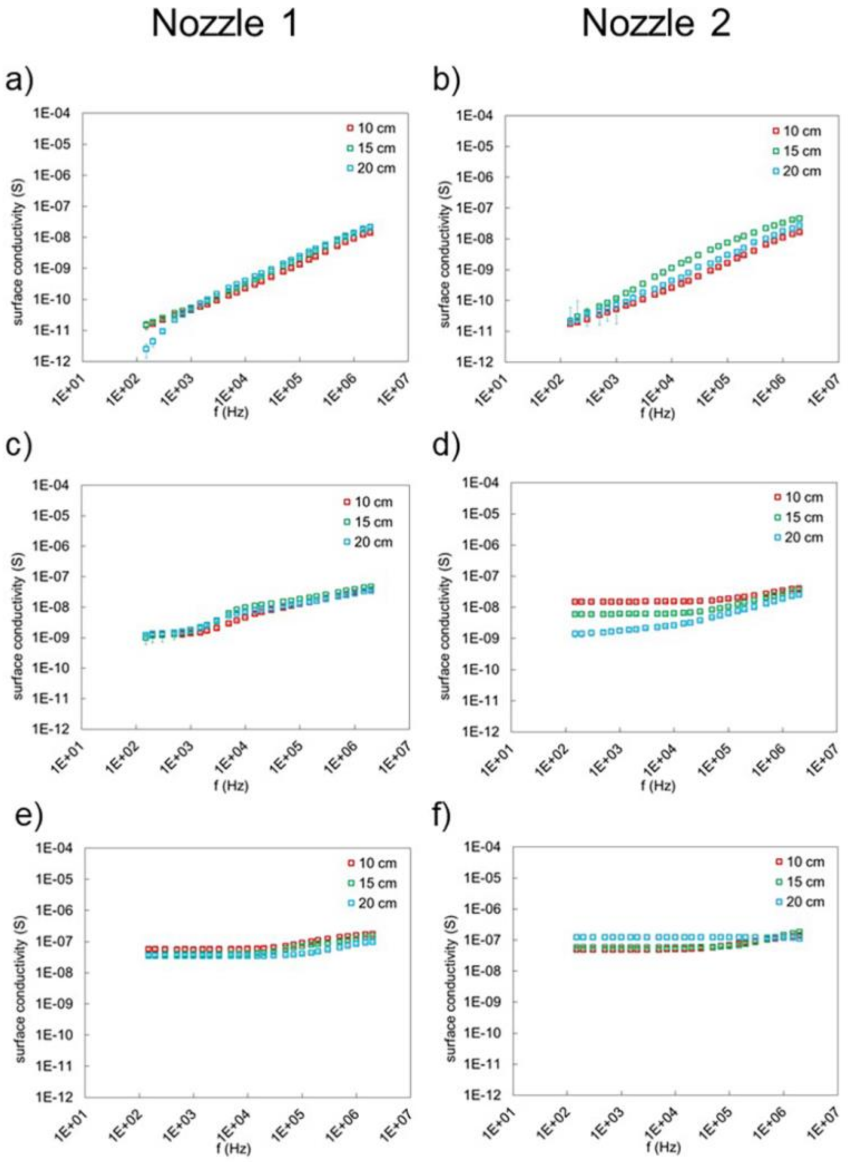

Fig. 9. Surface conductivity values as a function of frequency, at different target distance using nozzle 1 (diameter 1.2 mm) and nozzle 2 (diameter 1.5 mm) for filler contents (a, b) 0.5 wt%, (c, d) 1 wt%, and (e, f) 2 wt%.

At a fixed concentration of MWCNTs, the order of magnitude of the surface conductivity and the trend of the curves are similar for both nozzles. However, in the case of nozzle 2, a small separation among the curves referring to different target distances can be seen, especially at 1 wt% of MWCNTs. In this case, the surface conductivity of samples realized with target distance of 20 cm is smaller of about 1 order of magnitude at low frequencies (up to 10^5 Hz), than those obtained with the other target distances. At higher frequencies, the differences tend to disappear and the curves to overlap.

In general, the effect of different MWCNT concentrations is more evident on the surface conductivity values of the nanocomposites. With the increasing of the concentration of MWCNTs, the surface conductivity values increase. This is evident particularly at low frequencies, where the surface conductivity increases of 2 and 4 orders of magnitude, when the concentration is increased from 0.5 wt% to 1 wt% and to 2 wt%, respectively. At high end of the frequency range, the surface conductivity is approximately the same for concentrations of 0.5 w% and 1 wt% of MWCNTs, and it increases of only 1 order of magnitude when the filler concentration is 2 wt%.

The increase of surface conductivity at higher concentrations of MWCNTs can be attributed to the fact that the dielectric properties of the nanocomposite films are governed by the interfacial interactions between the nanoparticles and the polymer matrix. In nanocomposite films with higher filler loading, the overlap and the proximity of the carbon nanoparticles may occur more easily, leading to an increase of the electrical conductivity of the nanocomposite films. Regarding the trend, at 0.5 wt% of MWCNTs, the surface conductivity increases linearly as the frequency increases (Fig. 9a). When passing from 0.5 wt% to 2 wt% of MWCNTs, the slope of the curves decreases, until the nanocomposite films show almost constant conductivity values at all frequencies (Fig. 9e and 9f).

3.4 Conclusions

In this work, carbon nanocomposite films were fabricated by spray coating blends of MWCNTs dispersed in thermosetting epoxy resin onto a Mylar substrate. The nanocomposite films were fabricated using two different nozzle diameters, and the role of the process parameters and filler concentration on the thickness and electrical properties of the spray -coated films were investigated. We observed that larger covered areas were obtained using the nozzle with diameter of 1.5 mm at lower viscosity values of the nanocomposite blends (MWCNT concentration of 0.5 wt% and 1 wt%) and at lower nozzle-to-target distance of 10 cm. The surface electrical properties of the nano-reinforced epoxy films on Mylar were determined at different locations in order to investigate their uniform distribution. Results showed that a uniform surface conductivity can be achieved in nanocomposite films processed with the larger nozzle, at intermediate concentrations of MWCNT (1 wt%), and at target distance of 15 cm. In general, at higher concentrations of carbon nanotubes, the increase in blend viscosity, which is due to entanglement and surface interactions of the nanofillers, strongly limits the use of the spray coating process. This study gives insight into the manufacturing process of electrically-conductive nanocomposite films on Mylar substrate using spray coating, and highlights the most favorable conditions and bottlenecks at the level of process parameters and blend composition, namely the loading of MWCNTs. The analysis of the electrical properties of the processed films at different locations of the spray-covered area revealed what parameters are most relevant and need to be considered in the manufacturing process of these films, in order to optimize their properties for aerospace applications.

3.5 References

[1] Tang W, Santare MH, Advani SG. Melt processing and mechanical property characterization of multi-walled carbon nanotube/high density polyethylene (MWNT/HDPE) composite films. Carbon 2003;41:2779-85.

[2] Li J, Hu L, Wang L, Zhou Y, Grüner G, Marks TJ. Organic light-emitting diodes having carbon nanotube anodes. Nano letters 2006;6:2472-7.

[3] Clausi M, Santonicola MG, Schirone L, Laurenzi S. Analysis of ultraviolet exposure effects on the surface properties of epoxy/graphene nanocomposite films on Mylar substrate. Acta Astronautica 2017;134:307-13.

[4] Toto E, Santonicola MG, Mancini MC, Laurenzi S. Ultraviolet-sensing surfaces based on hybrid nanocomposites for radiation monitoring systems. 2017 IEEE International Workshop on Metrology for AeroSpace (MetroAeroSpace)2017. p. 369-73.

[5] Philip B, Abraham JK, Chandrasekhar A, Varadan VK. Carbon nanotube/PMMA composite thin films for gas-sensing applications. Smart Materials and Structures 2003;12:935.

[6] Zhang L, Ni QQ, Shiga A, Natsuki T, Fu Y. Preparation of polybenzimidazole/functionalized carbon nanotube nanocomposite films for use as protective coatings. Polymer Engineering & Science 2011;51:1525-32.

[7] Smith Jr JG, Connell JW, Watson KA, Danehy PM. Optical and thermo-optical properties of space durable polymer/carbon nanotube films: experimental results and empirical equations. Polymer 2005;46:2276-84.

[8] Laurenzi S, Zaccardi F, Semeraro M, Santonicola MG. Nanocomposite layers for spacecraft protection: from multiscale numerical model to experimental data. 18th European Conference on Composite Materials Athens, Greece2018.

[9] Clausi M, Laurenzi S, La Saponara V, Gabriella Santonicola M. Multifunctional sensors for UV and mechanical damage detection of aerospace structures. Proceedings of the International Astronautical Congress, IAC2016.

[10] Munakata N, Makita K, Bolsée D, Gillotay D, Horneck G. Spore dosimetry of solar UV radiation: applications to monitoring of daily irradiance and personal exposure. Advances in Space Research 2000;26:1995-2003.

[11] Zhang C-S, Ni Q-Q, Fu S-Y, Kurashiki K. Electromagnetic interference shielding effect of nanocomposites with carbon nanotube and shape memory polymer. Composites Science and Technology 2007;67:2973-80.

[12] Li Y, Chen C, Zhang S, Ni Y, Huang J. Electrical conductivity and electromagnetic interference shielding characteristics of multiwalled carbon nanotube filled polyacrylate composite films. Applied Surface Science 2008;254:5766-71.

[13] Yang Y, Gupta MC, Dudley KL. Towards cost-efficient EMI shielding materials using carbon nanostructure-based nanocomposites. Nanotechnology 2007;18:345701.

[14] Fernandez M, Shi H, Barnard AS. Geometrical features can predict electronic properties of graphene nanoflakes. Carbon 2016;103:142-50.

[15] Clausi M, Santonicola MG, Laurenzi S. Fabrication of carbon-based nanocomposite films by spin-coating process: An experimental and modeling

study of the film thickness. Composites Part A: Applied Science and Manufacturing 2016;88:86-97.

[16] Leopold C, Augustin T, Schwebler T, Lehmann J, Liebig WV, Fiedler B. Influence of carbon nanoparticle modification on the mechanical and electrical properties of epoxy in small volumes. Journal of Colloid and Interface Science 2017;506:620-32.

[17] Ansari S, Giannelis EP. Functionalized graphene sheet—Poly (vinylidene fluoride) conductive nanocomposites. Journal of Polymer Science Part B: Polymer Physics 2009;47:888-97.

[18] Eda G, Chhowalla M. Graphene-based composite thin films for electronics. Nano letters 2009;9:814-8.

[19] Peng H. Aligned carbon nanotube/polymer composite films with robust flexibility, high transparency, and excellent conductivity. Journal of the American Chemical Society 2008;130:42-3.

[20] Song YS, Youn JR. Influence of dispersion states of carbon nanotubes on physical properties of epoxy nanocomposites. Carbon 2005;43:1378-85.

[21] Xie X-L, Mai Y-W, Zhou X-P. Dispersion and alignment of carbon nanotubes in polymer matrix: a review. Materials Science and Engineering: R: Reports 2005;49:89-112.

[22] Norrman K, Ghanbari-Siahkali A, Larsen N. 6 Studies of spin-coated polymer films. Annual Reports Section" C"(Physical Chemistry) 2005;101:174-201.

[23] Krebs FC. Fabrication and processing of polymer solar cells: a review of printing and coating techniques. Solar energy materials and solar cells 2009;93:394-412.

[24] Bose S, Keller SS, Alstrøm TS, Boisen A, Almdal K. Process optimization of ultrasonic spray coating of polymer films. Langmuir 2013;29:6911-9.

[25] Ichiki M, Zhang L, Yang Z, Ikehara T, Maeda R. Thin film formation on non-planar surface with use of spray coating fabrication. Microsystem technologies 2004;10:360-3.

[26] Girotto C, Rand BP, Genoe J, Heremans P. Exploring spray coating as a deposition technique for the fabrication of solution-processed solar cells. Solar energy materials and solar cells 2009;93:454-8.

[27] Steirer KX, Reese MO, Rupert BL, Kopidakis N, Olson DC, Collins RT, et al. Ultrasonic spray deposition for production of organic solar cells. Solar Energy Materials and Solar Cells 2009;93:447-53.

[28] Vak D, van Embden J, Wong WW, Watkins S. Optically monitored spray coating system for the controlled deposition of the photoactive layer in organic solar cells. Applied Physics Letters 2015;106:7_1.

[29] Cadogan D, Lin J. Inflatable solar array technology. 37th Aerospace Sciences Meeting and Exhibit1999. p. 1075.

[30] Babuscia A, Corbin B, Knapp M, Jensen-Clem R, Van de Loo M, Seager S. Inflatable antenna for cubesats: Motivation for development and antenna design. Acta Astronautica 2013;91:322-32.

[31] Kerzhanovich VV, Cutts JA, Cooper HW, Hall JL, McDonald BA, Pauken MT, et al. Breakthrough in Mars balloon technology. Advances in Space Research 2004;33:1836-41.

[32] Engelhart D, Cooper R, Cowardin H, Maxwell J, Plis E, Ferguson D, et al. Space Weathering Experiments on Spacecraft Materials. 2017.

[33] Mazzinghi A, Sabbadini M, Freni A. Enhanced RF Behavior Multi-Layer Thermal Insulation. Scientific Reports 2018;8:91.

[34] Fesmire JE, Johnson WL. Cylindrical cryogenic calorimeter testing of six types of multilayer insulation systems. Cryogenics 2018;89:58-75.

[35] Woods AJ, Wenaas EP. Spacecraft discharge electromagnetic interference coupling models. Journal of Spacecraft and Rockets 1985;22:265-81.

[36] Catani J, Payan D. Electrostatic behaviour of materials in a charging space environment. Proceedings of the 2004 IEEE International Conference on Solid Dielectrics, 2004 ICSD 20042004. p. 917-27 Vol.2.

[37] Rawal S, Brantley J, Karabudak N. Development of carbon nanotube-based composite for spacecraft components. 6th International Conference on Recent Advances in Space Technologies (RAST)2013. p. 13-9.

[38] Steady-shear rheological properties of graphene-reinforced epoxy resin for manufacturing of aerospace composite films. AIP Conference Proceedings 2016;1736:020024.

[39] Sacramento RN, Yang Y, You Z, Waldmann A, Martins AL, Vaz ASL, et al. Deep bed and cake filtration of two-size particle suspension in porous media. Journal of Petroleum Science and Engineering 2015;126:201-10.

Chapter 4 – *Design of nanocomposite coatings by bar-coating process on CFRP structures for electrostatic charging mitigation for spacecraft*[3]

---

[3] Work in collaboration with Thales Alenia Space, Domain Exploration & Science – Engineering and Advanced Studies, Turin, Italy (Research period = May 2018-November 2018)

Abstract

The hostile space environment causes larger degradation effects on polymer-based material of the spacecrafts due to the combination of ultraviolet UV radiations, vacuum, atomic oxygen, plasma, electrons, protons as well as large temperature gradients, which can compromise the success of the entire mission.

In this work, we fabricated carbon/epoxy nanocomposite films on composite laminate substrate (CFRP) at different carbon nanoparticle loadings using bar-coating process. The effects of UV-C radiations and of aging tests on the electrical properties of carbon nanoparticles/epoxy films were investigated. The samples were irradiated at given UV-C dose, subjected to humidity and thermal cycles and electrical surface and volume conductivities were performed on untreated and irradiated/aged samples. Results show that the fabricated coatings respect NASA requirements to control and minimize electrostatic charging (ESC) by making spacecrafts surfaces uniformly conductive with a necessary surface resistivity $\rho_s<10^{+08}$ Ω/square.

4.1 Introduction

The ultraviolet radiation in the C band, with the combination of many space environmental factors such as large temperature gradients, plasma, vacuum, atomic oxygen, can compromise the integrity of many aerospace components [1-5] and the astronauts life during human exploration missions [6, 7]. In particular, the presence of space plasma can induce surfaces charging and so cause permanently physical damages and biasing of instruments to the on-board structural and electronic components respectively of the spacecraft [8-10].

Recently, it is devoting much attention to the possibility to exploit the excellent electrical properties of carbon nanoparticles [11-13] to fabricate nanocomposite materials with improved performance [14-21].

In this study we investigated the effects of UV-C radiations, high humidity level and thermal gradients on the electrical properties of carbon nanoparticles/epoxy resin coatings realized on carbon fiber/epoxy resin composite laminate (CFRP) substrate. In this study, we fabricated nanocomposite films on carbon fiber/ epoxy resin composite laminate substrate by bar-coating process. Different types of films were fabricated with different concentration and different carbon nanoparticles. Results show that the fabricated nanocomposite films have a sufficient electrical conductivity compliant with NASA requirements to mitigate ESC build-up [22].

4.2 Experimental

4.2.1 Materials

Graphene nanoplatelets (GnPs) with average thickness of 6-8 nm and lateral size of 25 µm were purchased from STREM Chemicals Inc. Tuball^{TM} single-walled carbon nanotubes (SWNTs) with diameter of 2 nm and length >1 µm were developed by OCSiAL and used to fabricate nanocomposite coatings. Henkel Loctite Hysol EA 9396 AERO Epoxy Adhesive was selected for the epoxy matrix.

TUBALL COMP_E epoxy Masterbatch containing 1 wt.% of single-walled carbon nanotubes (SWCNT) produced by OCSiAL, was used for the fabrication of thermoset nanocomposites.

Carbon fiber-reinforced polymer (CFRP) laminated panels were used as support for the nanocomposite coatings.

4.2.2 Fabrication of nanocomposite films on CFRP substrate

Carbon-based nanocomposite films were manufactured by bar-coating process on CFRP substrate. We prepared a homogeneous fluid mixture adding the carbon nanoparticles at a given weight percentage to the epoxy adhesive matrix. The epoxy adhesive was pre-heated for 30 min at 40°C to decrease its viscosity and then, after the addition of carbon nanoparticles, kept in ultrasonic bath for 120 min at 40°C. After sonication, the curing agent was gently added to the blend in the ratio of 100:30 by weight with respect to the epoxy base component. This procedure was repeated for each type of prepared nanocomposite blend: in particular we fabricated films with SWNTs at concentration of 0.9 wt.% (called for the analysis in this study C1) and films with hybrid concentration of 3wt.% of SWNTs and 1 wt.% of GnPs (called C2) respect to the epoxy adhesive matrix (called C). Following the same above-described procedure, we fabricated nanocomposite films based on masterbatch (called for the analysis B) with GnPs concentration at 2, 4, 6 and 8 wt.%.

For the bar-coating process, a fixed amount of nanocomposite mixture was dropped in different spots in orderly sequence on the top of CFRP substrate. The wire bar coater used was made out of stainless steel and the thickness of the film is controlled by the area of groove between the coils of wire. Nanocomposite films were cured in oven by varying the curing parameters with the nanoparticles content according to the thermo-analysis results. The final average thicknesses of the nanocomposite films after cure were measured using a digital calibre (accuracy 0.05μm). Thickness measurements were repeated in quintuplicate across a sample area and values were averaged. Film thicknesses were in the range 400-500 μm depending on nanoparticles concentration.

For electrical volume measurements, with all nanocomposite blends prepared, nanocomposite disc samples (and so without CFRP substrate), with a thickness in the range 400-500 μm, were fabricated by drop casting technique. The blends were drop-casted in a circular mold and then cured in oven following the same above-described procedure. At the end, after curing process, the nanocomposite discs obtained were lapped to obtain the wanted thicknesses and flatter surfaces in both sides of the disc to carried out more accurately electrical volume measurements.

4.2.3 Thermal characterization

Thermo-analysis will be performed to evaluate the effects of carbon nanofillers (CNT, GNP) on thermal properties of polymer matrix used. The addition of nanofillers to a polymer matrix greatly affects the polymerization phase in terms of kinetics and glass transition temperature [23]. These effects vary as a function of the filler wt.% in the polymer in a non-linear way, so this aspect must be studied. As the nanocomposite properties are strictly related to the curing process, thermo-analysis will help to set the process parameters.

Thermal analysis of the nanocomposite films was carried out using Differential Scanning Calorimeter (DSC) Q20 (TA Instruments, USA). Tests were performed in a nitrogen inert atmosphere with a heating rate of 10°C/min to acquire the enthalpies of reaction ΔH and 20°C/min for the glass transition temperature T_g. Tests were conducted in a range of temperature including the expected glass transition temperature of all nanocomposite materials fabricated, from 25 to 250 °C. The total area under the exothermal curves was used to calculate the enthalpies of reaction ΔH (J/g).

Thermogravimetric analysis (TGA, TA Instruments, USA) was conducted with a heating rate of 10°C/min under nitrogen inert atmosphere in the range of temperature from 25°C to 250°C, with the aim to investigate the thermal degradation behaviour of the nanocomposite samples to determine their thermal stability during heating.

The combined TGA-Fourier-transform infrared (FT-IR) spectra of fabricated nanocomposite samples were recorded by using the attenuated total reflectance (ATR) technique (Thermo Scientific, USA) in order to evaluate the nature of the reaction products from the thermogravimetric tests carried out on all nanocomposite samples. The spectrum was scanned 64 times at a resolution of 4 cm^{-1}.

4.2.4 Electrical measurements characterization

Dielectric measurements, in the frequency range from 1 MHz to 500 MHz, of the nanocomposite films were carried out using Dielectric Text fixture 16453A from Keysight. It employs the parallel plate method, in which the nanocomposite samples were placed between two identical electrodes to form a capacitor. It measures the capacitance created from the fixture and then it calculates the complex relative permittivity. The parameter, normalized respect to the thickness of the nanocomposite samples, that was measured on the machine, was $\varepsilon_r''(\omega)$ ($\varepsilon_r''(\omega)$ is the imaginary part of the complex relative permittivity). From the $\varepsilon_r''(\omega)$ measurements, we calculated the AC-volume electrical conductivity $\sigma_{V\text{-}AC}$ (S/m) of the samples, according to the following formula:

$$\sigma_{V\text{-}AC} = 2 \cdot \pi \cdot f \cdot \varepsilon_r'' \cdot \varepsilon_0 \tag{1}$$

where f is the testing frequency and ε_0 is the vacuum dielectric constant equal to 8.9 E^{-12} (F/m).

DC electrical measurements of the nanocomposite films on CFRP substrate were carried out using Resistance Meter with a concentric ring probe technique. The parameter that was measured on the device, was R_s (R_s is the electrical surface resistance of the film). From the R_s measurements we obtained the surface resistivity and conductivity of the samples, according to the following formulas [24]:

$$\rho_s = R_s \cdot [2\pi/(\ln (R_2/R_1))] \tag{2}$$

$$\sigma_s = 1/\rho_s \tag{3}$$

where R_2 is the inner radius of the outer ring electrode and R_1 is the outer radius of the center electrode.

A minimum of twenty measurements were carried for each nanocomposite sample.

The electrical properties of all films were measured before and after the UV-C exposure, humidity and thermal aging tests.

4.2.5 UV-C characterization

The nanocomposite samples were irradiated by with a UV lamp at fixed wavelength of 254 nm. The nanocomposite specimens were placed in the UV chamber and radiated for 2 hours to study the effects of radiations on nanocomposite films. The samples were irradiated with a radiative flux of 58 W/m^2.

The irradiance was measured and controlled by the photo-radiometers by Delta OHM with a combined probe for UV-C.

4.2.6 Humidity and thermal aging characterization

The aging tests are conducted with the aim to predict how the fabricated nanocomposite samples will age with time. It's well-known, in fact, that, in particular the exposure to higher temperature for extended periods of time can cause many physical and chemical property changes and degradations in polymer-based material.

In this work, the nanocomposite samples were placed in a climatic chamber and subjected to humidity and thermal cycles to study the effects of high humidity level and thermal gradients on overall electrical properties of nanocomposite samples.

For humidity aging test, the nanocomposite samples were aged for 4 hours at constant temperature of 23°C and 75% of humidity (RH).

For thermal aging test, the nanocomposite samples were aged following a thermal cycle inclusive of with 4 sub-cycles in temperature from T_0 = 23°C to T_f = 80 °C with stasis time in T_0 and T_f of 4 hours maintaining constant humidity level at 60%. The upper temperature limit, in thermal aging test, was selected to be consistent with the common temperature limit in which on-board electronic components work and due to the configuration of the available climatic testing chamber.

Nanocomposite films with and without CFRP substrate were tested in order to achieve the surface and volume electrical properties of the samples respectively.

4.3 Results and discussion

4.3.1 Thermal analysis

The DSC curves for B (masterbatch), B/GnPs 2-8wt.%, C (Epoxy - EA9396), C1 (C/SWCNTs 0.9 wt.%) and C2 (C/SWNTs 3 wt.% + GnPs 1 wt.%) nanocomposite samples are shown in fig. 1 (a,b). It’s evident that, after the addition of carbon nanoparticles, the cure reaction peaks increase. The enthalpies ΔH of reaction, the exothermal peak temperatures (T_{peak}) and the glass transition temperatures (T_g) values for all nanocomposite samples investigated are shown in Table 1. It can be observed that both ΔH and T_{peak} increase after the addition of nanoparticles not following a linear relationship with nanoparticles content especially for the class of nanocomposites made with B (Masterbatch). These results can be interpretated as a result of increased number of reactions that occur between polymeric chains and the nanoparticle surfaces [23, 25]. As expected, an appreciable increase of the T_g was also observed demonstrating that the introduction of nanoparticles in the polymer matrix leads to a reduction of the mobility of the polymeric chains induced by carbon nanoparticles, to an increasing of crosslinking density and so a more rigid material [26].

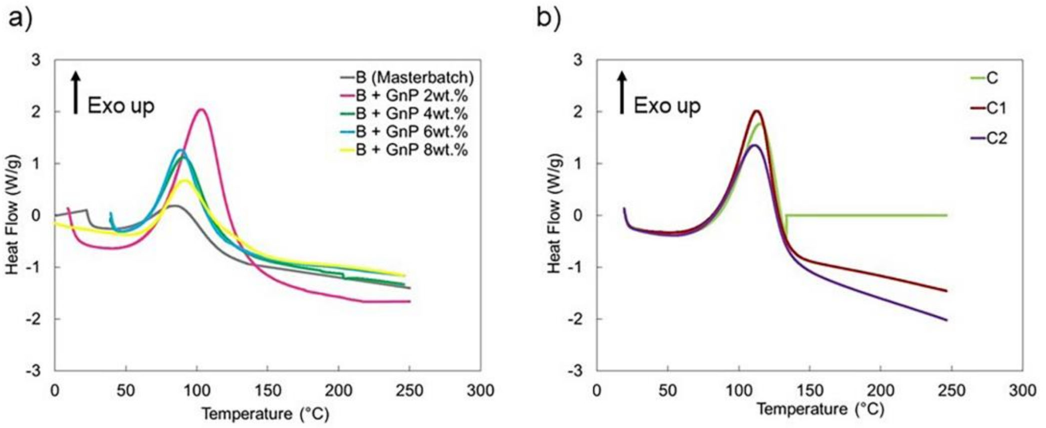

Fig. 1. DSC curves for B (Masterbatch) and different B/GnPs samples (a); (b) DSC curves for C (Epoxy-EA9396) and different C/carbon nanoparticles blends (namely C1 and C2).

Table 1. The enthalpies ΔH of reaction, the exothermal peak temperatures (T_{peak}) and the glass transition temperatures (T_g) of all nanocomposite sample fabricated.

Sample	**ΔH (J/g)**	**T_{peak}(°C)**	**T_g (°C)**
B (Masterbatch)	179.8	86.26	94.7
B + GnP 2wt.%	374.6	103.74	138.8
B + GnP 4wt.%	359.0	91.54	112.4
B + GnP 6wt.%	341.1	89.26	119.8
B + GnP 8wt.%	292.5	92.35	118.9
C (Epoxy)	543	108.23	115
C1	548	110.26	145
C2	570	109.26	158

Fig. 2 (a,b) shows the one-step degradation mass loss curves (TGA curves) of all nanocomposite samples fabricated. The addition of carbon nanoparticles decreases the thermal stability of the epoxy polymer matrix for all classes of nanocomposites fabricated: in fact, it can be detected that the onset temperatures of degradation shift to lower temperature after the introduction of nanoparticles. The presence, in fact, of carbon nanoparticles leads to an increasing of thermal conductivity and diffusivity of the resultant nanocomposite, and so a faster degradation of polymer [27]. In all cases, the residues at 250°C increase after the addition of nanoparticles, because of the higher content of carbon-based nanofillers in the composites. The first mass loss takes place below 100°C attributed to expulsion of the absorbed water as confirmed from TGA-FTIR spectra of the reaction products. The main mass loss occurs above 100°C (~3% for nanocomposites shown in fig. 2 (a) and ~1% for those shown in fig. 2 (b)) which can be assigned to the removal of carbon dioxide as confirmed from TGA-FTIR spectra.

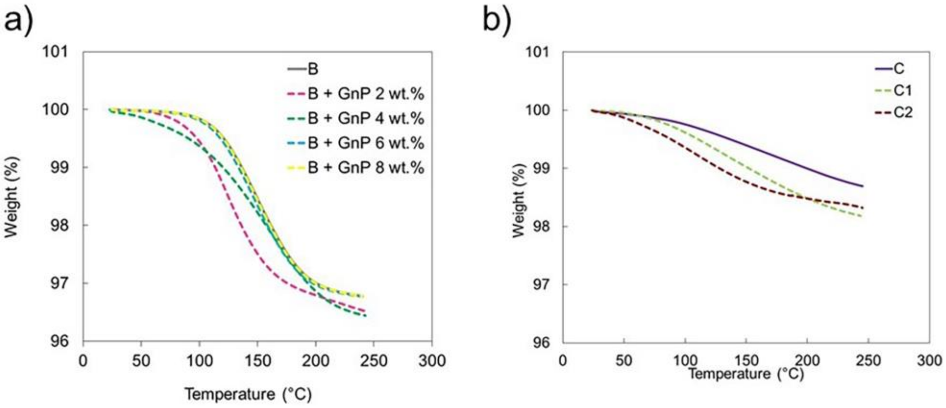

Fig. 2. Mass loss curves for B (Masterbatch) and different B/GnPs samples (a); (b) Mass loss curves for C (Epoxy-EA9396) and different C/carbon nanoparticles samples measured by TGA.

4.3.2 Electrical measurements analysis

Fig. 3 shows volume conductivity values obtained for hybrid B (masterbatch) nanocomposite samples reinforced with GnPs at concentration in the range 2-8 wt.%, as a function of working frequency up to 500 MHz. Electrical volume conductivity of all nanocomposite samples, tends to increase with increasing of working frequency and with graphene nanoplatelets content. In the case of nanocomposite sample reinforced with 8 wt.% of GnPs, in particular, it can be observed the highest values of volume conductivity at lower working frequency up to 30 MHz, then they tend to decrease respect to the case of nanocomposite sample with 6 wt.% of GnPs. We noted also that the volume conductivity does not change in order of magnitude after the introduction of graphene nanoparticles, remaining substantially costant and so, we decided to continue with the test

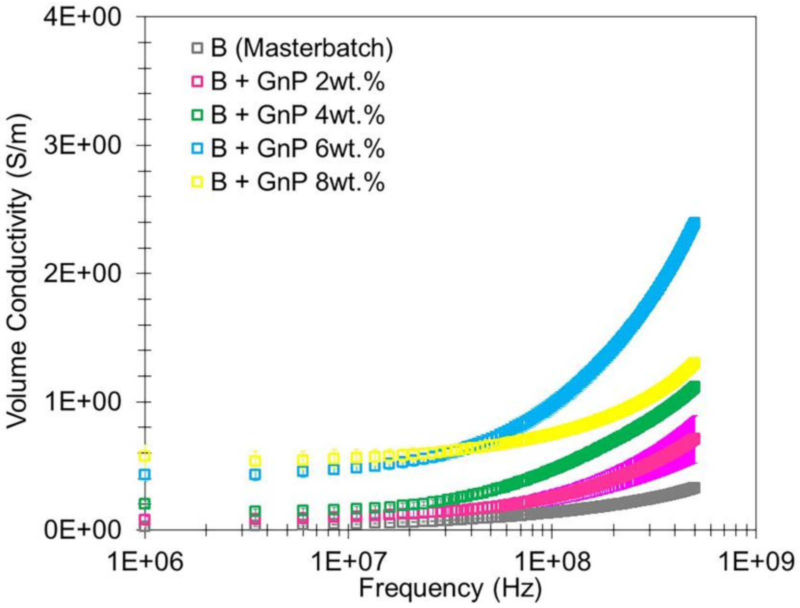

Fig. 3. Volume conductivity values of B (Masterbatch)/GnPs samples as a function of working frequency.

campaigns only with B (Masterbatch) and the other nanocomposite films made with epoxy matrix C (namely C1 and C2).

Fig. 4 shows volume conductivity values obtained for C (Epoxy), B (Masterbatch), C1 and C2 nanocomposite samples, before and after UV-C exposure, as a function of working frequency. Electrical volume conductivity of all nanocomposite samples, tends to increase with increasing of working frequency, in both cases of pre and post UV-C irradiation. Results show that, after UV- irradiation, the volume conductivity increases of one order of magnitude at higher frequency only for the more concentrated C2 nanocomposite sample. For the less concentrated nanocomposite samples (B and C1) are shown in figure 4 (b), any relevant changes are observed after UV-C irradiation.

Increasing of electrical conductance of the nanocomposite samples can be explained by considering that the UV-C radiations degrade the polymeric matrix, and so leaving uncovered a greater amount of conductive graphene nanoplatelets: that effect is more visible in the case of more concentrated C2 sample, at higher testing frequencies, in which the erosion of the resin results in a more conductive surface of the nanocomposites due to the exposure of a great amount of carbon nanoparticles.

The volume conductivity values obtained for C (Epoxy), B (Masterbatch), C1 and C2 nanocomposite samples, before and after humidity and thermal aging, as a function of working frequency, are shown in fig. 5 and fig. 6 respectively. For all nanocomposite samples, in both cases, the volume conductivity increases with the testing frequency both before and after aging tests. In particular, the volume conductivity values after humidity and thermal aging tends to increase especially at higher frequencies and for more concentrated nanocomposite sample C2. On the contrary, in the case of the less concentrated samples B and C1, the volume conductivity values after humidity and thermal aging tend to decrease at higher frequencies. Despite that, the volume conductivity values after both types of aging tests remain in the same order of magnitude than those not-aged.

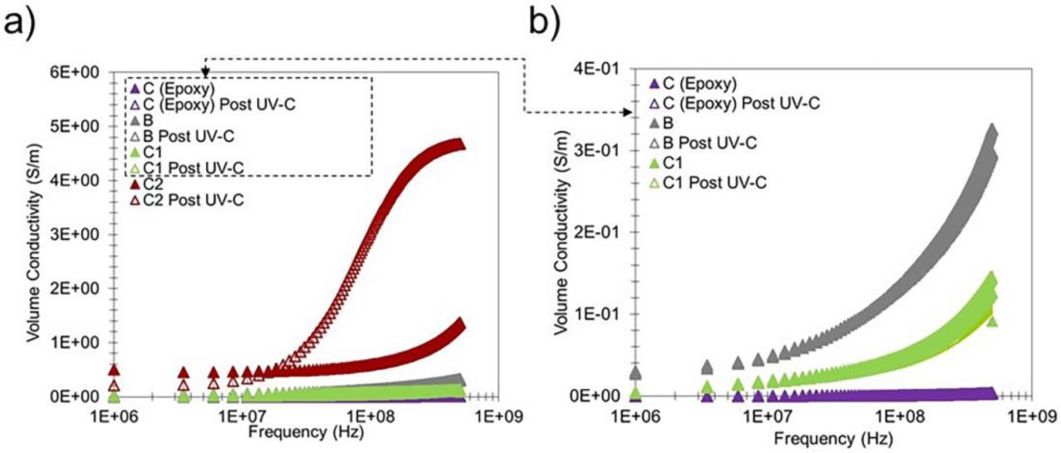

Fig. 4. Volume conductivity values of C, B, C1 and C2 nanocomposite samples before and after 2 h exposure to UV-C radiation as a function of working frequency (a); (b) zoom for C, B and C1 nanocomposite samples.

The above results from the volume conductivity analysis, in the case of humidity aging test, can be explained by considering the electrical resistance changing of SWNTs nanoparticles in presence of high concentration of water molecules. It’s well-known, in fact, that electrons-donating H_2O molecules are absorbed by carbon nanotubes, filling the hole carriers of p-type SWNTs and leading to a decreasing of conductivity until humidity level up to 65%. After the saturation point, in which all the water molecules compensate all the holes of semiconductor SWNTs, the conductivity starts to increase with increasing of humidity level, as happened in our case in which we aged nanocomposite samples with humidity at 75%, due to the fact that SWNTs become n-type semiconductor [28, 29]. We detected that the above-described behaviour is more evident in the case of more concentrated C2 sample.

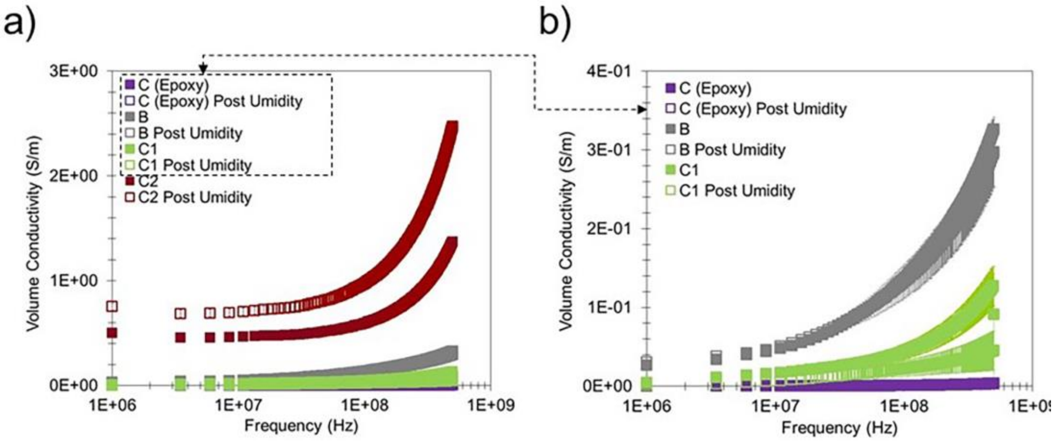

Fig. 5 Volume conductivity values of C, B, C1 and C2 nanocomposite samples before and after 4 hours of humidity cycle at 75% as a function of working frequency (a); (b) zoom for C, B and C1 nanocomposite samples.

The effects of thermal cycling, with the upper limit of temperature of 80°C, on nanocomposite samples demonstrate that the cyclical increase of temperature leads to a modest increasing of volume conductivity only for the more concentrated sample C2 and at higher frequencies. At lower frequencies the volume conductivity values didn't change because they remain within the standard deviation limits. In the case of less concentrated samples, as shown in fig. 6 (b), there aren't substantially any changes in the volume conductivity after thermal cycle, even if they tend to decrease after aging especially at higher frequencies.

Several sets of samples were tested for data reproducibility. The electrical response to UV-C irradiation, humidity and thermal cycles was found to be consistent over all the analyzed nanocomposite samples.

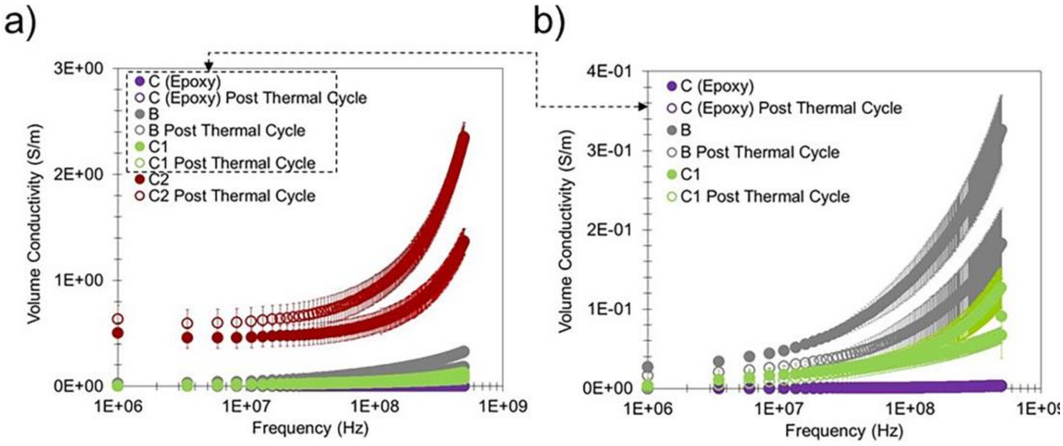

Fig. 6. Volume conductivity values of C, B, C1 and C2 nanocomposite samples before and after 4 thermal cycles from 23°C to 80°C as a function of working frequency (a); (b) zoom for C, B and C1 nanocomposite samples.

The surface electrical properties, determined in terms of surface resistivity and conductivity for all nanocomposite films fabricated on CFRP substrates, and electrical volume conductivity values obtained at f= 10 MHz, are summarized in Table 2. We detected, in particular that there are not relevant changes in the surface electrical properties of all nanocomposite films fabricated after aging tests because the obtained values of resistivity and conductivity vary within the standard deviation limits obtained before and after agings. For these reasons, all values of electrical properties reported in Table 2 refer to those obtained for non-aged nanocomposite films.

Results show that the obtained surface resistivity ρ_s values, for all nanocomposite films fabricated on CFRP, respect NASA requirements to control and minimize ESC charging by making spacecrafts surfaces uniformly conductive with a necessary surface resistivity $\rho_s<10^{+08}$ Ω/square [22].

Table 2. The surface resistivity ρ_s, conductivity σ_s and the volume conductivity $\sigma_{V\text{-}AC}$ of B, C1 and C2 nanocomposite samples.

Sample	**Carbon nanoparticles content**	ρ_s **(Ω/sq)**	σ_s **(S)**	$\sigma_{V\text{-}AC}$ **(S/m)** at f=10 MHz
B	1 wt. % of SWNT	$\leq 10^{+04}$	$\geq 10^{-04}$	$4.8 \cdot 10^{-02} \pm 1 \cdot 10^{-04}$
C1	0.9 wt. % of SWNT	$5 \cdot 10^{+06} \pm 1 \cdot 10^{+04}$	$2 \cdot 10^{-07} \pm 1 \cdot 10^{+09}$	$1.7 \cdot 10^{-02} \pm 1 \cdot 10^{-04}$
C2	3 wt.% of SWNT+1wt. % of GnP	$\leq 10^{+04}$	$\geq 10^{-04}$	0.47±0.05

The nanocomposite films of type C1 (Epoxy EA9396/0.9 of SWNT) were deposited, by bar coating process and with different geometrical configurations as shown in fig. 7 (a), on carbon epoxy composite laminate panel (CFRP), typically employed in satellite structures, to assess their use as potential innovative grounding system for spacecrafts. The choice of C1 is due for its lower absolute viscosity, due to the its lowest content of nanoparticles in the epoxy matrix, respect to the other two types of nanocomposite blends (namely B and C2) allowing for easier deposition process and in the same time providing good electrical properties. Fig.7 (b) shows the E-field radiated emission testing and measurements set-up of electronic component developed according to ECSS and NASA standards for EMC compatibility for a space vehicle.

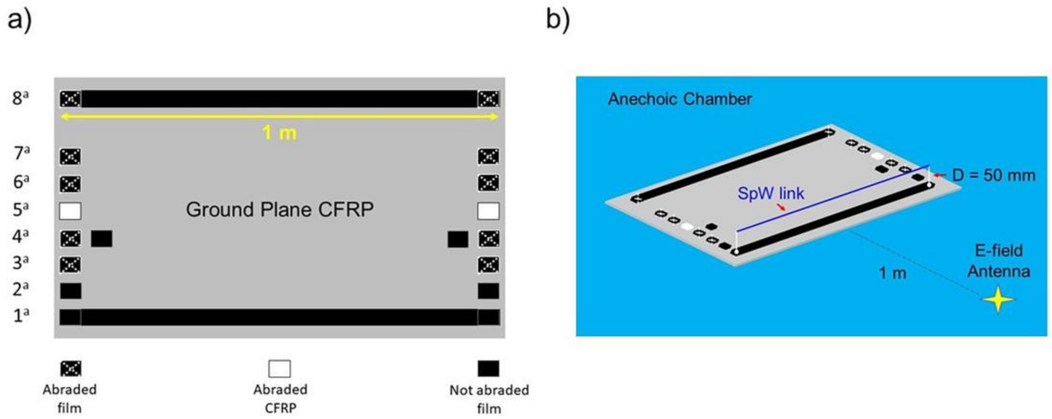

Fig. 7. (a) View of the eight configurations of C1-nanocomposite films deposited on ground plane CFRP; (b) Testing and measurements set-up of the E-field radiated emission of electronic component [30].

Preliminary DC electrical measurements on all nanocomposite film configurations realized on ground plane CFRP showed that all geometrical configurations of nanocomposite film fabricated on CFRP structure provide a low-DC electrical resistance paths to units placed on the CFRP structure. In particular, the fourth configuration (Fig.7 (a)), represent the most promising one with the lowest DC electrical resistance R_{DC} of 100 ± 5 Ω.

4.4 Conclusion

We investigated the properties of different carbon-based nanocomposite films, hybrid and not, deposited on carbon fiber/epoxy resin composite laminates

(CFRP) by bar-coating process. The effects of carbon nanoparticles on the cure reaction, glass transition temperature and thermal stability of the nanocomposite films fabricated were investigated with DSC and TGA. DSC analysis show that the introduction of nanoparticles in the polymer matrix leads to an increasing of enthalpies of reaction, cure peak temperature and of glass transition temperature. Moreover, the addition of carbon nanoparticles decreases the thermal stability of the epoxy polymer matrix for all classes of nanocomposites fabricated as shown in TGA results.

These films were exposed to UV-C radiation, humidity and thermal cycles and their electrical response, in terms of surface and volume conductivity, was investigated. Comparing the volume conductivity values obtained at the lower frequencies up to 100 MHz, we detected that only the nanocomposite film, with the highest concentration of nanoparticles (namely C2 sample), exhibits a modest increasing of the volume conductivity upon high level of humidity of 75% due to the fact that water molecules allow to the SWNTs to become n-type semiconductors. On the contrary, after UV-Irradiation and after thermal cycle with upper temperature limit of 80°C, any changes of volume conductivities were detected at those lower frequencies. For the others nanocomposite films, with a lower content of nanoparticles, we didn’t detect any changes in the volume conductivity after UV-C irradiation and after aging tests. At higher frequencies, no relevant changes in the volume conductive values, for all nanocomposite films, were detected after all tests except for the nanocomposite sample C2, which shows an electrical volume conductivity increased of one order of magnitude upon UV-C irradiation.

On the other hand, no significant changes in the surface resistivity and conductivity, are detected after all aging tests on all nanocomposite films fabricated.

Electrical results show that the fabricated coatings respect NASA requirements for thin material to control and minimize ESC charging for which the electrical resistivity $\rho_s < 10^{+08}$ Ω/square is needed.

4.5 References

[1] Hastings D, Garrett H. Spacecraft-environment interactions: Cambridge university press; 2004.

[2] Dever J, Banks B, de Groh K, Miller S. Degradation of spacecraft materials. Handbook of environmental degradation of materials 2005:465-501.

[3] Dever JA, Miller SK, Sechkar EA, Wittberg TN. Space environment exposure of polymer films on the materials international space station experiment: results from MISSE 1 and MISSE 2. High Performance Polymers 2008;20:371-87.

[4] Hastings D, Garrett H. Spacecraft-Environment Interactions. Cambridge: Cambridge University Press; 1996.

[5] Minton TK, Garton DJ. Dynamics of atomic-oxygen-induced polymer degradation in low earth orbit. Chemical dynamics in extreme environments 2001;11:420-89.

[6] Gallagher RP, Lee TK. Adverse effects of ultraviolet radiation: A brief review. Progress in Biophysics and Molecular Biology 2006;92:119-31.

[7] Barbatti M, Aquino AJ, Lischka H. The UV absorption of nucleobases: semi-classical ab initio spectra simulations. Physical Chemistry Chemical Physics 2010;12:4959-67.

[8] Fennell JF, Koons HC, Chen MW, Blake J. Internal charging: A preliminary environmental specification for satellites. IEEE transactions on plasma science 2000;28:2029-36.

[9] Takada T, Miyake H, Tanaka Y. Pulse acoustic technology for measurement of charge distribution in dielectric materials for spacecraft. IEEE transactions on plasma science 2006;34:2176-84.

[10] TRIBBLE A. The space environment and its impact on spacecraft design. 31st Aerospace Sciences Meeting1993. p. 491.

[11] Aliofkhazraei M, Ali N, Milne WI, Ozkan CS, Mitura S, Gervasoni JL. Graphene science handbook: electrical and optical properties: CRC press; 2016.

[12] Fernandez M, Shi H, Barnard AS. Geometrical features can predict electronic properties of graphene nanoflakes. Carbon 2016;103:142-50.

[13] Li J, Hu L, Wang L, Zhou Y, Grüner G, Marks TJ. Organic light-emitting diodes having carbon nanotube anodes. Nano letters 2006;6:2472-7.

[14] Ansari S, Giannelis EP. Functionalized graphene sheet—Poly (vinylidene fluoride) conductive nanocomposites. Journal of Polymer Science Part B: Polymer Physics 2009;47:888-97.

[15] Eda G, Chhowalla M. Graphene-based composite thin films for electronics. Nano Letters 2009;9:814-8.

[16] Böger L, Wichmann MH, Meyer LO, Schulte K. Load and health monitoring in glass fibre reinforced composites with an electrically conductive nanocomposite epoxy matrix. Composites Science and Technology 2008;68:1886-94.

[17] Kuilla T, Bhadra S, Yao D, Kim NH, Bose S, Lee JH. Recent advances in graphene based polymer composites. Progress in polymer science 2010;35:1350-75.

[18] Li Y, Chen C, Zhang S, Ni Y, Huang J. Electrical conductivity and electromagnetic interference shielding characteristics of multiwalled carbon nanotube filled polyacrylate composite films. Applied Surface Science 2008;254:5766-71.

[19] Tiwari S, Singh AK, Prakash R. Poly (3-hexylthiophene)(P3HT)/graphene nanocomposite material based organic field effect transistor with enhanced mobility. Journal of nanoscience and nanotechnology 2014;14:2823-8.

[20] Yang Y, Gupta MC, Dudley KL. Towards cost-efficient EMI shielding materials using carbon nanostructure-based nanocomposites. Nanotechnology 2007;18:345701.

[21] Smith Jr J, Connell J, Delozier D, Lillehei P, Watson K, Lin Y, et al. Space durable polymer/carbon nanotube films for electrostatic charge mitigation. Polymer 2004;45:825-36.

[22] NASA-HDBK-4002A. MITIGATING IN-SPACE CHARGING EFFECTS —A GUIDELINE. Approved: 03-03-2011.

[23] Cividanes LS, Simonetti EA, Moraes MB, Fernandes FW, Thim GP. Influence of carbon nanotubes on epoxy resin cure reaction using different techniques: a comprehensive review. Polymer Engineering & Science 2014;54:2461-9.

[24] Maryniak WA, Uehara T, Noras MA. Using a Concentric Ring Probe Technique.

[25] Yang K, Gu M, Jin Y. Cure behavior and thermal stability analysis of multiwalled carbon nanotube/epoxy resin nanocomposites. Journal of Applied Polymer Science 2008;110:2980-8.

[26] Pham JQ, Mitchell CA, Bahr JL, Tour JM, Krishanamoorti R, Green PF. Glass transition of polymer/single-walled carbon nanotube composite films. Journal of Polymer Science Part B: Polymer Physics 2003;41:3339-45.

[27] Ciecierska E, Boczkowska A, Kurzydlowski KJ, Rosca ID, Van Hoa S. The effect of carbon nanotubes on epoxy matrix nanocomposites. Journal of thermal analysis and calorimetry 2013;111:1019-24.

[28] Zahab A, Spina L, Poncharal P, Marliere C. Water-vapor effect on the electrical conductivity of a single-walled carbon nanotube mat. Physical Review B 2000;62:10000.

[29] Na PS, Kim H, So H-M, Kong K-J, Chang H, Ryu BH, et al. Investigation of the humidity effect on the electrical properties of single-walled carbon nanotube transistors. Applied Physics Letters 2005;87:093101.

[30] Cooperstein B, Johnson W, Thomas A. Development of a space vehicle electromagnetic interference/compatibility specification. Volume 1 Final engineering report, 28 Jun. 1968. 1968.

Chapter 5 - *Direct effects of UV irradiation on graphene-based nanocomposite films revealed by electrical resistance tomography*[4]

---

[4] Taken from the publication: ‘Direct effects of UV irradiation on graphene-based nanocomposite films revealed by electrical resistance tomography’, Composites Science and Technology, vol. 183, 1-8, 2019, (doi.org/10.1016/j.compshitech.2019.107823)’.

Abstract

The integration of surface sensing elements providing an *in situ* monitoring of the UV-induced degradation effects in composite materials and structures is crucial for their applications in hostile environments characterized by high levels of radiation, such as space. In this work, the electrical response of a novel UV-sensitive nanocomposite film was investigated using electrical resistance tomography (ERT). The conductivity changes measured at the irradiated surfaces were compared with results from morphology analysis by scanning electron microscopy (SEM) and surface analytical techniques, such as Raman microscopy. Highly conductive and UV-sensitive nanocomposite coatings were prepared by embedding the graphene and deoxyribonucleic acid (DNA) component in a poly(3,4-ethylene dioxythiophene):poly(styrene sulfonate) (PEDOT:PSS) matrix. The coatings were deposited onto carbon-reinforced laminated structures fabricated by resin transfer molding process using an aerospace-grade epoxy resin. Two different irradiation conditions were tested by exposing the nanocomposite surfaces to UV-C irradiances of 2.6 and 4.0 mW/cm^2. Results show that the ERT technique has great potential for the *in situ* health monitoring of carbon-based materials and structures for aerospace applications, which are subject to degradation by UV-C radiation: it allows mapping of the conductivity changes occurring at the surface of the graphene/DNA/PEDOT:PSS coatings during irradiation.

5.1 Introduction

Carbon fiber-reinforced polymer composites are widely used in aerospace structures for their excellent strength-to-weight ratio and stiffness-to-weight ratio, improved corrosion resistance and property tailorability for specific applications [1, 2]. However, it is well known that hostile space conditions cause degrading effects on polymer composite laminates [3-5]. UV radiations, vacuum, atomic oxygen and large temperature gradients all lead to the degradation of polymer-based materials [4-8], affecting the structural integrity of spacecraft components, and reducing the life cycle of the structure. To solve these problems, researchers are investigating many solutions, one being the fabrication of sensor elements to integrate into the composite laminates, thus creating health monitoring systems for radiation-induced damage to aerospace structures [9-11]. In this contest, the use of electrical measurements for strain sensing and damage identification was recently proposed [12-19]. In particular, several groups are studying electrical conductivity-based health monitoring methods, in which the damaged areas in composite laminates are identified by monitoring the changes of electrical conductivity in such areas. To this end, electrical impedance tomography (EIT), based on alternating currents (AC), and electrical resistance tomography (ERT), based on direct currents (DC), are receiving great attention because they are low-cost and non-invasive techniques that allow to obtain electrical conductivity maps of the parts under exam. In their study, Schueler and colleagues demonstrated that, using EIT mapping, damaged areas in carbon fiber-reinforced composite materials correspond to areas with lower electrical conductivity [20]. Baltopoulos et al. investigated the effects of different types of damage (drilled hole, local indentation) on the electrical properties of composites reinforced with carbon fibers and nanotubes, using ERT [21, 22]. In both works, the authors were able to detect the presence of damage in terms of loss of conductivity in the same area where the damage occurred. Other studies investigated the use of electrically conductive nanocomposites and the possibility of identifying damage to the matrix by electrical measurements [23-25]. For example, by using carbon black filler and the EIT technique, Tallman et al. were able to locate the matrix damage in glass fiber/epoxy laminates [26].

Recently, the development of nanocomposite films is receiving great attention, where the films are applied on composite structures for damage monitoring purposes. Loh et al. fabricated nanocomposite films filled with carbon nanotubes as sensing skins on different type of substrates [18]. They detected strain during applied load and spatial impact damage on the nanocomposite films by electrical impedance tomography. In another work, Loyola et al. studied the spatial distribution of conductivity changes in nanocomposite films that were spray-deposited on glass fiber-reinforced polymer (GFRP) composites upon damage from a drilling operation and from low-velocity impact [12]. Results showed that indeed, in the electrical resistance tomography maps, the damaged areas possess a lower conductivity. These trends were confirmed by Lestari et al. for uniaxial tensile loadings in glass fiber-reinforced polymer composites coated by nanocomposite films [27].

In this proof-of-concept work, the use of ERT to identify the damaging effects of UV-C radiation was investigated on nanocomposite coatings made of graphene nanoplatelets (GNP) functionalized with deoxyribonucleic acid (DNA) and embedded in a poly(3,4-ethylene dioxythiophene):poly(styrene sulfonate) (PEDOT:PSS) matrix. The DNA-functionalized GNPs were chosen based on previous work from our group showing their sensitivity to UV radiation [9, 28], whereas the PEDOT:PSS matrix was selected to enhance the electrical conductivity of the overall nanocomposite [10]. The UV-sensitive coatings were applied to the surface of carbon fiber/epoxy laminates, which are composite structures that are typically used in the aeronautical and space fields. To our knowledge, this is the first report of the application of the ERT technique to the detection of surface conductivity changes induced by UV exposure. This technique in combination with the UV-sensitive coatings containing DNA-functionalized graphene can provide a health monitoring method for composite materials and structures that are exposed to damaging levels of UV radiation. A 16-electrode scheme was applied along the edges of the nanocomposite sensor coatings, and maps of conductivity changes were reconstructed after UV-C irradiation with two different intensities (2.6 and 4.0 mW/cm^2) for 24 h. The information from the ERT analysis is discussed and related to results from complementary techniques, such as scanning electron microscopy and Raman spectroscopy, which have previously proven to be a valuable tool for the characterization of carbon/DNA interfaces [29, 30].

5.2 Experimental

5.2.1 Materials

Graphene nanoplatelets grade AO-4 with average thickness 60 nm and lateral size in the range 3-7 μm were purchased from Graphene Supermarket (Graphene

Laboratories, USA). Double-stranded DNA and poly(3,4-ethylenedioxythiophene)-poly(styrenesulfonate) (PEDOT:PSS) in the form of dry re-dispersible pellets were purchased from Sigma-Aldrich and used as received. DNA solutions and GNP/DNA dispersions were prepared in Milli-Q deionized water (resistivity 18.2 MΩ·cm) from a Direct-Q3 UV water purification system (Millipore, France). Carbon fiber-reinforced polymer (CFRP) laminated plates were fabricated by resin transfer molding (RTM) as support for the nanocomposite sensors. The resin used was HexFlow RTM6, a space-grade mono-component epoxy resin purchased from Hexcel (Duxford, UK). The fiber reinforcement was a 1K-T300 carbon plain weave with areal mass density of 120 g/m^2. Silver paint (Ted Pella, USA) and silver epoxy conductive adhesive (Type 8331, MG Chemicals, Canada) were used to fabricate the electrodes on the top surface of the nanocomposite sensor.

5.2.2 Fabrication methods

Nanocomposite coatings containing GNP/DNA nanomaterial dispersed in the PEDOT:PSS matrix were prepared by sonication in aqueous solution followed by deposition on the CFRP laminated plates and drying at 50 °C. First, aqueous dispersions of GNP and double-stranded DNA (20 mg/ml) were prepared in ultrapure water and sonicated for 2 h in a cold bath to prevent DNA degradation. For an optimal dispersion of graphene in the DNA solution, the two components were mixed at a 1:1 weight ratio, following previously established results [30, 31]. Next, PEDOT:PSS pellets were added to the GNP/DNA solution, while stirring, at a concentration of 0.7% by weight. The dispersion (4 mL) was deposited on the

CFRP supports (size 40 mm x 40 mm) and dried in oven at 50 °C overnight. Prior to the deposition, the carbon fiber/epoxy supports were coated by a thin layer of PEDOT:PSS (from an aqueous solution at 0.7% by weight) using the same drying conditions. The interposed PEDOT:PSS layer allowed for enhanced adhesion between the support and the GNP/DNA/PEDOT:PSS coating. Nanocomposite coatings with a uniform thickness of 0.03 mm and reference conductivities of 0.08 - 0.09 S/mm were obtained at these conditions.

5.2.3 UV-C irradiation tests

Nanocomposite coatings were irradiated with monochromatic UV light at 254 nm from a 30 W low-pressure mercury lamp. Samples were placed in a closed irradiation chamber with the UV source fixed in the top lid. Only the central part (20 mm × 20 mm) of the sample was exposed to UV-C radiation for 24 h, while the edges of the sample (where the electrodes would be fixed) were protected using aluminum foil. In prior work, an irradiation period of 17 h was sufficient to observe changes of the electrical conductivity of GNP/DNA films (applied to a different fiber-reinforced polymer substrate) [9]. Here, an irradiation time of 24 h was used for testing convenience. Samples were placed at two different distances from the lamp in order to vary the radiation intensity on the surface. For the ERT investigation, irradiances of 2.6 and 4.0 mW/cm^2 were used, corresponding to sample-to-source distances of 93 mm and 55 mm, and to radiation doses of 225 and 346 J/cm^2 in 24 h, respectively. The UV-C irradiance levels were selected to be consistent with those in the Low Earth Orbit (LEO) environment, in which the International Space Station and most communication satellites are located. Here, approximately 0.8% of the solar irradiance value is in the UV-C region, in particular 1.30 mW/cm^2 at the wavelength of 254 nm [32]. In this work, higher levels of irradiances between two and four times those of the LEO environment were used in order to achieve radiation doses in the range 200-400 J/cm^2 within 24 h of exposure and due to the configuration of the available testing chamber.

Additional irradiation tests as a function of the UV-C dose were performed under a 8 W low-pressure lamp set at 254 nm (3UV-38, UVP LLC, USA) in a closed chamber. The irradiances were measured using a HD 2302.0 radiometer (Delta Ohm, Italy) fitted with a LP 471 UVC probe (spectral range 200–280 nm). Samples were exposed to an irradiance of 0.63 mW/cm^2 and measured daily for up to 7 days, corresponding to a maximum dose of 380 J/cm^2.

5.2.4 ERT system, acquisition and post-processing

Electrical resistance tomography (ERT) is a technique that allows to obtain a distribution of electrical resistance values within the domain of interest [33]. The electrical resistance distribution in that domain is obtained by injecting a current into electrodes that are positioned around the boundary of the domain of interest on the sample surface. Then, the resulting voltages between two electrodes are measured along this boundary, as the output, which will be used in the image processing algorithm. The algorithm will eventually compute the conductivity map of the domain, in a two parts sequence: the solution of a forward problem, and the solution of an inverse problem, as discussed below.

The experimental ERT setup for the acquisition of differential voltage data from up to 16 electrodes was composed by the data acquisition system (DAQ) from

National Instruments (NI-6216), connected to a 16-electrodes voltage buffer circuit used with the aim of reducing current leak from the voltage sensing electrodes [34]. Direct currents were injected using an Agilent DC current supply (Agilent E3610A), while an op-amp power supply was used to reduce the noise in the measurements. A digital multimeter (Tektronix DMM916) ensured that there was accuracy in the injection current amplitude during the tests. Differential voltage data were acquired using the LabVIEW software package (National Instruments, Inc.) at various injection currents, with the baselines consisting of the untreated coatings, i.e. before exposure to UV-C. Samples for the ERT investigations were of size 40 mm × 40 mm; 16 electrodes were fixed along the edge of the nanocomposite sensor surface, leaving a central area of 20 mm × 20 mm free for irradiation (Fig. 1a). Four equidistant electrodes were applied to each side and in orderly sequence. To ensure a strong sensor-electrode contact, the electrodes were created with a layer of silver paint onto which the ends of electrical wires were placed and then fixed using silver epoxy conductive adhesive (cure in air at ambient conditions for 24 h). The size of the electrodes was mainly dictated by the challenge of bonding electrodes on the nanocomposite film. In the current study, the electrodes were manufactured at a nominal distance of 1-2 mm among each other. The electrode size could be construed as large with respect to the domain of interest. However, Gisser et al. [35] and Hua et al. [36] used large electrodes in their study, achieving a more uniform internal current distribution, and leading to improvements in image reconstructions.

From the measured differential voltage data, ERT conductivity maps, describing the changes in the surface electrical conductivity of the nanocomposite samples after irradiation, were reconstructed by finite element method (FEM) approach using the open-source Electrical Impedance and Diffuse Optical Reconstruction Software (EIDORS) suite [37, 38], based on the commercial software MATLAB (Mathworks). The reconstruction problem was addressed by discretizing the sample in a finite number of elements, defining the dimension of the model, the position, the dimensions and the geometry of the electrodes on the sample surface, and describing all current injection patterns used (forward problem). Next, the reconstruction of the conductivity distribution on the sample surfaces was performed (inverse problem) [38, 39]. The relationship between the conductivity distribution σ and a vector of measured voltages v for a specific current injection and initial conductivity estimate σ_0 is approximated by a vector of analytically predicted boundary voltages $F(\sigma)$ expressed by the Taylor series (Eq. 2):

$$v = F(\sigma) \tag{1}$$

$$F(\sigma) = F(\sigma_0) + \sum_{n=1}^{\infty} \frac{1}{n!} \frac{\partial^n F(\sigma)}{\partial \sigma^n}\bigg|_{\sigma_0} (\sigma - \sigma_0)^n \tag{2}$$

Recovering σ from experimental measurements v is an ill-posed inverse problem, which depends on several factors including the exact shape of the region of interest and electrode positions, variations in contact impedance, and estimation of the internal conductivity. Solving the non-linear inverse problem requires regularization techniques. In this work, the Tikhonov regularization was implemented [39], with the electrical conductivity changes of the sensor coatings ($\Delta\sigma$) related to the measured difference voltage data ($\Delta V_{\text{resultant}}$) as:

$$\Delta\sigma = (J^T J + aL^T L)^{-1} J^T \Delta V_{\text{resultant}} \tag{3}$$

Here, J is the Jacobian matrix for complex impedance, and a is the regularization hyperparameter, which governs the amount of smoothing in the reconstruction process in conjunction with a discrete Laplacian filter L. In order to prevent over-smoothing and for an objective selection of the hyperparameter [40], the fixed noise figure (NF) method proposed by Adler and Guardo [41] was implemented. In this method, the hyperparameter α is chosen so that to the signal-to-noise ratio (SNR) for the voltage measurements (SNR_v) equals that of the reconstructed conductivity distribution (SNR_σ), which corresponds to a NF value of 1.

$$NF(\alpha) = \frac{SNR_v}{SNR_\sigma} \tag{4}$$

Several authors have selected the fixed NF method when implementing the ERT analysis in structural health monitoring applications using composite materials [12, 14, 27, 42]. In the reconstructed conductivity maps, the conductivity changes ($\Delta\sigma$) were normalized with respect to the maximum variation of the electrical conductivity occurring at the surface ($\Delta\sigma_{max}$) according to the following formula:

$$\Delta\sigma_{normalized} = \Delta\sigma/\Delta\sigma_{max} = \left(J^T J + \alpha L^T L\right)^{-1} J^T (\Delta V_{\text{resultant}}/\Delta V_{\text{resultant}_{max}}) \tag{5}$$

5.2.5 Characterization methods

The morphology of the nanocomposite coatings was investigated by scanning electron microscopy (SEM) using a Tescan VEGA II LSH instrument with accelerating voltage of 10 kV and magnifications from 1000 X to 3000 X. The electrical resistance was determined by electrical impedance spectroscopy (EIS) using a Gamry Reference 600 potentiostat in a custom-made cell with two copper strips as electrodes [10]. Resistance values were converted to conductivity values using the following equation [42]:

$$\sigma = \frac{1}{\rho} = \left(R\,\frac{A}{l}\right)^{-1} \tag{6}$$

where σ is the electrical conductivity, ρ is the resistivity, R is the measured electrical resistance, l is the distance between the copper electrodes, and A is the cross-sectional area of the sensor coating. Raman experiments were performed with a Horiba XploRA PLUS Raman microscope with 532 nm laser excitation. The Raman signal was collected through a 10 X objective in the range 200 - 3000 cm^{-1} with accumulation time of 5 s per spectrum. Areas of the substrates up to 7 µm × 7 µm were scanned with diffraction grating of 600 g/mm. All spectra were obtained with a 10% filter to avoid sample heating and damaging.

5.3 Results and discussion

5.3.1. ERT sensitivity analysis

In the first part of the study, a sensitivity analysis on values and patterns of the injection currents was carried out, with the aim of identifying a combination which would be reasonably sensitive to surface defects in the as-manufactured samples, prior to UV-C irradiation. Direct current values of 10 mA, 20 mA, 30 mA, 40 mA, 50 mA, 80 mA, 100 mA and 150 mA were used. Previously, a 200 mA current was found to cause electrolysis damage to the electrodes [34], and therefore the selected currents for this study were lower. For each injection, 256 differential voltage data measurements were recorded at each load step ($m^2 = 256$, in which $m = 16$ is the number of electrodes). The number of independent measurements depends on the type of injection. Shi et al. have advocated the so-called pseudo-polar pattern as the best drive pattern for brain electrical impedance tomography: in this pattern, the driving current flows into one electrode and out of another electrode located almost at 180 degrees with respect to the injection electrode [43]. On the other hand, Kolehmainen et al. have found that the so-called adjacent injection pattern is more robust to modeling errors of contact impedance, electrode size, boundary in typical EIT biomedical problems [44]. Because of the nature of the samples in this paper and the absence of earlier ERT studies on such samples, a reasonably broad set of injection patterns was investigated. Fig. 1 shows the five different voltage measurement patterns that were investigated in combination with each injection current.

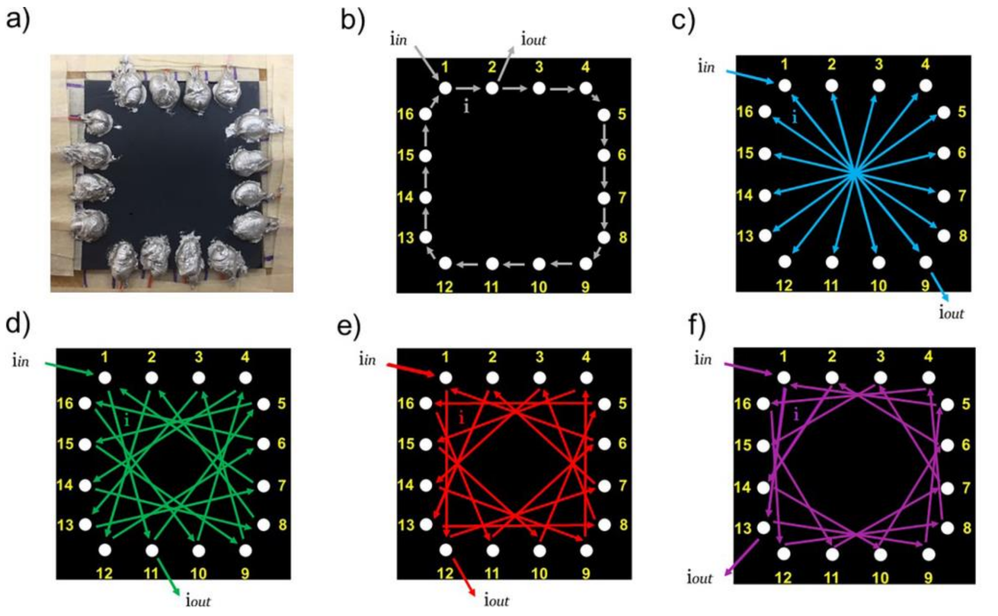

Fig. 1. (a) GNP/DNA/PEDOT:PSS nanocomposite film on CFRP laminated substrate (size 40 mm × 40 mm) with sixteen electrode elements fixed by conductive silver epoxy; schemes of applied current injection patterns: (b) adjacent pattern, (c) opposite pattern, (d) 1-11 pattern, (e) 1-12 pattern, and (f) 1-13 pattern.

In the adjacent pattern (Fig. 1b), the current was injected through two neighboring electrodes, while the differential voltage data were recorded from all other electrodes. The sequence rotates for a new measurement until the pattern returns to the original position. In the opposite pattern (Fig. 1c), the current was injected through the first and the ninth electrodes, and the procedure was repeated clockwise. In the 1-11 pattern (Fig. 1d), the current was injected through the first and eleventh electrodes. In the 1-12 pattern (Fig. 1e) and in the 1-13 pattern (Fig. 1f), the current was injected through the first and twelfth electrodes, and from the first and the thirteenth electrodes, respectively. The same procedure used for the adjacent and opposite patterns was applied to the 1-11, 1-12 and 1-13 patterns. For each injection, measurements at a specific current value and current pattern were repeated several times. The results of the preliminary ERT sensitivity analysis for the nanocomposite coatings exposed to UV-C irradiances of 2.6 and 4.0 mW/cm^2 are reported in Fig. 2 and Fig. 3, respectively. The changes of voltage measurements due to UV-C irradiation, as recorded by the sixteen electrodes, are shown for different patterns and injection currents (range 10 – 50 mA). In both cases of UV-C exposure, the opposite scheme resulted in the current pattern exhibiting the highest sensitivity to the changes induced by irradiation at all injection currents. For this reason, the opposite scheme was selected for the subsequent reconstruction of the conductivity change maps by the EIDORS toolbox. The optimal electric field density that is required for the reconstruction of meaningful conductivity change maps describing the changes of GNP/DNA/PEDOT:PSS surfaces under UV irradiation depends on the correct combination of injection pattern and current intensity. Results show that increasing the density of the injection pattern, for the same injection current, the absolute difference between the voltage measurements increases. From the optimization analysis of the ERT injection currents, in order to localize surface defects on the nanocomposite coatings under investigation, the best results were found using lower injection currents, up to 50 mA.

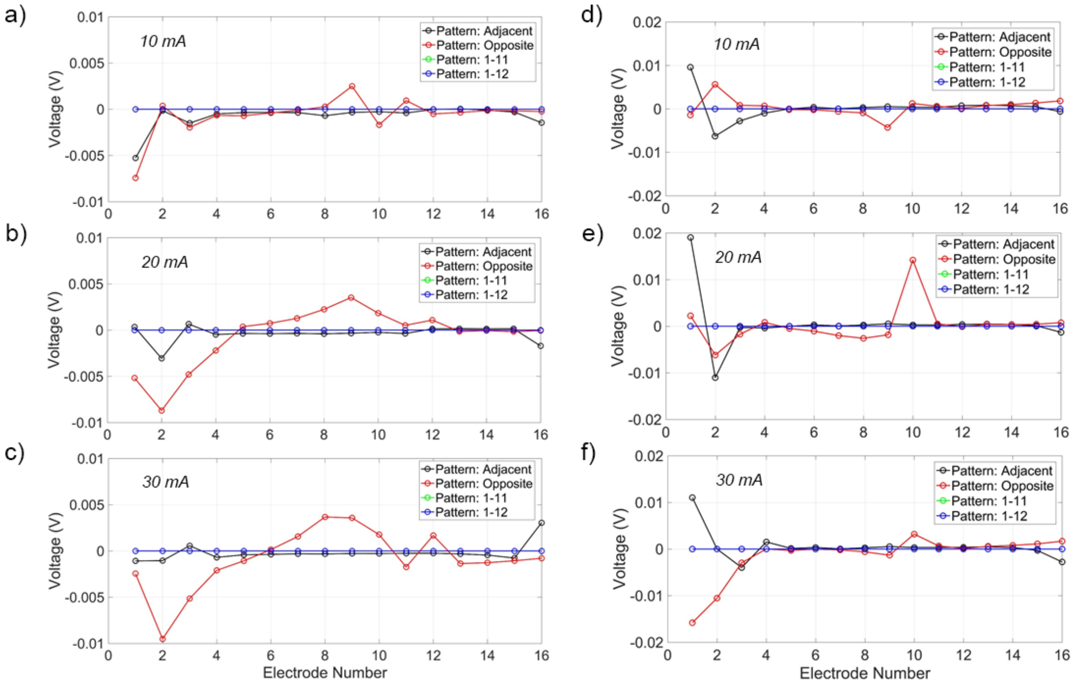

Fig. 2. Voltage changes of GNP/DNA/PEDOT:PSS surfaces due to UV-C irradiation recorded using the sixteen-electrode configuration with different injection patterns and currents of 10, 20 and 30 mA. UV-C exposure: (a, b, c) 2.6 mW/cm^2 for 24 h; (d, e, f) 4.0 mW/cm^2 for 24 h.

5.3.2. ERT mapping of UV damage on nanocomposite surface

The ERT analysis was applied to investigate the effects of UV-C irradiation on the surface electrical conductivity of GNP/DNA/PEDOT:PSS surfaces. The normalized conductivity change maps reconstructed from the ERT data for the surfaces exposed to UV-C irradiance of 2.6 mW/cm^2 for 24 h are presented in Fig. 4. Different injection currents in the range 10 – 50 mA were considered in combination with the opposite current injection pattern. The reconstruction was performed with the hyperparameter value *a* that yielded a noise factor NF = 1, as discussed above.

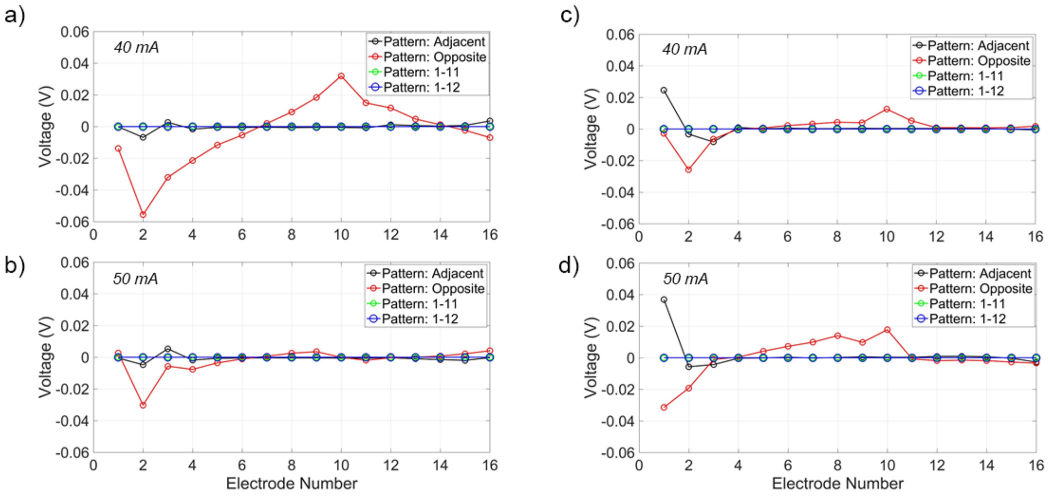

Fig. 3. Voltage changes of GNP/DNA/PEDOT:PSS surfaces due to UV-C irradiation recorded using the sixteen-electrode configuration with different injection patterns and currents of 40 and 50 mA. UV-C exposure: (a, b) 2.6 mW/cm^2 for 24 h; (c, d) 4.0 mW/cm^2 for 24 h.

In the maps, the yellow color indicates a negative change of the normalized electrical conductivity, indicating a local decrease of the sample electrical conductivity, whereas the blue color is associated with a positive conductivity change. A smaller area of the nanocomposite surface was radiated with the aim of evaluating the grade of accuracy of the ERT analysis in locating the surface electrical conductivity changes on the sample after UV-C exposure.

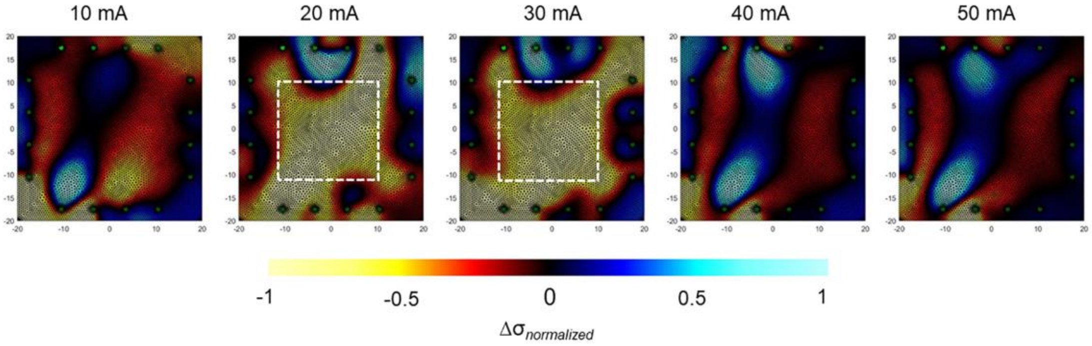

Fig. 4. ERT conductivity change maps of GNP/DNA/PEDOT:PSS film after UV-C irradiation (2.6 mW/cm^2, 24 h) reconstructed using EIDORS. Voltage data recorded with the opposite injection pattern and currents in the range 10-50 mA. The white dashed line denotes the UV-C irradiated area (20 mm × 20 mm).

The white dashed line denotes the central region (20 mm × 20 mm) that was exposed to UV-C, whereas the edges of the sensor surface had been shielded to avoid damage to the electrodes. From the reconstruction of the voltage changes, it was noted that injection currents of 20 and 30 mA provided the best localization of the area exposed to UV, in which a significant loss of electrical conductivity seems to occur. This result was further investigated and confirmed by measurements of the average electrical impedance of the samples (see discussion below and Fig. 7).

Researchers in the biomedical field (Kauppinen et al. [45]) have observed that the impedance obtained from a given current injection and a given voltage measurement could increase, decrease or just be unaffected by a conductivity change in the region of interest, undermining the sensitivity of the EIT approach. This observation may support why some combinations of current intensity and injection patterns were not successful in identifying the surface defects of the current study, and may have been possibly impacted by larger noise. In particular, for the dense opposite pattern, when considering the dimensions of the nanocomposite samples investigated in this study, the enhanced overlapping of the electric flux lines at higher injection currents causes a higher disturbance in the measurements. On the other hand, when using lower injection currents (20-30 mA), it was possible to localize the irradiated area on the samples, by observing the regions in which negative surface conductivity changes occur (in yellow color). Besides the opposite pattern, other injection schemes were also investigated, but did not result in a meaningful correspondence between the irradiated area and the conductivity change maps.

Fig. 5 shows a comparison of the ERT conductivity maps for the nanocomposites irradiated at two different intensities (2.6 and 4.0 mW/cm^2), which were reconstructed from data acquired using the opposite pattern and the injection current of 20 mA. For the surface irradiated at higher intensity, 4.0 mW/cm^2 corresponding to a UV-C dose of 346 J/cm^2 in 24 h, a different conductivity change pattern was observed (Fig. 5b), with a prevalence of areas with positive conductivity changes (in blue color). For conductive composite materials that are fabricated by embedding a carbon-based filler in a polymer matrix, this result is not unexpected, and can be attributed to the large polymer degradation that is caused by exposure to a high dose of UV radiation [46, 47]. In fact, while the matrix is eroded, the conductive filler is progressively exposed causing an apparent increase of the coating electrical conductivity.

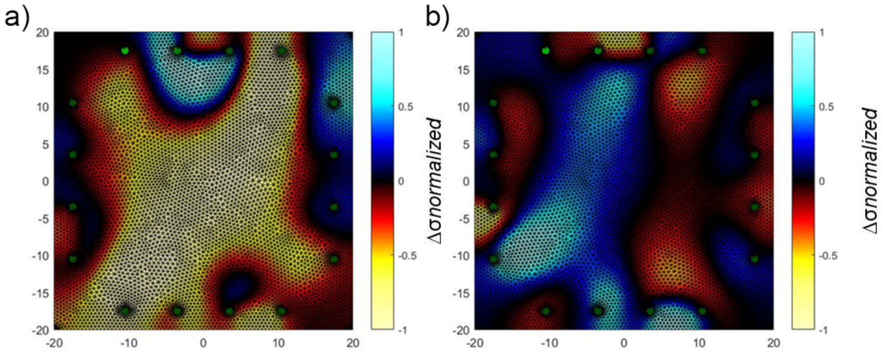

Fig. 5. Reconstructed conductivity change maps of irradiated GNP/DNA/PEDOT:PSS films after exposure to UV-C intensities of (a) 2.6 mW/cm^2 and (b) 4.0 mW/cm^2 (exposure time 24 h). Tests with 20 mA current, opposite injection pattern. The yellow and blue colors indicate negative and positive conductivity changes ($\Delta\sigma_{\text{normalized}}$), respectively.

In our case, the morphology analysis of the GNP/DNA/PEDOT:PSS surfaces exposed to higher UV-C intensity (4.0 mW/cm^2) conducted by SEM revealed a marked difference between the irradiated and non-irradiated samples (Fig. 6). A degradation of the non-conductive component of the nanocomposite coating can be observed after UV-C irradiation: the surface features are characterized by smoother edges than those of the non-irradiated sample, and this observation is more evident in the SEM images at higher magnification (Fig. 6c and d). No changes were detected on the GNP/DNA/PEDOT:PSS sample exposed to lower values of irradiance (2.6 mW/cm^2).

In order to evaluate the accuracy of the results in the conductivity maps reconstructed from the ERT data, further investigations on the GNP/DNA/PEDOT:PSS surfaces under UV-C irradiation were performed. The positive or negative surface conductivity changes in the ERT reconstructed maps, localized in the areas exposed to different intensities of UV-C, were investigated by electrical impedance spectroscopy (EIS) in a traditional two-electrode cell. A lower irradiance (0.63 mW/cm^2) was used in order to obtain a trend of the surface conductivity change as a function of the UV-C dose within 7 days of irradiation tests. The normalized conductivity changes measured after each day of irradiation are reported in Fig. 7. They show a non-linear behavior as a function of the dose. In particular, a significant drop of conductivity was measured after the first day of irradiation (dose of 50 J/cm^2). The conductivity remained approximately constant for the next 2 days, after which a linear increase as a function of the UV-C dose was observed. This result suggests that different levels of UV-C damage might be present at different radiation doses. Consequently, the electrical properties of the irradiated samples may vary significantly with the intensity of the UV-C radiation, leading to the results observed in the ERT conductivity change maps (Fig. 5). The initial drop of conductivity of the irradiated GNP/DNA/PEDOT:PSS films in Fig. 7 can be explained considering the degradation effect that UV radiation has on the conductive PEDOT:PSS matrix. Previous studies have demonstrated that irradiation under UV-C light determines a significant increase of the resistivity values of PEDOT:PSS films due to the decomposition of the polymer chemical bonds [48, 49]. This phenomenon is likely the initial phase of degradation of the GNP/DNA/PEDOT:PSS films, causing the marked conductivity drop during the first 3 days of exposure. This phase is followed by an almost linear increase of the conductivity, which can be related to a progressive exposure of the graphene nanoplatelets component.

Raman spectroscopy provides direct information on molecular vibrational modes, and was therefore used to gain insight into the UV-induced damage mechanism of the nanocomposite films at molecular level. Fig. 8a shows the Raman spectra of the GNP/PEDOT:PSS film before and after UV-C irradiation, recorded using a 532 nm excitation. The strong band observed at 1427 cm^{-1} can be assigned to the symmetric $C_\alpha=C_\beta$ stretching of PEDOT [50], whereas the peak at ~1580 cm^{-1} and the broad band at ~2700 cm^{-1} are the G and 2D peaks of graphene, respectively [51]. A significant decrease of the main PEDOT peak is evident in the spectrum of the irradiated samples. The analysis of the intensities of the PEDOT and GNP characteristic peaks reveals that the value of I_{PEDOT}/I_G changes from 4.0 to 2.1 upon irradiation, while the I_G/I_{2D} value stays approximately the same (from 2.4 to 2.6, typical values for multiple layers of graphene [52]). Similar results were obtained from analysis of the irradiated GNP/DNA/PEDOT:PSS films (Fig. 8b), for which the I_{PEDOT}/I_G value varies from 4.6 to 2.8. For both types of films, the PEDOT component is more affected and degrades more quickly than graphene under UV-C irradiation. This is consistent with the initial conductivity drop measured by electrical impedance spectroscopy (Fig. 7). In the Raman spectra of the GNP/DNA/PEDOT:PSS films, the characteristic peaks of DNA are visible in the 1100 – 1300 cm^{-1} region, with the bands near 1150 and 1256 cm^{-1} due to the vibrational modes of deoxyribose-phosphate and of cytosine and adenine rings, respectively [53, 54]. Both peaks exhibit a marked shift to lower frequency upon irradiation, from 1150 to 1123 cm^{-1} and from 1256 to 1243 cm^{-1}, which has been linked to alteration of the DNA structure [55]. The damage to DNA can be also inferred from the large drop of the

Raman bands in the 1100 – 1300 cm^{-1} region after UV-C irradiation (Fig. 8b). The intensity ratios I_{1150}/I_{1500} and I_{1256}/I_{1500} between the characteristic DNA peaks and the G band of graphene vary from 2.0 to 0.7 and from 1.8 to 0.7, respectively.

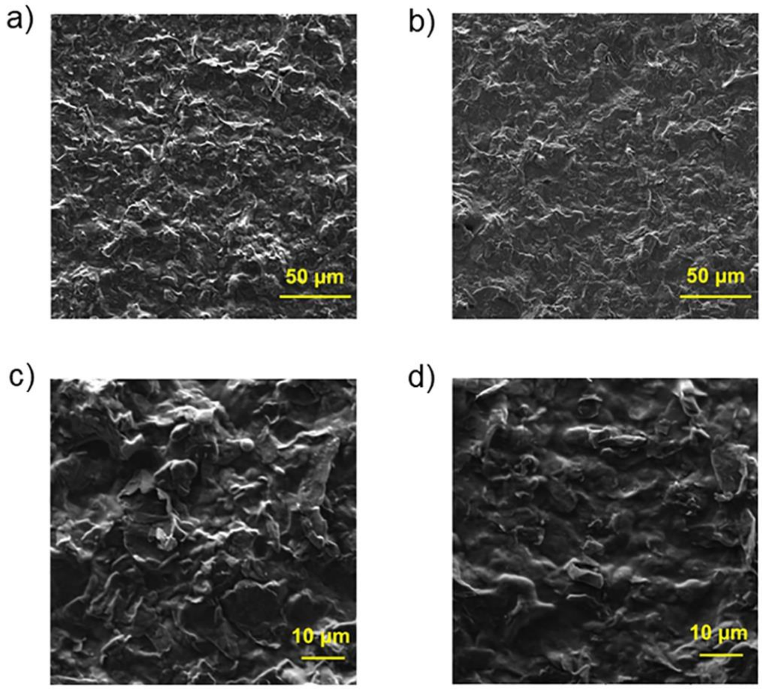

Fig. 6. SEM images of GNP/DNA/PEDOT:PSS nanocomposite surfaces (a, c) before irradiation and (b, d) after UV-C exposure (4.0 mW/cm^2, 24 h) showing local erosion effects on irradiated samples (right). Images acquired with accelerating voltage 10 kV and increasing magnification: (a, b) 1000 X, (c, d) 3000 X.

Collectively, these results indicate that the damage induced by UV-C is localized more on the PEDOT and DNA components of the nanocomposite films, and this is consistent with the conductivity increase observed after the initial degradation of the conductive polymer matrix, due to progressive exposure of the graphene nanoplatelets.

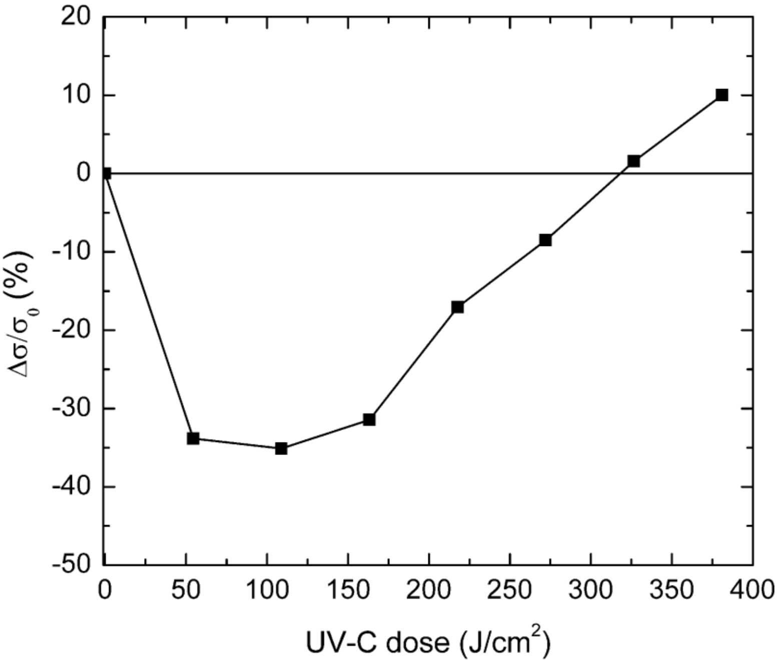

Fig. 7. Surface conductivity changes of irradiated GNP/DNA/PEDOT:PSS films as a function of the UV-C dose determined by electrical impedance spectroscopy in two-electrode measurement cell. Dose range corresponds to irradiation times from 0 to 7 days (UV-C irradiance of 0.63 mW/cm^2).

5.4 Conclusions

Electrical resistance tomography was used to investigate the changes of the surface electrical properties of UV-sensitive nanocomposite films upon exposure to UV-C radiation. The nanocomposite coatings were fabricated by integration of DNA-functionalized graphene nanoplatelets into a conductive polymer matrix made of PEDOT:PSS. The ERT technique was optimized in terms of current patterns and injection values in order to detect damage induced by UV irradiation, with the opposite injection pattern and currents of the order of 20-30 mA giving the most reliable outcome.

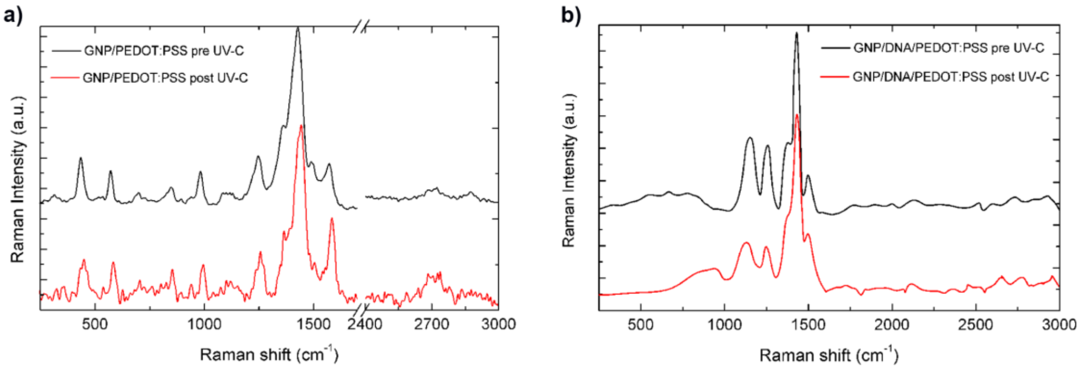

Fig. 8. Raman spectra of (a) GNP/PEDOT:PSS and (b) GNP/DNA/PEDOT:PSS films before and after UV-C irradiation (0.63 mW/cm^2 for 6 days corresponding to a dose of 327 J/cm^2) acquired with an excitation wavelength of 532 nm.

Maps of conductivity changes for the irradiated films were reconstructed from the acquired differential voltage changes with respect to a baseline sample. The nanocomposite area exposed and affected by the UV-C radiation was localized in the ERT maps with good agreement. Different levels of conductivity changes were detected by the technique when exposing the surfaces to different intensities of UV-C radiation. These conductivity changes were verified using 2-electrode impedance spectroscopy. The results were supported by SEM morphology and Raman spectroscopy analyses. In particular, the GNP/DNA/PEDOT:PSS nanocomposite films face different stages of conductivity changes upon irradiation with UV-C light, with an initial drop of the electrical conductivity due to degradation of the conducting polymer matrix, and a subsequent increase related to DNA denaturation and progressive exposure of the GNP. Both situations were captured in the reconstructed conductivity maps, highlighting ERT as an effective technique, and a potential real-time health monitoring method of materials and structures subject to degradation by UV-C radiation.

5.5 References

[1] Soutis C. Fibre reinforced composites in aircraft construction. Progress in Aerospace Sciences. 2005;41(2):143-151.

[2] Mallick PK. Fiber-reinforced composites: materials, manufacturing, and design: CRC press 2007.

[3] Dever JA, Miller SK, Sechkar EA, Wittberg TN. Space environment exposure of polymer films on the materials international space station experiment: results from MISSE 1 and MISSE 2. High Perform Polym. 2008;20(4-5):371-387.

[4] Dever J, Banks B, de Groh K, Miller S. Degradation of spacecraft materials. Handbook of environmental degradation of materials. 2005:465-501.

[5] Hastings D, Garrett H. Spacecraft-environment interactions: Cambridge University Press 2004.

[6] Minton TK, Garton DJ. Dynamics of atomic-oxygen-induced polymer degradation in low earth orbit. In: Dressler RA, editor. Chemical dynamics in extreme environments, vol. 11 Singapore: World Scientific Publishing; 2001. p. 420-489.

[7] Clausi M, Santonicola MG, Schirone L, Laurenzi S. Analysis of ultraviolet exposure effects on the surface properties of epoxy/graphene nanocomposite films on Mylar substrate. Acta Astronaut. 2017;134:307-313.

[8] Yang XF, Li J, Croll S, Tallman D, Bierwagen G. Degradation of low gloss polyurethane aircraft coatings under UV and prohesion alternating exposures. Polym Degrad Stab. 2003;80(1):51-58.

[9] Clausi M, Laurenzi S, La Saponara V, Santonicola MG. Multifunctional sensors for UV and mechanical damage detection of aerospace structures. Proceedings of the International Astronautical Congress, IAC, 2016.

[10] Toto E, Santonicola MG, Mancini MC, Laurenzi S. Ultraviolet-sensing surfaces based on hybrid nanocomposites for radiation monitoring systems. IEEE International Workshop on Metrology for AeroSpace (MetroAeroSpace), 2017. p. 369-373.

[11] Munakata N, Makita K, Bolsée D, Gillotay D, Horneck G. Spore dosimetry of solar UV radiation: applications to monitoring of daily irradiance and personal exposure. Adv Space Res. 2000;26(12):1995-2003.

[12] Loyola BR, Briggs TM, Arronche L, Loh KJ, La Saponara V, O’Bryan G, et al. Detection of spatially distributed damage in fiber-reinforced polymer composites. Struct Health Monit. 2013;12(3):225-239.

[13] Loyola BR, La Saponara V, Loh KJ, Briggs TM, O'Bryan G, Skinner JL. Spatial sensing using electrical impedance tomography. IEEE Sens J. 2013;13(6):2357-2367.

[14] Gallo GJ, Thostenson ET. Spatial damage detection in electrically anisotropic fiber-reinforced composites using carbon nanotube networks. Compos Struct. 2016;141:14-23.

[15] Zhao L, Yang J, Wang K, Semperlotti F. An application of impediography to the high sensitivity and high resolution identification of structural damage. Smart Mater Struct. 2015;24(6):065044.

[16] Tallman TN, Wang K. Damage and strain identification in multifunctional materials via electrical impedance tomography with constrained sine wave solutions. Struct Health Monit. 2016;15(2):235-244.

[17] Hallaji M, Pour-Ghaz M. A new sensing skin for qualitative damage detection in concrete elements: Rapid difference imaging with electrical resistance tomography. NDT & E International. 2014;68:13-21.

[18] Loh KJ, Hou T-C, Lynch JP, Kotov NA. Carbon nanotube sensing skins for spatial strain and impact damage identification. J Nondestruct Eval. 2009;28(1):9-25.

[19] Hou T-C, Loh KJ, Lynch JP. Spatial conductivity mapping of carbon nanotube composite thin films by electrical impedance tomography for sensing applications. Nanotechnology. 2007;18(31):315501.

[20] Schueler R, Joshi SP, Schulte K. Damage detection in CFRP by electrical conductivity mapping. Compos Sci Technol. 2001;61(6):921-930.

[21] Baltopoulos A, Polydorides N, Pambaguian L, Vavouliotis A, Kostopoulos V. Damage identification in carbon fiber reinforced polymer plates using electrical resistance tomography mapping. J Compos Mater. 2013;47(26):3285-3301.

[22] Baltopoulos A, Polydorides N, Pambaguian L, Vavouliotis A, Kostopoulos V. Exploiting carbon nanotube networks for damage assessment of fiber reinforced composites. Composites Part B. 2015;76:149-158.

[23] Pedrazzoli D, Dorigato A, Pegoretti A. Monitoring the mechanical behavior under ramp and creep conditions of electrically conductive polymer composites. Composites Part A. 2012;43(8):1285-1292.

[24] Böger L, Wichmann MH, Meyer LO, Schulte K. Load and health monitoring in glass fibre reinforced composites with an electrically conductive nanocomposite epoxy matrix. Compos Sci Technol. 2008;68(7):1886-1894.

[25] Nofar M, Hoa S, Pugh M. Failure detection and monitoring in polymer matrix composites subjected to static and dynamic loads using carbon nanotube networks. Compos Sci Technol. 2009;69(10):1599-1606.

[26] Tallman T, Gungor S, Wang K, Bakis C. Tactile imaging and distributed strain sensing in highly flexible carbon nanofiber/polyurethane nanocomposites. Carbon. 2015;95:485-493.

[27] Lestari W, Pinto B, La Saponara V, Yasui J, Loh KJ. Sensing uniaxial tensile damage in fiber-reinforced polymer composites using electrical resistance tomography. Smart Mater Struct. 2016;25(8):085016.

[28] Santonicola MG, Coscia MG, Sirilli M, Laurenzi S. Nanomaterial-based biosensors for a real-time detection of biological damage by UV light. Proceedings of the Annual International Conference of the IEEE Engineering in Medicine and Biology Society, vol. 2015-November Milan, Italy: IEEE EMBS; 2015. p. 4391-4394.

[29] Botti S, Laurenzi S, Mezi L, Rufoloni A, Santonicola MG. Surface-enhanced Raman spectroscopy characterisation of functionalised multi-walled carbon nanotubes. Phys Chem Chem Phys. 2015;17(33):21373-21380.

[30] Botti S, Rufoloni A, Laurenzi S, Gay S, Rindzevicius T, Schmidt MS, et al. DNA self-assembly on graphene surface studied by SERS mapping. Carbon. 2016;109:363-372.

[31] Santonicola MG, Coscia MG, Botti S, Laurenzi S. Graphene/DNA nanostructured films for bioinspired sensing of UV radiation effects. Proceedings of the International Astronautical Congress, IAC, vol. 9, 2014. p. 6313-6317.

[32] Gueymard CA. The sun's total and spectral irradiance for solar energy applications and solar radiation models. Solar Energy. 2004;76(4):423-453.

[33] Holder D, Tidswell T. Electrical Impedance Tomography: Methods, History and Applications. Bristol: Institute of Physics Publishing; 2006.

[34] Gildner TK. Damage and Stress Concentration Identification in CFRP Composite Structures with Electrical Resistance Tomography and Digital Image Correlation. MS Thesis, University of California, Davis, 2017.

[35] Gisser DG, Isaacson D, Newell JC. Current topics in impedance imaging. Clin Phys Physiol Meas. 1987;8(Suppl A):39-46.

[36] Hua P, Woo EJ, Webster JG, Tompkins WJ. Iterative reconstruction methods using regularization and optimal current patterns in electrical impedance tomography. IEEE Transactions on Medical Imaging. 1991;10(4):621-628.

[37] Vauhkonen M, Lionheart WRB, Heikkinen LM, Vauhkonen PJ, Kaipio JP. A MATLAB package for the EIDORS project to reconstruct two-dimensional EIT images. Physiol Meas. 2001;22:107-111.

[38] Adler A, Lionheart WR. Uses and abuses of EIDORS: an extensible software base for EIT. Physiol Meas. 2006;27(5):25-42.

[39] Lionheart W, Polydorides N, Borsic A. The reconstruction problem. In: Holder DS, editor. Electrical Impedance Tomography: Methods, History and Applications, Bristol: Institute of Physics Publishing; 2005. p. 3-64.

[40] Graham BM, Adler A. Objective selection of hyperparameter for EIT. Physiol Meas. 2006;27(5):S65-S79.

[41] Adler A, Guardo R. Electrical impedance tomography: regularized imaging and contrast detection. IEEE Transactions on Medical Imaging. 1996;15(2):170-179.

[42] Dai H, Gallo GJ, Schumacher T, Thostenson ET. A Novel Methodology for Spatial Damage Detection and Imaging Using a Distributed Carbon Nanotube-Based Composite Sensor Combined with Electrical Impedance Tomography. J Nondestruct Eval. 2016;35(26):1-15.

[43] Shi X, Dong X, Shuai W, You F, Fu F, Liu R. Pseudo-polar drive patterns for brain electrical impedance tomography. Physiol Meas. 2006;27(11):1071-1080.

[44] Kolehmainen V, Vauhkonen M, Karjalainen PA, Kaipio JP. Assessment of errors in static electrical impedance tomography with adjacent and trigonometric current patterns. Physiol Meas. 1997;18(4):289-303.

[45] Kauppinen P, Hyttinen J, Malmivuo J. Sensitivity Distribution Visualizations of Impedance Tomography Measurement Strategies. Int J Bioelectromagnetism. 2006;8(1):63-71.

[46] Toto E, Palombi M, Laurenzi S, Santonicola MG. Functional nanocomposites with graphene-DNA hybrid fillers: Synthesis and surface properties under UV irradiation. Ceram Int. in press https://doi.org/10.1016/j.ceramint.2018.10.236.

[47] Petersen EJ, Lam T, Gorham JM, Scott KC, Long CJ, Stanley D, et al. Methods to assess the impact of UV irradiation on the surface chemistry and structure of multiwall carbon nanotube epoxy nanocomposites. Carbon. 2014;69:194-205.

[48] Nagata T, Oh S, Chikyow T, Wakayama Y. Effect of UV–ozone treatment on electrical properties of PEDOT:PSS film. Organic Electronics. 2011;12(2):279-284.

[49] Elschner A. The spectral sensitivity of PEDOT:PSS films. Sol Energy Mater Sol Cells. 2011;95(5):1333-1338.

[50] Garreau S, Louarn G, Buisson JP, Froyer G, Lefrant S. In Situ Spectroelectrochemical Raman Studies of Poly(3,4-ethylenedioxythiophene) (PEDT). Macromolecules. 1999;32(20):6807-6812.

[51] Ferrari AC, Meyer JC, Scardaci V, Casiraghi C, Lazzeri M, Mauri F, et al. Raman Spectrum of Graphene and Graphene Layers. Phys Rev Lett. 2006;97(18):187401.

[52] Reina A, Jia X, Ho J, Nezich D, Son H, Bulovic V, et al. Large Area, Few-Layer Graphene Films on Arbitrary Substrates by Chemical Vapor Deposition. Nano Lett. 2009;9(1):30-35.

[53] Duguid JG, Bloomfield VA, Benevides JM, Thomas GJ. DNA melting investigated by differential scanning calorimetry and Raman spectroscopy. Biophys J. 1996;71(6):3350-3360.

[54] Overman SA, Aubrey KL, Reilly KE, Osman O, Hayes SJ, Serwer P, et al. Conformation and interactions of the packaged double-stranded DNA genome of bacteriophage T7. Biospectroscopy. 1998;4(S5):S47-S56.

[55] Ke W, Yu D, Wu J. Raman spectroscopic study of the influence on herring sperm DNA of heat treatment and ultraviolet radiation. Spectrochim Acta Part A. 1999;55(5):1081-1090.

Chapter 6 - *Hydrophobic multi-layered graphene-based nanocomposite films spray-coated on textured aluminum substrate with high thermal conductivity*[5]

---

[5] Work in collaboration with Italian Institute of Technology (IIT) under the supervision of Dr. Ilker S. Bayer. This work is part of a European project partnership [H2020 project (HARMoNIC – HierARchical Multiscale NanoInterfaces for enhanced Condensation processes; EU project Grant Agreement 801229)]

Abstract

The design and development of graphene-based nanocomposite films are receiving great interest, due to their multifunctional properties, with potential applications in a wide range of technological areas. From aerospace to chemical sector, such nanocomposite films are investigating as (bio)sensors, electromagnetic interference shielding materials, thermal interface materials (TIMs) and for thermal energy harvesting. In this work, we reported the development of hydrophobic multi-layered graphene-based nanocomposite films on textured aluminum substrate. The formulated nanocomposite conductive inks were spray-coated on textured aluminum substrate surfaces by forming nanocomposite films ranging from 1 to 10 layers. The effects of thermal annealing on morphology, surface topography properties, surface hydrophobicity and on the thermal properties of the fabricated nanocomposite films were investigated. In particular, from electron microscopy analysis, we detected that, thermal annealing compresses the fabricated graphene-based nanocomposite films, resulting in a thinner, less rough and compacted coatings, almost similar to 'all-graphene nanoplatelets' films. Hence, we obtained that thermal annealing is able to increase thermal properties of the fabricated films, with an enhancement of the thermal conductivity up to ~ 759%, without altering the hydrophobic nature of their nanocomposite surfaces.

6.1 Introduction

Graphene-based nanocomposite films have attracted significant attention as multifunctional coatings with given thermal, electrical, optical properties, that can bring relevant progress in a wide range of technological applications, from aerospace to chemical industry. Graphene nanoparticles, in fact, for their high stiffness and strength[1] combined with exceptional electrical[2, 3] and thermal properties[4, 5], allow the fabrication of the resulting composite material with superior features at relatively low loadings[6-10]. For example, potential applications in the electronics sector include the possibility to use such materials in the field-effect transistors (MOSFETs) technology[11-13], as an alternative to the most common silicon semiconductor used, in view of the miniaturization of next-generation electronic components [11, 14]. One of the most promising concepts is the use of carbon-based nanocomposite films, due to high intrinsic thermal conductivity of the carbon nanoparticles [5], as thermal interface materials (TIMs)[15] to dissipate heat in a large number of electronic devices[16, 17]. Marconnet et al.[18], for example, fabricated aligned CNT arrays reinforced epoxy polymer matrix, for thermal interface applications, obtaining a thermal conductivity enhancement, in the axial direction, of a factor 18.5 with 16.7vol.% of CNT respect to the epoxy matrix. Multifunctional nanocomposite films are currently investigated also in the aerospace field to create UV-sensors[19, 20] with the aim, for example, to monitor the radiation absorbed by the astronauts during extra vehicular activities (EVA), as inner layers of multi-layer insulation (MLI) blankets for satellites to reduce the unwanted interference and passive intermodulation products problems due to its high radio frequency reflectivity (RF) in the specular direction [21] or as new and advanced grounding systems to mitigate plasma-induced spacecrafts charging [22]. In addition, carbon-based nanocomposite films can be useful in robotics industry as pressure sensors [23] and in flexible [24] and touch-screen technologies [25], as materials with biosensing[26, 27] and gas-sensing [28, 29] properties and as multifunctional materials for (thermal)energy harvesting [11, 30-33].

The purpose of this work is to achieve thermal performance of the unit increased over time, resulting in an ideal design of heat exchangers thanks to the application of efficient nanocomposite coatings. It's well-known, in fact, that dropwise condensation as opposed to filmwise condensation can lead to much higher heat transfer coefficients, improving so the energy efficiency in a large variety of engineering applications. The main objective of this work so, is to fabricate promising graphene-based nanocomposite films on aluminum substrate with high thermal conductivity and evaluate the effects of thermal annealing on its surface hydrophobicity and thermal properties that are relevant parameters to improving the efficiency of thermal power generation. For this study, we fabricated multi-layered nanocomposite films (ranging from 1 to 10 layers), deposited on aluminum substrates, with graphene nanoplatelets embedded in PVDF-DMAc solution, by spray-coating process. Aluminum was chosen as substrate for the nanocomposite films as it is a metal largely used in several industrial sectors, especially in the heat exchangers [34-36]. We performed, at last, thermal annealing with a carver press, by placing the dried samples between two metal plates at 150°C for 10 minutes under 0.5 metric tons of applied pressing load. A further objective is to investigate the effect of thermal annealing on morphology and surface texture properties of the graphene-based nanocomposite films on aluminum substrate.

6.2 Experimental

6.2.1 Materials

Graphene nanoplatelets (GnPs), purchased from STREM Chemicals Inc. (UK), with thickness of 6-8 nm, wide of 5 µm, an oxygen content of <1%, a carbon content of 99.5 wt.% and a residual acid content of <0.5 wt.% were used as nanofillers. Polyvinylidene fluoride (PVDF) thermoplastic polymer, with molecular weight (g/mol) of 64.035, was purchased from Alfa Aesar^{TM} Chemicals (Thermo Fisher Scientific, USA) and it was chosen as polymer matrix in this study. PVDF powder was dispersed in N,N-Dimethylacetamid (DMAc) solvent (Merck KgaA, Germany) and then acetone solvent was added and used as received. Aluminum samples (5 cm × 2 cm), namely 'Al-Front', 'Al-Back' sheets with a thickness of 30 μm and 'Al-Thick' piece with a thickness of 1.2 mm, were used as substrates for the spray-coated nanocomposite films.

6.2.2 Fabrication of multi-layered nanocomposite films

Multi-layered graphene-based nanocomposite films were fabricated by spray-coating the ink of graphene nanoplatelets and PVDF-DMAc-acetone solution on aluminum substrate, followed by thermal drying at 150°C for a few seconds after each layer deposition. In particular, we dissolved PVDF powder into DMAc solvent with a PVDF weight percentage of 10 wt.%. PVDF powder was completely dispersed in DMAc solvent by continuous magnetic-stirring for 6 hours at room temperature (RT) and after that, graphene nanoplatelets were added to the clear PVDF/DMAc solution at different weight percentages, ranging from 10 to 60 wt.% respect to the PVDF content. At last, acetone solvent was added to the final graphene-nanocomposite mixture in a ratio 1:1 (wt./wt.) with the PVDF/DMAc solution to decrease the viscosity of the that final mixture. The formulated nanocomposite inks were manual stirred for 5 min at room temperature and then, in order to further improve the fillers dispersion in the polymer, the inks were sonicated for 2 minutes with an ultrasonic probe (40% amplitude, 20kHz frequency, Sonics & Materials Inc.). The nanocomposite films were deposited on aluminum substrates by spray-coating process (airbrush spray system, model VL-SET, Paasche) and by tilting of 30° the surface targets (aluminum substrates) respect to the floor. We used, in this study 3 different types of aluminum substrates, namely ‘Al-Front’, ‘Al-Back’ and ‘AL-Thick’. The distance between the spray-gun nozzle and aluminum substrate was fixed at 10 cm and the spraying pressure applied was fixed at 1.5 bar. The deposition of each layer was obtained through the same multi-passes in vertical and horizontal spraying directions. After each nanocomposite layer deposition, we immediately gently dried it at 150°C with a thermogun for a few seconds. We obtained that, following the same deposition protocol for all films fabricated, the thickness of each layer is ~ 3.0±2.1 μm by using ~ 0.3 ml of the formulated nanocomposite ink. The thickness of a nanocomposite layer was measured using a 3D optical profilometer at 50× magnification with accuracy of 0.05 μm. Thickness measurements were repeated several times in different spots of the film and the obtained values were averaged. In this work, we characterized and analyzed films from 3 layers because from those we can obtain a total and uniform nanocomposite film coverage on aluminum substrate. After the film deposition process, we performed thermal annealing with a carver press, by placing the samples between two metal plates at 150°C for 10 minutes with an applied pressing load of 0.5 metric tons. PVDF polymer film, without graphene nanoplatelets, coated on aluminum substrate, was also fabricated and used as control sample.

6.2.3 Surface topography characterization

Surface texture properties of the aluminum substrates and of fabricated multi-layered nanocomposite films were investigated by 3D Optical Profilometer provided by Zeta Instruments. Different magnifications, ranging from 2.5× to 50×, with a Z profile resolution ranging from 25 μm to 0.05 μm respectively, were applied in order to appropriately calculate the surface topography properties of the samples. The measured parameters were the arithmetic mean surface roughness S_a, the root mean square of heights S_q, the skewness S_{sk} and the kurtosis S_{ku}, defined as:

$$S_a = \frac{1}{NxM}\sum_{j=1}^{N}\sum_{i=1}^{M}|z_{i,j}| \tag{1}$$

$$S_q = \sqrt{\frac{1}{NxM}\sum_{j=1}^{N}\sum_{i=1}^{M}(z_{i,j})^2} \tag{2}$$

$$S_{sk} = \frac{1}{(NxM)S_q^3}\sum_{j=1}^{N}\sum_{i=1}^{M}\left(z_{i,j}\right)^3 \tag{3}$$

$$S_{sk} = \frac{1}{(NxM)S_q^4}\sum_{j=1}^{N}\sum_{i=1}^{M}\left(z_{i,j}\right)^4 \tag{4}$$

where, z is the profile vertical direction respect to the mean plane and M and N are the numbers of sampled points in x and y directions respectively. In particular, S_a (eq.1) represents the most common surface property investigated and it describes the height variations in the sample surface (the units are generally micrometers). On the contrary, the skewness (eq. 3) and kurtosis (eq. 4) are non-dimensional parameters and they describe the asymmetry of surface heights respect the mean plane and the asymmetry of peakedness of surface heights, respectively. It means that, for example, a sample surface with positive skewness and high kurtosis will show spiky topographic features; on the contrary for negative skewness and low kurtosis (considering that kurtosis of a Gaussian distribution is equal to 3.0), the sample surface will be blunter. The all-above described parameters were calculated in different spots of the samples and their average values were considered in the analysis.

3D Optical Profilometer was also used to determine the thickness of the graphene-based nanocomposite layers.

6.2.4 Dewetting phenomenon and mechanical abrasion description of aluminum substrates

As mentioned above, we considered as target substrates 3 types of aluminum samples, different for thickness, surface finish due to manufacturing process and roughness, with the aim to study which one is the best to obtain a good adhesion between substrate and film. The aluminum substrates used are: the first Al substrate called ‘Al-Front’, the second one ‘Al-Back’ and the third one ‘Al-Thich’. The ‘Al-Front’ and ‘Al-Back’ sheets have a thickness of 30 µm and vertical lay-bright and mill-matte surface finishes respectively. The thicker third one, ‘Al-Thich’, has a thickness of 1.2 mm and the same surface finish in both size of the piece. After the first deposition, we found that the formulated (PVDF-DMAc)/GnPs inks dewetted on all above-mentioned aluminum substrates: in particular, we noted a formation of different and irregular patterns of nanocomposite droplets depending on the surface finish and roughness of each aluminum substrate. It’s well-known that, in fact, dewetting phenomenon is influenced by several factors including surface and morphological properties of the substrate [37] and, for this reason, we investigated, in order to understand how to avoid the phenomenon under study, the surface texture properties of all aluminum substrates. Fig. 1 shows the optical microscope images of Al-Front (a), Al-Back (c) and Al-Thick (e) aluminum substrates with their average measured S_a, and the correspondent optical images of dewetting patterns formed (b,d and e). In particular we noted that, in the case of Al-Front aluminum substrate (Fig. 1, a), characterized by a striped surface due to the manufacturing process and by the lowest arithmetic mean surface roughness S_a of 0.08±0.02 μm, dewetting phenomeno results from the formation of separate droplets with different heights of its well-defined rims (Fig. 1, b). On the contrary, in the case of not-striped and rougher Al-Back (Fig.1, c) and Al-Thick (Fig.1, e) surfaces, it’s visible the formation of a periodic structure of strings of material (Fig. 1, d and f respectively) that results in a greater spreading of nanocomposite film especially on the roughest Al-Thick substrate having S_a of 0.31±0.10 μm.

For these reasons, to ensure the fabrication of nanocomposite films and avoid dewetting problem, we adopted the easy and fast technique of mechanical abrasion, with the aim to create

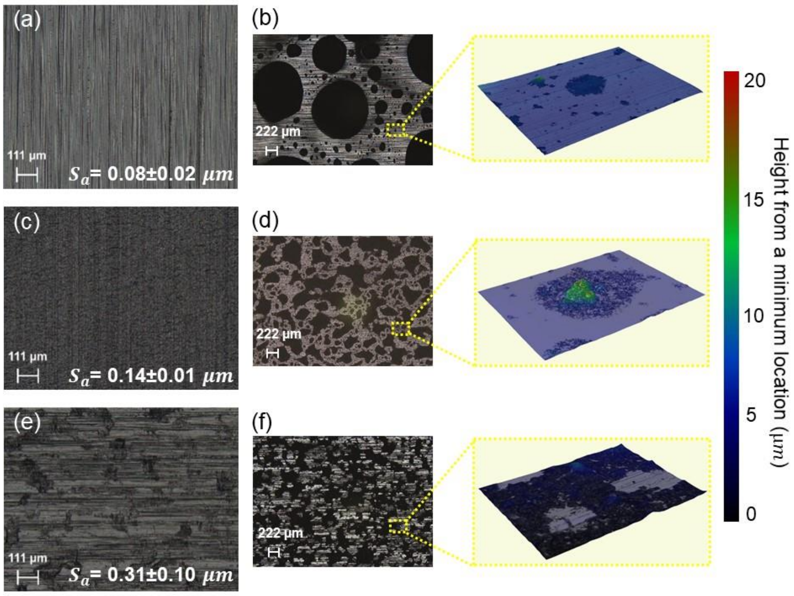

Fig. 1. Optical microscope images of the top surface of aluminum substrates Al-Front (a), Al-Back (c) and Al-Thick (e). The images were taken at 20× magnification. In (b), (d) and (e) there are the optical images of dewetting patterns formation on each correspondent aluminum substrate taken at 2.5× magnification with a zoom of each at 50× magnification. Different colors indicate the height (μm) from a minimum location.

rougher aluminum surfaces. We abraded, following different protocols, the 3 above-mentioned aluminum substrates by using the same type of silicon carbide abrasive papers. In particular, in order to understand how different abrasive parameters influence the texture properties of the aluminum surfaces, we used abrasive papers with different grains size, two different abrasion direction movements (linear and circular) and different abrasion times. Three different abrasive methods were used for Al-Front aluminum substrate. Abrasive methods used are as follows: the first method is to use the P1200 abrasive paper, applying linear and rotatory movements for 30 minutes and the abraded sample was called ‘Al-F1’; the second method consist to use a combination of 3 abrasive papers, namely P600-P800-P1200, applying linear and rotatory movements for a lower time of 8 minutes and the abraded sample was called ‘Al-F2’; at last, in the third method we used the same combination abrasive papers used in the second method, but using only linear movements for 8 minutes and in this case the abraded sample was called ‘Al-F3’.For Al-Back aluminum substrate, two different abrasive methods were used, that are: the first method is to use P1200 abrasive paper, applying linear movements for 60 seconds and the sample abraded following this protocol was called ‘Al-B1’; the second method is to use P800 abrasive paper, applying linear movements for 60 seconds and the abraded sample was called ‘Al-B2’.At last, the thicker Al-Thick aluminum substrate was abraded also following two different abrasive methods. In this case the abrasive methods used are as follows: the first method is to use the P600 abrasive paper, applying linear movements for 60 seconds and the abraded sample was called ‘Al-T1’; the second method consists to use P120 abrasive paper, applying linear movements for 60 seconds and the abraded sample was called ‘Al-T2’. All abrasive methods used were repeated several times. After abrasion we washed the aluminum substrates with water and ethanol solvent in order to remove contaminants and silicon carbide residues resulting from the abrasive papers. We found that, for all of these abrasive methods adopted, dewetting phenomenon did not occur on abraded aluminum substrates. In this study, ‘Al-T1’ was chosen as abraded aluminum substrate for the spray-coated nanocomposite films. In the section 3.1 are presented the motivations for this.

6.2.5 Morphological characterization

In order to assess the morphology of nanocomposite surfaces, we used a Scanning Electron Microscopy (SEM JSM-6490LA series, JEOL, Japan) operating with 10 kV of acceleration voltage and magnification in the range 1000×-3000×. Energy dispersive X-ray (EDX) spectroscopy analysis was also performed on cross sections of nanocomposite films, before and after thermal annealing, in order to identify the distribution of the occurring materials along the aluminum substrate. For the surfaces of fracture analysis, the nanocomposite films were deposited on a thinner aluminum substrate and then the samples were fractured by using cryogenic liquid nitrogen. Cross sections SEM images, in combination with 3D Optical Profilometer, were also used to determine the thickness of the graphene-based nanocomposite layers.

6.2.6 Water contact angle characterization

Water contact angles were measured by the sessile drop method using a DataPhysics OCA 20 analyzer (DataPhysics Instruments, Germany) (Fig.4, a). Water was dispensed through the Hamilton syringe of 0.5-mL volume. The spreading kinetics of water drops on all nanocomposite films was analyzed as a function of time until equilibrium was reached (up to 140 sec.). Values of the water contact angles were determined by curve fitting with the Young-Laplace equation using the DataPhysics software provided with the instrument. A minimum of 10 drops (volume of 5 µl and dosing rate 1 µl/s) in different spots of the sample surface were analyzed.

6.2.7 Thermal properties measurements characterization

Thermal measurements of the nanocomposite films were carried out using C-Therm TCi Thermal Analyzer Device (Fig. 2).

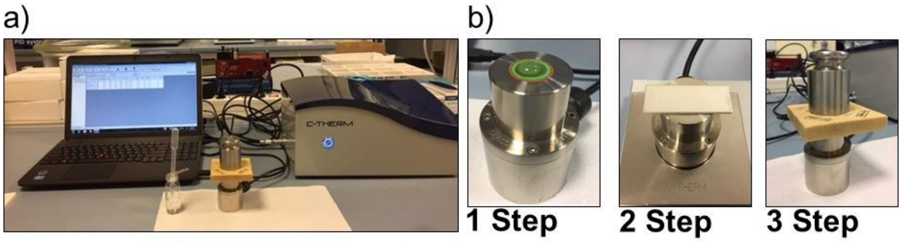

Fig. 2. Experimental set-up for thermal measurements of nanocomposite films deposited by spray-coating on abraded aluminum substrate. a) Thermal Analyzer Device C-Therm TCi and in (b) steps for thermal measurements. 1 Step: deposition of drops of water as contact agent; 2 Step: sample placed on thermal sensor; 3 Step: weight of 500g placed to ensure a stronger contact between sensor and sample.

Modified transient plane source (MTPS) technique, conforms to ASTM D7984, was applied to characterize the thermal properties of the samples. Nanocomposite film samples were placed on interfacial heat reflectance circular sensor (diameter of 2 cm) surrounded by a guarded ring. A piece of insulator material was placed on the sample and on the top a weight of 500g was positioned to ensure a stronger contact between sensor and sample. Three drops of water as contact agent were deposited at sensor-sample interface. The applied heat source from the sensor to the sample allows to measure the thermal properties of the sample. The measured parameters were the thermal conductivity λ and the thermal effusivity ε. The measurements were collected under the same conditions of temperature (T=20.5°C) and the thickness of all samples tested can be substantially approximated to the thickness of Al-substrate (Al-T1) that is equal to 1.2 mm. From the λ and ε measurements we determined thermal diffusivity α as $\alpha = \lambda/\varepsilon$. The thermal conductivity variation of nanocomposite films on Al-T1 substrate, before and after thermal annealing, was calculated according to the following formula:

$$\Delta\lambda^* = \lambda - \lambda_0 \tag{1}$$

where λ_0 is the thermal conductivity of PVDF film coated Al-T1 aluminum surface without graphene nanoplatelets. The normalized thermal conductivity, effusivity and diffusivity changes over the increase of a number of film layers were calculated as:

$$\Delta\lambda^*_{normalized} = (\lambda - \lambda_0) / \lambda_0 \tag{2}$$

$$\Delta\varepsilon^*_{normalized} = (\varepsilon - \varepsilon_0) / \varepsilon_0 \tag{3}$$

$$\Delta\alpha^*_{normalized} = (\alpha - \alpha_0) / \alpha_0 \tag{4}$$

where ε_0 and α_0 are the thermal effusivity and diffusivity respectively of PVDF film on aluminum surface without graphene nanoplatelets. A minimum of 20 measurements were performed for each nanocomposite sample tested.

6.3 Results and discussion

6.3.1 Surface topographic analysis of abraded aluminum substrates

The surface topographic analysis was conducted to obtain information on the changes of surface roughness of the aluminum substrates after mechanical abrasions that is a relevant parameter to improving the film wettability on the substrate and to avoid the unwanted dewetting phenomenon. Table 1 summarizes the surface texture properties of all abraded and not aluminum substrates. In particular we found that after abrasion S_a increases in all cases, leading to a complete spreading of nanocomposite ink on abraded aluminum substrates, and in the same time surface features remain substantially nearly symmetric with S_{sk} close to 0.0 and nearly Gaussian with S_{ku} close to 3.0, except in the case of Al-F3 in which we obtained the lowest and highest skewness and kurtosis respectively. It means that mechanical abrasion does not substantially affect the feature shapes of the aluminum samples.

Fig. 3 shows the 3D optical profilometer surface images of all abraded aluminum substrates, except of the worst Al-F3, with the images of the nanocomposite films fabricated.

Table 1. Surface texture properties of aluminum substrates Al-Front, Al-Back and Al-Thick and of respective abraded aluminum substrates.

Al substrate	S_a (μm)	S_q	S_{sk}	S_{ku}
Al-Front	0.08±0.02	0.10±0.02	0.31±0.08	2.85±0.88
Al-F1	0.34±0.10	0.44±0.14	-0.54±0.54	2.97±0.38
Al-F2	0.47±0.12	0.58±0.13	-0.56±0.31	3.18±0.84
Al-F3	0.33±0.09	0.43±0.12	-1.07±0.24	4.39±0.74
Al-Back	0.14±0.01	0.18±0.01	0.01±0.15	3.03±0.11
Al-B1	0.17±0.11	0.21±0.10	-0.11±0.52	3.59±0.23
Al-B2	0.21±0.01	0.28±0.02	-0.72±0.38	3.93±0.83
Al-Thick	0.31±0.10	0.41±0.12	-0.99±0.36	3.70±0.86
Al-T1	0.81±0.01	1.03±0.01	-0.35±0.10	3.35±0.18
Al-T2	1.43±0.24	1.80±0.28	0.49±0.02	3.75±0.32

In this study, we decided to analyzed nanocomposite films spray-coated on abraded aluminum substrate Al-T1 (Fig. 3, g), because it has a mean surface roughness S_a of 0.81±0.01 such that the adhesion of nanocomposite films on Al-T1 substrate is very strong (Fig. 3, i). In fact, for example the abraded aluminum samples Al-B1 and Al-B2, show a lower S_a that not permits a good adhesion of the film on the substrate especially for films with a large number of layers (since 4 and up) and so peeling off problem occurs (Fig. 3, f). In addition, Fig. 3, g shows the surface height distribution of Al-T1 substrate at 20× magnification and it is evident that there is a uniform distribution of height and shape of peaks and valleys across the surface: in fact, it has surface features nearly symmetric and

Gaussian with a skewness of -0.35±0.10 and kurtosis of 3.35±0.18. Moreover, the abrasion time of 60 seconds to fabricate Al-T1 is the lowest time compared to that one considered to fabricate Al-F1, Al-F2 and Al-F3 surfaces, and for that reason we preferred it to the last ones without losing the uniformity and symmetry of the surface features.

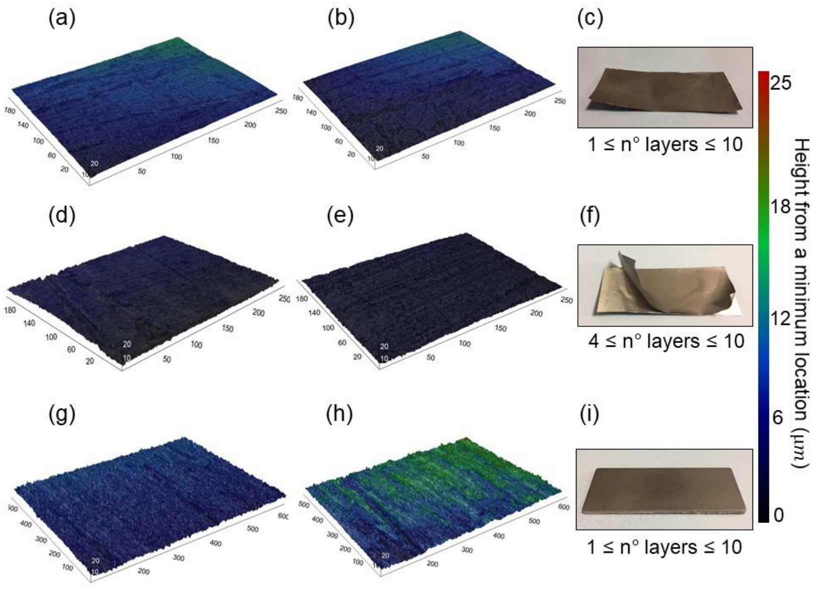

Fig. 3. 3D surface images, acquired by 3D optical profilometer, of abraded Al-F1 (a), Al-F2 (b), Al-B1 (d), Al-B2 (e), Al-T1 (g) and Al-T2 (h) aluminum substrates. (a,b,c,d,e) 3D surface images acquired at 50× magnification; (g,h) images acquired at 20× magnification. (c,f,i) Pictures of the deposited nanocomposite films: (c) view of nanocomposite film deposited on Al-F1(the same quality obtained for Al-F2 substrate); (f) nanocomposite films peeled off from the Al-B1 substrate (peeling off problem occurs also for Al-B2 substrate); (i) view of the nanocomposite film deposited on Al-T1 (the same quality obtained for Al-T2 substrate). Different colors indicate the height (μm) from a minimum location.

6.3.2 Scanning electron microscopy (SEM) and energy dispersive X-ray (EDS) spectroscopy analysis

The SEM images of nanocomposite films, before (a) and after (b) 10 minutes of thermal annealing at 150°C, at magnification of 1000x and 3000x (insets in a and b) are shown in Fig. 4. From the analysis of SEM images, a morphological difference is clearly visible of the nanocomposite surface: in fact, before thermal annealing the GnPs edges are sharp and well-defined respect to the after thermal annealing case in which GnPs are compacted and closer with smoother edges. We investigated, also, the cross-section of nanocomposite films, in combination with EDS spectroscopy to correlate the images obtained with the nature of the occurring materials, before (Fig. 4, c) and after (Fig. 4, d) thermal annealing. Results of the analysis of SEM cross section images, in combination with EDS spectroscopy (insets in c and d), confirm that after thermal annealing the overall result is a flatter and thinner coating, almost similar to 'all-graphene' one, with more compacted GnPs. For films made by 10 layers, for example, with GnPs concentration of 60 wt.% the thicknesses of the coating before and after thermal annealing, pass respectively from $26 \pm 2\ \mu m$ to $4 \pm 2\ \mu m$. Similar results were obtained at the others graphene nanoplatelets concentrations.

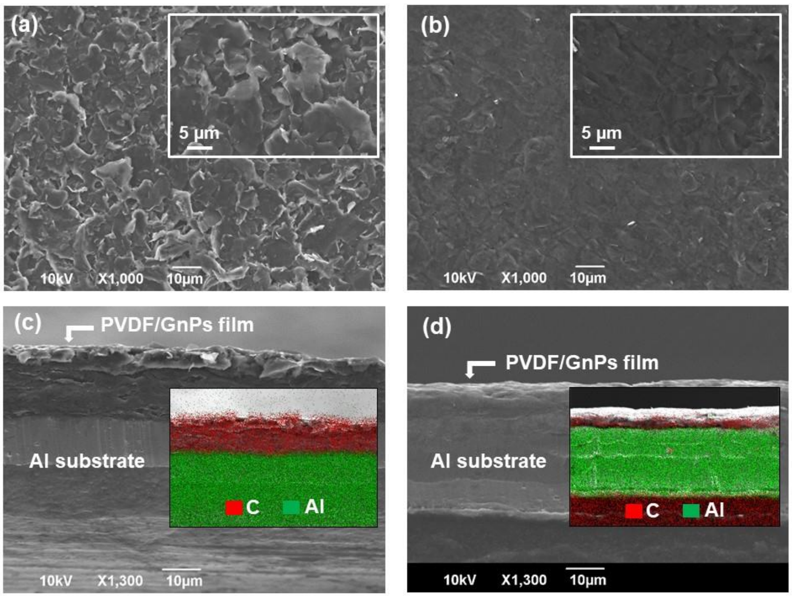

Fig. 4. SEM images of PVDF/60 wt.% of GnPs nanocomposite films with 10 layers before and after thermal annealing. The images were taken at 1000× magnification (a,b). The insets in (a) and (b) are the SEM images taken at 3000× magnification. (c,d) Cross section SEM images of PVDF/60 wt.% of GnPs nanocomposite films with 10 layers before and after 10 minutes of thermal annealing at 150°C respectively at 1300× magnification. The insets in (c) and (d) are the EDX atomic signals of carbon and aluminum.

Fig. 5 shows the EDX spectra of the cross sections of the nanocomposite films (the same cross sections shown in Fig. 4 c,d) with 10 layers and at 60 wt.% of graphene nanoparticles before (a) and after (b) thermal annealing. In both cases of pre and post thermal annealing, we found four distinct peaks at 0.277 keV, 0.530 keV, 0.688 keV and at 1.509 keV representing carbon, oxygen, fluorine and aluminum, respectively. In addition, we detected that after thermal annealing EDX analysis shows lower peak intensities especially for carbon (C-peak), contained in graphene nanoplatelets, and fluorine (F-peak), contained in PVFD polymer matrix. Change of intensity of such peaks can be attributed to the depth of distribution of the corresponding atoms [38, 39]. Before thermal annealing carbon and fluorine atoms, diffuse towards the aluminum surface, showing a higher

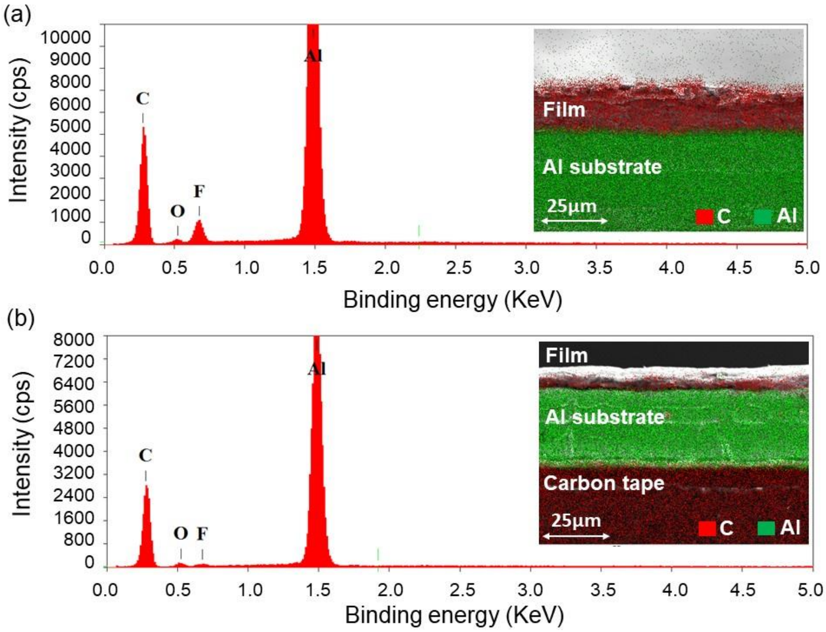

Fig. 5. EDX spectra of the same cross sections of nanocomposite films shown in Fig.3 c and d, containing 60 wt.% of graphene nanoparticles, on aluminum substrates before (a) and after (b) thermal annealing. Insets in (a) and (b) show EDX images of the corresponding samples before and after thermal annealing, respectively (these are the same of the insets shown in Fig.3 c and d).

intensity of C-peak and F-peak in EDX spectrum. On the contrary, after thermal annealing, it’s clearly visible that hot pressing compresses the graphene-based nanocomposite films and so, the carbon and fluorine atoms diffuse through the nanocomposite film resulting in a thinner coating, almost similar to ‘all-graphene nanoplatelets' film, with more compacted and closer GnPs, and with fluorine atoms distributed on its bottom. Due to these reasons the intensity of the C and F peaks decrease without altering the number of the corresponding atoms.

6.3.2 Surface topography analysis of nanocomposite films

Fig. 6 shows the arithmetic mean surface roughness S_a values obtained for nanocomposite films on Al-T1 substrates with 3 (a), 7 (d) and 10 (g) layers as a function of amount of graphene nanoplatelets before and after thermal annealing. Before thermal annealing S_a of the films, comparing films with the same number of layers, tends to increase with GnP wt.%: for example for films made by 3 layers the S_a values pass respectively from 0.60 ± 0.01 µm in the case of 10 wt.% of GnPs to 1.72 ± 0.10 µm for a GnPs concentration of 60 wt.%. At the lowest concentration of graphene nanoplatelets of 10 wt.%, S_a is independent from number of layers; on the contrary at the higher GnPs concentration of 40-60 wt.%, S_a tends to decrease with the increase of the number of layers (see Fig. 6, b, e, h) as a result of the higher content of nanoparticles which are therefore more compacted making the nanocomposite surface less rough. After thermal annealing the roughness of coatings changes: in particular hot pressing smooths out the surface by aligning the more compacted and closer GnPs along the air interface reducing the surface roughness of the fabricated coatings. In this case, the lower S_a of all PVDF/GnPs nanocomposite films remains substantially constant especially at lower concentrations of GnPs in the range 10-40 wt.% and at lower numbers of layers up to 7 layers: in fact, for example, for film with GnPs concentration of 40 wt.% the S_a values pass respectively from 0.41 ± 0.01 µm in the case of 3 layers (Fig. 6, c) to 0.40 ± 0.03 µm in the case of 7 layers (Fig. 6, f).

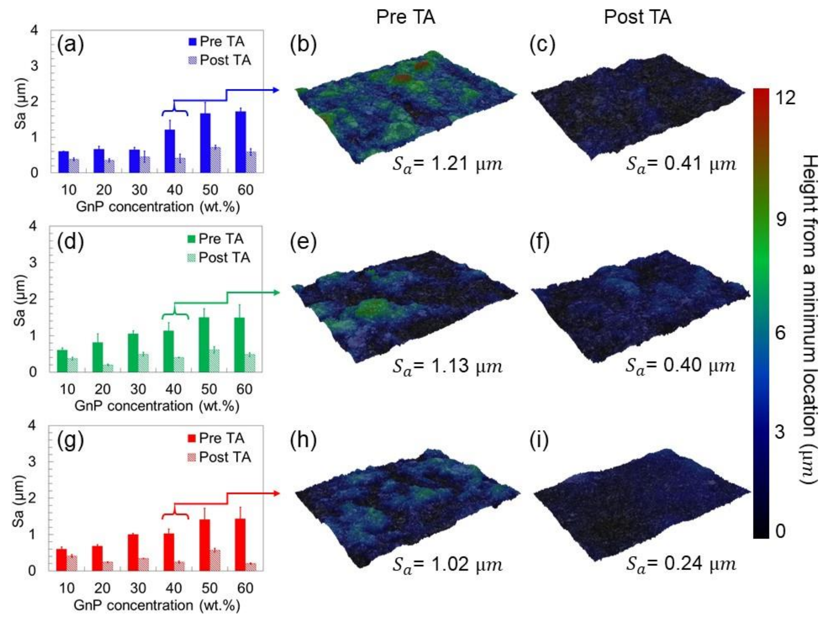

Fig. 6. Arithmetic mean surface roughness S_a values obtained for nanocomposite films with 3 (a), 7 (d) and 10 (g) layers as a function of amount of graphene nanoplatelets before and after 10 minutes of thermal annealing (TA) at 150°C. 3D Optical profilometer topography: 3D surface images of PVDF/40 wt.% of GnPs nanocomposite films with 3 (b,c), 7 (e,f) and 10 (h,i) layers before and after thermal annealing (TA) respectively. Different colors indicate the height (μm)from a minimum location.

On the contrary, there are modest variations in skewness and kurtosis in the nanocomposite film surfaces after thermal annealing. Tables 2-4 summarize the surface properties, in terms of skewness S_{sk} and kurtosis S_{ku}, of nanocomposite films with 3, 7 and 10 layers respectively, deposited on Al-T1 substrates before and after thermal annealing. It’s clearly that after thermal annealing there aren’t any significant changes in the distribution of height and shape of peaks and valleys across the nanocomposite surface. Calculated skewness (close to 0.0) and kurtosis (close to 3.0) of all PVDF/GnPs nanocomposite films, in fact, remain substantially constant, within standard deviation limits, at all concentrations of GnPs in the range 10-60 wt.% and at all numbers of layers: in particular, the absolute values of skewness are lower than 1 in all cases and kurtosis is higher than 2.9 and lower than 4.

Table 2. Skewness S_{sk} and kurtosis S_{ku} values for nanocomposite films with 3 layers, at all graphene nanoplatelets concentrations and before and after thermal annealing.

GnP wt.%	$\boldsymbol{S_{sk}}$ **Pre TA**	$\boldsymbol{S_{sk}}$ **Post TA**	$\boldsymbol{S_{ku}}$ **Pre TA**	$\boldsymbol{S_{ku}}$ **Post TA**
10	0.34±0.03	0.38±0.04	3.03±0.09	2.93±0.17
20	0.31±0.08	0.08±0.22	3.76±0.76	3.11±0.35
30	0.32±0.06	0.07±0.24	3.26±0.66	3.01±0.38
40	0.16±0.32	0.07±0.04	2.95±0.23	2.91±0.25
50	0.73±0.59	0.16±0.51	3.96±0.56	3.21±0.60
60	0.47±0.01	0.46±0.14	3.07±0.21	3.23±0.57

Table 3. Skewness S_{sk} and kurtosis S_{ku} values for nanocomposite films with 7 layers, at all graphene nanoplatelets concentrations and before and after thermal annealing.

GnP wt.%	$\boldsymbol{S_{sk}}$ Pre TA	$\boldsymbol{S_{sk}}$ Post TA	$\boldsymbol{S_{ku}}$ Pre TA	$\boldsymbol{S_{ku}}$ Post TA
10	0.26±0.45	0.15±0.22	3.71±0.19	2.93±0.17
20	0.28±0.57	0.66±0.14	3.45±0.39	2.96±0.03
30	0.24±0.27	0.63±0.24	3.44±0.20	3.42±0.38
40	0.18±0.25	0.10±0.25	2.97±0.35	3.01±0.40
50	0.27±0.59	0.40±0.59	3.01±0.38	3.57±0.24
60	0.44±0.02	0.10±0.58	3.12±0.53	2.91±0.17

Table 4. Skewness S_{sk} and kurtosis S_{ku} values for nanocomposite films with 10 layers, at all graphene nanoplatelets concentrations and before and after thermal annealing.

GnP wt.%	$\boldsymbol{S_{sk}}$ Pre TA	$\boldsymbol{S_{sk}}$ Post TA	$\boldsymbol{S_{ku}}$ Pre TA	$\boldsymbol{S_{ku}}$ Post TA
10	0.19±0.26	0.34±0.16	3.23±0.26	2.94±0.17
20	0.04±0.23	-0.06±0.04	2.96±0.11	3.42±0.05
30	0.56±0.15	0.35±0.44	2.98±0.15	3.19±0.53
40	-0.23±0.13	-0.01±0.47	2.93±0.15	3.05±0.14
50	0.30±0.23	0.17±0.47	2.97±0.11	2.95±0.09
60	0.41±0.29	0.58±0.50	2.93±0.33	3.94±0.09

6.3.3 Surface hydrophobicity analysis of nanocomposite films

The water contact angle analysis was conducted with the aim to investigate the surface hydrophobicity of the PVDF/GnPs nanocomposite films on Al-T1 substrates, and how this property is affected by thermal annealing. Fig. 7 (b) compares the water contact angle (WCA) values for the nanocomposite films made by 3, 7 and 10 layers at GnPs concentration in the range 10-60 wt.% before and after thermal annealing. The measured WCA of neat PVDF is of 82.6° ± 1.2°. The presence of graphene nanoplatelets increases the value of the contact angle at the nanocomposite surface, and the value tends to increase as the concentration of GnPs and the number of layers become respectively higher and lower. Before thermal annealing, the average WCA values at different loadings (10-60 wt.%) are in the range of 93.1° - 128.0° with standard deviations in the range of 0.9° - 2.0°. After thermal annealing, the contact angle of all PVDF/GNPs nanocomposite films decreases and remains substantially constant within the number of layers especially at higher concentrations of GnPs in the range 30-60 wt.%: for example at 50 wt.% for films made by 3 layers the water contact angle values, before and after thermal annealing, pass respectively from 125 ± 2.0° to 102 ± 1.3°. The above results from the water contact angle analysis can be explained by considering the changes in surface roughness of the nanocomposite films after thermal annealing: in fact, results in Fig. 6 confirm that after thermal annealing the surface roughness of the engineered films is lower and so it leads to a lower WCAs for all GnPs concentrations and all number of layers. Fig. 7 (c) shows the spreading kinetics of WCAs on nanocomposite films with 3 layers at 10-60 GnPs wt.% as a function of time before and after thermal annealing. In all cases, the water contact angle on all nanocomposite surfaces does not vary significantly after approximately 1 min. In addition, the results obtained show that, for all films, the rate of spread of pure water droplets with time is higher within 12 seconds especially before thermal annealing and at the highest GnPs concentration in the range 40-60 wt.% characterized by larger water contact angle values.

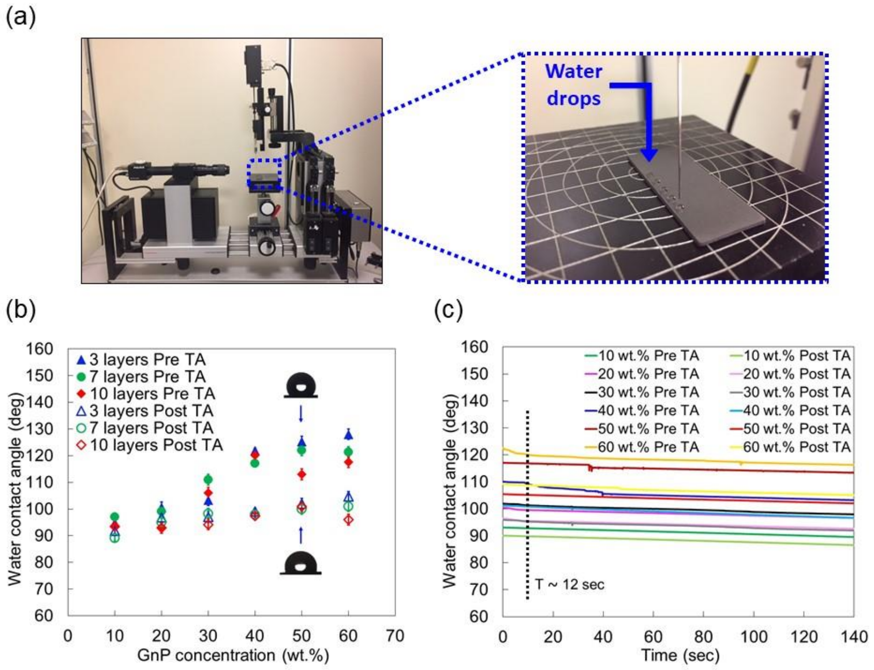

Fig. 7. (a) DataPhysics OCA 20 used for WCAs measurements with a view of a nanocomposite film on Al-T1 substrate during water drops deposition. (b) Water contact angle values at equilibrium on PVDF/GnPs nanocomposite films with 3, 7 and 10 layers, at different nanoplatelets loading, before and after 10 minutes of thermal annealing (TA) at 150°C. (c) Spreading kinetics of water contact angle values on PVDF/GnPs nanocomposite films with 3 layers as a function of time, at nanoplatelet loading in the range 10-60 wt.%, before and after thermal annealing (TA).

6.3.5 Thermal measurements analysis

Fig. 8 shows the thermal conductivity variation values ($\Delta\lambda$*) of all nanocomposite films deposited on Al-T1 substrates at all concentrations of graphene nanoplatelets as a function of the number of layers of the film before and after thermal annealing. The measured thermal conductivity (λ_0) and effusivity (ε_0) of PVDF polymer film coated on aluminum surface without graphene nanoplatelets are constant and equal to 1.7±0.1 W/mK and 1834.0±10.2 Ws$^{1/2}$/m^{2}K respectively. After the addition of graphene nanoplatelets, thermal conductivity of the samples increases of one order of magnitude almost better than PVDF polymer film coated on aluminum surface samples. Before thermal annealing $\Delta\lambda$* tends to decrease with the increase of the number of layers as a consequence of a non-uniform interface between layers and between the different materials, namely PVDF polymer matrix and graphene nanoplatelets, which leads to an higher total porosity of the nanocomposite film and so to a lower thermal conductivity [40, 41]. In all cases the measured thermal conductivity λ increases after thermal annealing especially for those films with the higher GnPs concentration, and so the thermal conductivity variation $\Delta\lambda$* becomes higher.

Fig. 9 shows the $\Delta\lambda*_{normalized}$ (a), $\Delta\varepsilon*_{normalized}$ (b) and $\Delta\alpha*_{normalized}$ (c) values of all nanocomposite films with layers in the range 3-10 as a function of graphene nanoplatelets concentration after thermal annealing. Results obtained show that normalized thermal conductivity of all nanocomposite samples, tends to increase with increasing of GnPs concentrations especially up to 50 wt.% and it remains substantially constant with the increase of layers. In fact, for example, such increase of the $\Delta\lambda*_{normalized}$ was of 758.8% and 752.9% for films with 3 and 10 layers respectively at 50 wt.% of graphene nanoplatelets after 10 minutes of thermal annealing at 150°C. On the contrary, normalized thermal effusivity and diffusivity changes, after thermal annealing, show a modest increase, after the addition of graphene nanoplatelets, of 238.0% and 167.6% respectively, for films with 3 layers at GnPs concentration of 50 wt.% and their increase is almost constant with the increasing graphene nanoplatelets content.

Increasing of thermal conductivity of the nanocomposite films after hot pressing, can be explained by considering that nanocomposite films with higher GnPs concentrations have a higher content of compacted and closer nanoparticles in the polymer matrix resulting essentially in all graphene-based films. In fact, results in Fig. 4, confirm that after thermal annealing the nanocomposite films show smoothed edges of graphene nanoplatelets, so closer nanoparticles are more evident, and it is clearly visible the reduction of the film thickness after hot pressing leading to the formation of almost similar to the more compacted 'all-graphene' film. For that reason, the thermal pathways increase, the total porosity of the films decreases, the interfacial thermal resistance (ITR) between polymer matrix and GnPs becomes lower and the thermal contact resistance at sensor-film interface reduces as a result of a reduced surface roughness of the nanocomposite films as shown in Fig. 3.

The thermal annealed nanocomposite films were placed into a condensation test chamber, to assess their condensation heat transfer performances. Dropwise condensation (DWC) was observed in all nanocomposite films and preliminary heat transfer coefficient measurements showed a modest increase of the values, respect to the case of the hydrophilic filmwise uncoated sample.

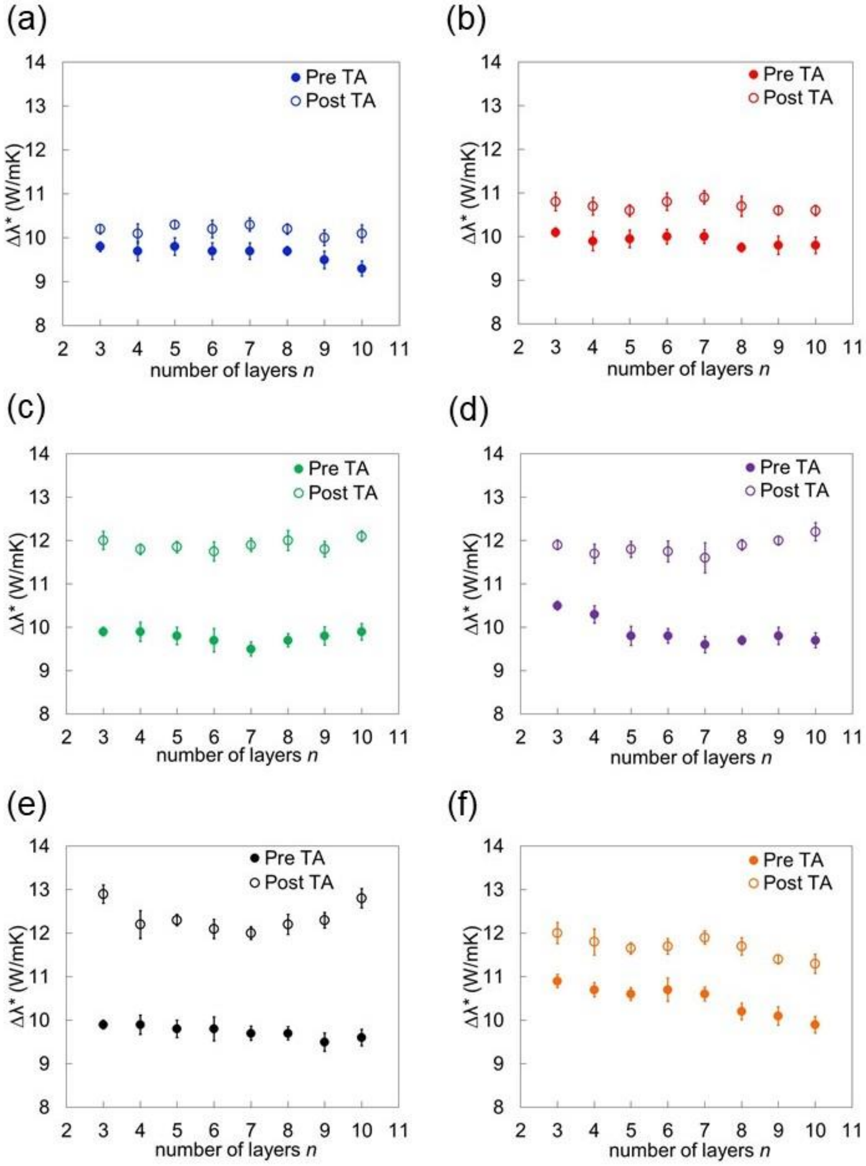

Fig. 8. Thermal conductivity *Δλ** variation values obtained for all nanocomposite films with different amount of graphene nanoplatelets as a function of number of layers of the films before and after 10 minutes of thermal annealing (TA) at 150°C: (a,b) filler content 10 and 20 wt.% respectively ;(c,d) filler content 30 and 40 wt.% respectively; (e,f) filler content 50 and 60 wt.% respectively.

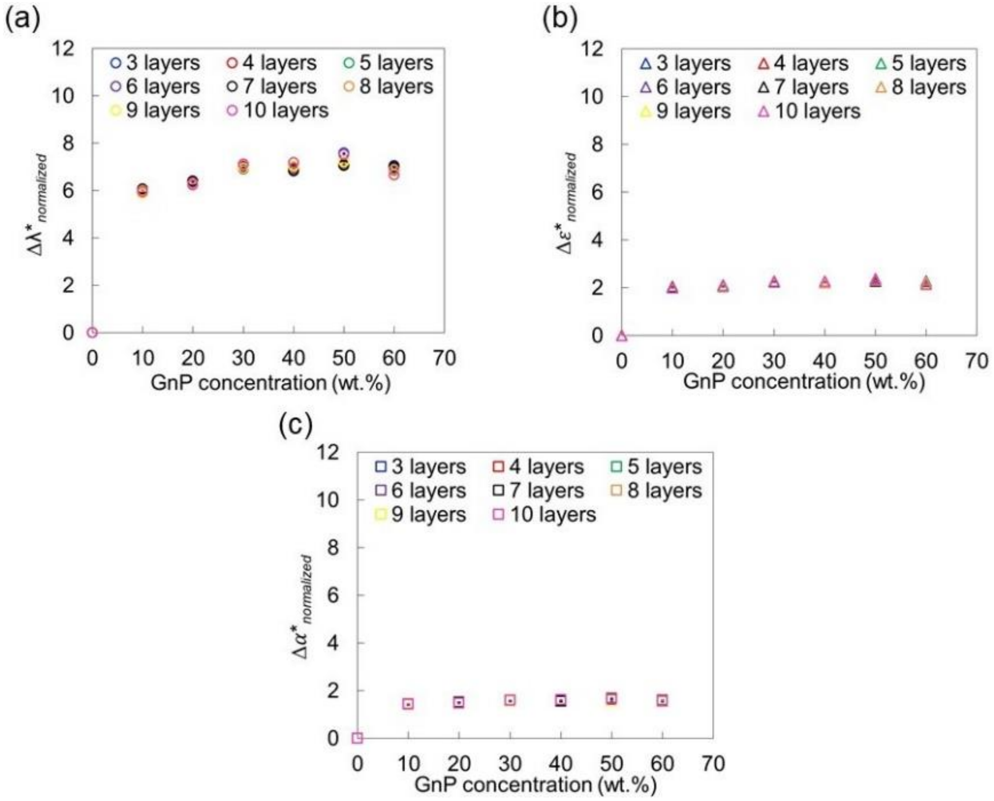

Fig. 9. $\Delta\lambda^*_{normalized}$ (a), $\Delta\varepsilon^*_{normalized}$ (b), $\Delta\alpha^*_{normalized}$ (c) values of PVDF/GnPs films after 10 minutes of thermal annealing at 150°C as a function of the number of graphene nanoplatelets (10, 20, 30, 40, 50 and 60 wt.%) and for all number of layers.

6.4 Conclusions

In conclusion, we developed multi-layered nanocomposite films by spray coating the formulated graphene-based polymer conductive inks on textured aluminum substrates, at different graphene nanoplatelets loadings. These films were thermal annealed, resulting essentially in ‘all-graphene’ films, and their morphological, topographic, hydrophobic and thermal responses were investigated.

The fabricated nanocomposite surfaces exhibit a decrease of the roughness and the water static contact angle after hot pressing: in particular we obtained mean surface roughnesses lower than 1 μm and SCA greater than 90°, showing that thermal annealing does not affect the hydrophobic nature of all nanocomposite surfaces on textured aluminum substrate. On the contrary, thermal annealing, does not affect the surface features of the fabricated nanocomposite films: in fact, they remain substantially nearly symmetric with S_{sk} close to 0.0 and nearly Gaussian with S_{ku} close to 3.0.

Moreover, thermal properties of the developed nanocomposite films were evaluated in terms of thermal conductivity, effusivity and diffusivity changes. We detected that their thermal conductivity increases up to ~ 759% after hot pressing and with increasing of graphene nanoplatelets especially up to 50 wt.% concentration: in particular we obtained that, after thermal annealing, the through-plane thermal conductivity of the nanocomposite films with 3 layers at GnPs loading of 50 wt.% is around ~14.7 W/mK, with an increase of thermal effusivity and diffusivity of 238.0% and 167.6% respectively.

6.5 References

[1] Lee C, Wei X, Kysar JW, Hone J. Measurement of the elastic properties and intrinsic strength of monolayer graphene. science 2008;321:385-8.

[2] Aliofkhazraei M, Ali N, Milne WI, Ozkan CS, Mitura S, Gervasoni JL. Graphene science handbook: electrical and optical properties: CRC press; 2016.

[3] Novoselov KS, Geim AK, Morozov SV, Jiang D, Zhang Y, Dubonos SV, et al. Electric field effect in atomically thin carbon films. science 2004;306:666-9.

[4] Balandin AA, Ghosh S, Bao W, Calizo I, Teweldebrhan D, Miao F, et al. Superior thermal conductivity of single-layer graphene. Nano letters 2008;8:902-7.

[5] Balandin AA. Thermal properties of graphene and nanostructured carbon materials. Nature materials 2011;10:569.

[6] Stankovich S, Dikin DA, Dommett GH, Kohlhaas KM, Zimney EJ, Stach EA, et al. Graphene-based composite materials. nature 2006;442:282.

[7] Rafiee MA, Rafiee J, Wang Z, Song H, Yu Z-Z, Koratkar N. Enhanced mechanical properties of nanocomposites at low graphene content. ACS nano 2009;3:3884-90.

[8] Kuilla T, Bhadra S, Yao D, Kim NH, Bose S, Lee JH. Recent advances in graphene based polymer composites. Progress in polymer science 2010;35:1350-75.

[9] Ansari S, Giannelis EP. Functionalized graphene sheet—Poly (vinylidene fluoride) conductive nanocomposites. Journal of Polymer Science Part B: Polymer Physics 2009;47:888-97.

[10] Rahman MA, Chung G-S. Synthesis of PVDF-graphene nanocomposites and their properties. Journal of Alloys and Compounds 2013;581:724-30.

[11] Pop E. Energy dissipation and transport in nanoscale devices. Nano Research 2010;3:147-69.

[12] Tiwari S, Singh AK, Prakash R. Poly (3-hexylthiophene)(P3HT)/graphene nanocomposite material based organic field effect transistor with enhanced mobility. Journal of nanoscience and nanotechnology 2014;14:2823-8.

[13] Kim BJ, Lee S-K, Kang MS, Ahn J-H, Cho JH. Coplanar-gate transparent graphene transistors and inverters on plastic. Acs Nano 2012;6:8646-51.

[14] Eda G, Chhowalla M. Graphene-based composite thin films for electronics. Nano Letters 2009;9:814-8.

[15] Bauld R, Choi D-YW, Bazylewski P, Divigalpitiya R, Fanchini G. Thermo-optical characterization and thermal properties of graphene–polymer composites: a review. Journal of Materials Chemistry C 2018;6:2901-14.

[16] Zahid M, Masood MT, Athanassiou A, Bayer IS. Sustainable thermal interface materials from recycled cotton textiles and graphene nanoplatelets. Applied Physics Letters 2018;113:044103.

[17] Karthick K, Joy GC, Suresh S, Dhanuskodi R. Impact of Thermal Interface Materials for Thermoelectric Generator Systems. Journal of Electronic Materials 2018;47:5763-72.

[18] Marconnet AM, Yamamoto N, Panzer MA, Wardle BL, Goodson KE. Thermal conduction in aligned carbon nanotube–polymer nanocomposites with high packing density. ACS nano 2011;5:4818-25.

[19] Munakata N, Makita K, Bolsée D, Gillotay D, Horneck G. Spore dosimetry of solar UV radiation: applications to monitoring of daily irradiance and personal exposure. Advances in Space Research 2000;26:1995-2003.

[20] Clausi M, Santonicola MG, Schirone L, Laurenzi S. Analysis of ultraviolet exposure effects on the surface properties of epoxy/graphene nanocomposite films on Mylar substrate. Acta Astronautica 2017;134:307-13.

[21] Micheli D, Apollo C, Pastore R, Morles RB, Laurenzi S, Marchetti M. Nanostructured composite materials for electromagnetic interference shielding applications. Acta Astronautica 2011;69:747-57.

[22] Smith Jr JG, Delozier DM, Connell JW, Watson KA. Carbon nanotube-conductive additive-space durable polymer nanocomposite films for electrostatic charge dissipation. Polymer 2004;45:6133-42.

[23] Ramalingame R, Lakshmanan A, Müller F, Thomas U, Kanoun O. Highly sensitive capacitive pressure sensors for robotic applications based on carbon nanotubes and PDMS polymer nanocomposite. Journal of Sensors and Sensor Systems 2019;8:87-94.

[24] Bae S-H, Kahya O, Sharma BK, Kwon J, Cho HJ, Ozyilmaz B, et al. Graphene-P (VDF-TrFE) multilayer film for flexible applications. ACS nano 2013;7:3130-8.

[25] Kammoun M, Berg S, Ardebili H. Flexible thin-film battery based on graphene-oxide embedded in solid polymer electrolyte. Nanoscale 2015;7:17516-22.

[26] Zhang W, Jia B, Furumai H. Fabrication of graphene film composite electrochemical biosensor as a pre-screening algal toxin detection tool in the event of water contamination. Scientific reports 2018;8:10686.

[27] Shan C, Yang H, Han D, Zhang Q, Ivaska A, Niu L. Graphene/AuNPs/chitosan nanocomposites film for glucose biosensing. Biosensors and bioelectronics 2010;25:1070-4.

[28] Philip B, Abraham JK, Chandrasekhar A, Varadan VK. Carbon nanotube/PMMA composite thin films for gas-sensing applications. Smart materials and structures 2003;12:935.

[29] Lobotka P, Kunzo P, Kovacova E, Vavra I, Krizanova Z, Smatko V, et al. Thin polyaniline and polyaniline/carbon nanocomposite films for gas sensing. Thin Solid Films 2011;519:4123-7.

[30] Romano MS, Li N, Antiohos D, Razal JM, Nattestad A, Beirne S, et al. Carbon nanotube–reduced graphene oxide composites for thermal energy harvesting applications. Advanced materials 2013;25:6602-6.

[31] Wang Y, Tang B, Zhang S. Single-walled carbon nanotube/phase change material composites: sunlight-driven, reversible, form-stable phase transitions for solar thermal energy storage. Advanced Functional Materials 2013;23:4354-60.

[32] Wang W, Tang B, Ju B, Gao Z, Xiu J, Zhang S. Fe 3 O 4-functionalized graphene nanosheet embedded phase change material composites: efficient magnetic-and sunlight-driven energy conversion and storage. Journal of Materials Chemistry A 2017;5:958-68.

[33] Rahman MA, Lee B-C, Phan D-T, Chung G-S. Fabrication and characterization of highly efficient flexible energy harvesters using PVDF–graphene nanocomposites. Smart Materials and Structures 2013;22:085017.

[34] Li Q, Flamant G, Yuan X, Neveu P, Luo L. Compact heat exchangers: A review and future applications for a new generation of high temperature solar receivers. Renewable and Sustainable Energy Reviews 2011;15:4855-75.

[35] Kim M-H, Bullard CW. Air-side thermal hydraulic performance of multi-louvered fin aluminum heat exchangers. International Journal of Refrigeration 2002;25:390-400.

[36] Hesselgreaves JE, Law R, Reay D. Compact heat exchangers: selection, design and operation: Butterworth-Heinemann; 2016.

[37] Thompson CV. Solid-state dewetting of thin films. Annual Review of Materials Research 2012;42:399-434.

[38] Powell CJ, Jablonski A. Progress in quantitative surface analysis by X-ray photoelectron spectroscopy: Current status and perspectives. Journal of Electron Spectroscopy and Related Phenomena 2010;178:331-46.

[39] Tougaard S. Energy loss in XPS: Fundamental processes and applications for quantification, non-destructive depth profiling and 3D imaging. Journal of Electron Spectroscopy and Related Phenomena 2010;178:128-53.

[40] Shtein M, Nadiv R, Buzaglo M, Kahil K, Regev O. Thermally conductive graphene-polymer composites: size, percolation, and synergy effects. Chemistry of Materials 2015;27:2100-6.

[41] Li Q, Guo Y, Li W, Qiu S, Zhu C, Wei X, et al. Ultrahigh thermal conductivity of assembled aligned multilayer graphene/epoxy composite. Chemistry of Materials 2014;26:4459-65.

Chapter 7 - Conclusions

7.1 Conclusions

The main objective of my Ph.D. research was the design and manufacturing of multifunctional nanocomposite films on different types of substrates, namely Mylar membranes, carbon-fiber/reinforced epoxy composite laminates (CFRP) and metal substrates, which are typically used in the aerospace field, with controlled thermal, electrical, morphological and hydrophobic characteristics while maintaining the features of the different substrates. Such multifunctional coatings were fabricated on one side with the aim to protect and safeguard the various spacecraft components, of different nature, from the surrounding hostile space environment, especially from ultraviolet radiations in C band (UV-C) and electrically charged particles coming from space-plasma, and on the other side to achieve thermal performance of the unit increased over time, by increasing the heat transfer coefficients, resulting in an ideal design of heat exchangers widely used in the aerospace field to control, for example, the temperature of on-board electronic components.

In this research, I focused on the development of nanocomposite films, containing carbon nanoparticles, namely carbon nanotubes (SWNT and MWNT) and graphene nanoplatelets (GnPs) with different geometrical features and functionalizations, which have unique electrical, thermal and mechanical properties, dispersed in different types of polymeric matrices, both aerospace-grade thermosetting and thermoplastic ones.

Preliminarily, the dispersion of nanofillers in the polymer matrix was strongly investigated as it is an important issue that greatly affects the quality of desired multifunctional properties and the outcome of the manufacturing process of nanocomposites. The role of nanoparticles geometry, their interaction with the polymeric matrix and the alignment of the nanofillers in the matrix and their functionalization and concentration in the polymer blend were so assessed.

Different deposition processes of the fabricated nanocomposite films were investigated, in order to expand upon the current research, and optimized as a function of the nature of nanocomposite blends, the substrates used and of the expected range (sufficiently large scale) to be useful for satellite applications.

In particular, the results from my PhD research can be summarized as follows:

1. Analysis of UV-C effects on the surface properties of epoxy/graphene nanocomposite films on Mylar substrate

The main objective of this work is to investigate the effects of space-abundant UV-C radiation on carbon-based nanocomposite films deposited on flexible Mylar substrates, which are already widely used in spacecraft sub-systems as MLI, Gossamer structures etc. It’s well-known, in fact, that polymer-based materials in space exhibit larger degradation effects due to the combination of energetic UV radiations, vacuum, atomic oxygen, as well as large temperature gradients, which degrade their electrical, optical and thermal properties. The possibility to apply carbon-based nanocomposite coatings on such polymeric membranes is currently investigated with the aim to protect the surfaces, by exploiting the excellent properties of carbon nanomaterials, by space environmental exposure, including UV radiations.

Epoxy/graphene nanocomposite films were fabricated by spin-coating process using Mylar as substrate and the effects of UV-C radiation on the surface properties were investigated in terms of wettability and electrical properties. Preliminary, the spin-coating process was investigated in order to set specific parameters to prepare homogeneous and uniform polymeric films. In particular, three different grades of xGnPs were used for the film fabrication at different loadings by weight. It was observed that the wettability of the nanocomposite films increases when adding the graphene nanoplatelets for all grades of xGnP. After exposure to UV-C, the average water contact angle of the irradiated nanocomposite films depends on the geometrical characteristics of the nano-reinforcement. In the case of the thinner graphene nanoplatelets (xGnP-C750), the WCA values remain almost constant even after 9 hours of UV-C exposure. On the contrary, in case of the thicker graphene nanoplatelets (grades M5 and H5), it was observed that the water contact angle at equilibrium increases after 9 hours of UV-C exposure, and the difference becomes larger as the thickness of graphene flakes increases. These results show that the hydrophobic nature, which is a relevant parameter to assess the level of moisture absorption by the films, of the epoxy/graphene nanocomposite films tends to increase after exposure to UV-C radiation.

When looking at the electrical properties of the nanocomposite films, the surface electrical resistivity decreases with the increasing of nanofiller loadings, as it would be expected, and also during exposure to the UV-C radiation. This latter effect is more significant for films with lower concentration of graphene nanoplatelets, whereas films at 7 wt.% loading of xGnPs (all three types tested in this work) show the lowest variation of electrical resistance over the UV-C exposure. This phenomenon can be related to the higher content of polymer, for the nanocomposites at lower concentration of xGnPs, as the polymer matrix erosion contributes to create a more conductive surface due to the exposure of graphene nanoplatelets. Results from the electrical impedance spectroscopy experiments showed that the surface resistivity decreases with the testing frequency following a linear trend both before and after radiation exposure, and that this behavior is common for all nanocomposite films. Further, the surface resistivity of the films after UV-C irradiation is always smaller than that before exposure regardless of the xGnP size, confirming that the dominant effect of the UV-C radiation is a selective polymer matrix erosion that gives rise to an increase of the electrical conductivity at the film surface.

2. Spray coating process of MWCNT/epoxy nanocomposite films on Mylar membranes for aerospace applications: effects of process parameters on surface electrical properties

The main objective of this research is to study the spray-coating deposition process and to investigate the role of its working parameters in setting the morphology and the electrical performance of MWCNT-based nanocomposite films on flexible Mylar. The spray-coating technique, as opposed to the previous used spin-coating one, allows to fabricate larger polymeric coatings in terms of covered area on planar and not substrates, becoming an attractive method for large scale production of coatings. The quality, in terms of uniformity and homogeneity properties, of the final coatings fabricated and its thicknesses are controlled by varying the feeding rate, the applied pressure, the spraying distance, the spraying time, the direction of the spraying, the nozzle diameter of the aerograph as well as the composition and so the viscosity of the sprayed mixture. In particular, the fabrication of uniformly electrically-conductive coatings on Mylar substrate can allow the mitigation of plasma-induced charging that is a problem related to the dielectric nature of MLI, including Mylar, which are a serious risk for the spacecraft operation and integrity.

In this work, carbon nanocomposite films were fabricated by spray coating blends of MWCNTs dispersed in thermosetting epoxy resin onto a Mylar substrate. The nanocomposite films were fabricated using two different nozzle diameters, and the role of the process parameters and filler concentration on the thickness and electrical properties of the spray -coated films were investigated. We observed that larger covered areas were obtained using the nozzle with diameter of 1.5 mm at lower viscosity values of the nanocomposite blends (MWCNT concentration of 0.5 wt.% and 1 wt.%) and at lower nozzle-to-target distance of 10 cm. The surface electrical properties of the nano-reinforced epoxy films on Mylar were determined at different locations in order to investigate their uniform distribution. Results showed that a uniform surface conductivity can be achieved in nanocomposite films processed with the larger nozzle, at intermediate concentrations of MWCNT (1 wt%), and at target distance of 15 cm. In general, at higher concentrations of carbon nanotubes, the increase in blend viscosity, which is due to entanglement and surface interactions of the nanofillers, strongly limits the use of the spray coating process. This study gives insight into the manufacturing process of electrically-conductive nanocomposite films on Mylar substrate using spray coating and highlights the most favorable conditions and bottlenecks at the level of process parameters and blend composition, namely the loading of MWCNTs. The analysis of the electrical properties of the processed films at different locations of the spray-covered area revealed what parameters are most relevant and need to be considered in the manufacturing process of these films, in order to optimize their properties for aerospace applications.

Electrical results show that the fabricated coatings on Mylar membranes respect NASA requirements for thin material to control and minimize ESC charging for which the electrical resistivity $\rho_s < 10^{+08}$ Ω/square is needed.

3. Design of nanocomposite coatings by bar-coating process on CFRP structures for electrostatic charging mitigation for spacecraft[1]

The main purpose of this study was to exploit the well-known superior electrical properties of the carbon nanoparticles to fabricate nanocomposite coatings with improved performance, with the aim to mitigate the degradative effects caused by space plasma that can induce surfaces charging and so cause permanently physical damages and biasing of instruments to the on-board structural and electronic components respectively of the spacecraft. NASA plasma environment effects design guidelines are, in fact, that it should make all external surfaces at least partially conductive to minimize ESC buid-up and ground all conductive elements to a common ground to minimize potential differences on spacecraft as well.

---

[1] Work in collaboration with Thales Alenia Space, Domain Exploration & Science – Engineering and Advanced Studies, Turin, Italy

In this study, I investigated the thermal and electrical properties of different carbon-based nanocomposite films, hybrid and not, deposited on carbon fiber/epoxy resin composite laminates (CFRP), typically employed in the aerospace structures, by bar-coating process. In this work, bar-coating technique was used to fabricate larger polymeric coatings due to the high viscosity nature of the aerospace-grade structural adhesives used as matrices becoming an attractive method for industrial production of coatings. The effects of carbon nanoparticles on the cure reaction, glass transition temperature and thermal stability of the nanocomposite films fabricated were investigated with DSC and TGA. DSC analysis shows that the introduction of nanoparticles in the polymer matrix leads to an increasing of enthalpies of reaction, cure peak temperature and of glass transition temperature. Moreover, the addition of carbon nanoparticles decreases the thermal stability of the epoxy polymer matrix for all classes of nanocomposites fabricated as shown in TGA results.

These films were exposed to UV-C radiation, humidity and thermal cycles and their electrical response, in terms of surface and volume conductivity, was investigated. Comparing the volume conductivity values obtained at the lower frequencies up to 100 MHz, we detected that only the nanocomposite film, at higher concentration of nanoparticles (namely hybrid C2 sample: Epoxy EA9396/3wt.% of SWNTs + 1 wt.% of GnPs), exhibits a modest increasing of the volume conductivity upon high level of humidity of 75% due to the fact that water molecules allow to the SWNTs to become n-type semiconductors. On the contrary, after UV-C irradiation and after thermal cycle, any changes of volume conductivities were detected at those lower frequencies. For the others nanocomposite films, with a lower content of nanoparticles, I didn't detect any changes in the volume conductivity after UV-C irradiation and after thermal and humidity tests. At higher frequencies, no relevant changes in the volume conductive values, for all nanocomposite films, were detected after all tests except for the nanocomposite sample C2, which shows an electrical volume conductivity increased of one order of magnitude upon UV-C irradiation due to the erosion of the resin induced by UC-C rays, making the nanocomposite surfaces more conductive.

On the other hand, no significant changes in the surface resistivity and conductivity, are detected after all aging tests on all nanocomposite films fabricated.

It was found that, the fabricated coatings respect NASA requirements for thin material to control and minimize ESC charging for which the electrical resistivity $\rho_s < 10^{+08}$ Ω/square is needed.

Moreover, the nanocomposite films of type C1 (Epoxy EA9396/0.9 of SWNT) were deposited by bar coating process with eight different geometrical configurations on carbon epoxy composite laminate panel (CFRP), typically employed in satellite structures, to assess their use as potential innovative grounding system for spacecrafts, to replace, for example, the heavy and bulky common employed grounding rails in aluminum for satellite telecommunications. The choice of C1 is due for its lower absolute viscosity, due to the its lowest content of nanoparticles in the epoxy matrix, respect to the other types of nanocomposite blends allowing for easier deposition process and in the same time providing good electrical properties. Preliminary DC electrical measurements on all nanocomposite film configurations realized on ground plane CFRP, to assess their use as potential and innovative weight-volume saving grounding system for spacecrafts to mitigate space plasma-induced charging, showed that in particular, the fourth configuration of nanocomposite coatings fabricated on CFRP structure, represents the most promising one with the lowest DC electrical resistance R_{DC} of 100 ± 5 Ω.

4. Direct effects of UV irradiation on the developed graphene-based nanocomposite coating sensors on CFRP structures revealed by electrical resistance tomography (ERT)

The main goal of this research was to develop a carbon-based nanocomposite coating sensor to monitor and quantify the space abundant UV-C radiation absorbed by the composite structures or for example by the astronauts during their extra vehicular activities (EVA) in the space, by exploiting the here investigated great potential of electrical resistance tomography (ERT) technique for the *in situ* health monitoring of aerospace structures.

Electrical resistance tomography was used to investigate the changes of the surface electrical properties of UV-sensitive nanocomposite films upon exposure to UV-C radiation. The nanocomposite coatings were fabricated by integration of DNA-functionalized graphene nanoplatelets into a conductive polymer matrix made of PEDOT:PSS. The ERT technique was optimized in terms of current patterns and injection values in order to detect damage induced by UV irradiation, with the opposite injection pattern and currents of the order of 20-30 mA giving the most reliable outcome. Maps of conductivity changes for the irradiated films were reconstructed, with the developed code using open-source MATLAB-based software suite Electrical Impedance Tomography and Diffuse Optical Tomography Reconstruction Software (EIDORS), from the acquired differential voltage changes with respect to a baseline sample. The nanocomposite area exposed and affected by the UV-C radiation was localized in the ERT maps with good agreement. Different levels of conductivity changes were detected by the technique when exposing the surfaces to different intensities of UV-C radiation. These conductivity changes were verified using 2-electrode impedance spectroscopy. The results were supported by SEM morphology and Raman spectroscopy analyses. In particular, the GNP/DNA/PEDOT:PSS nanocomposite films face different stages of conductivity changes upon irradiation with UV-C light, with an initial drop of the electrical conductivity due to degradation of the conducting polymer matrix, and a subsequent increase related to DNA denaturation and progressive exposure of the GNP.

Both situations were captured in the reconstructed conductivity maps, highlighting ERT, applied on the designed nanocomposite sensor, as an effective technique and a potential real-time health monitoring method of materials and structures subject to degradation by UV-C radiation.

5. Hydrophobic multi-layered graphene-based nanocomposite coatings spray-coated on textured aluminum substrate with high thermal conductivity to improve the efficiency of thermal power generation[2]

The main idea of this research, is to fabricate hydrophobic and, in the same time, thermal conductive nanocomposite coatings applied on aluminum substrate that can reduce the filmwise (FWC) condensation phenomenon encouraging the dropwise (DWC) one, leading to much higher heat transfer coefficients and improving so the energy efficiency of heat pipes used in the aerospace sector, for example to control the temperature of on-board electronic components. Aluminum was chosen as substrate for the nanocomposite films as it is a metal largely used in aerospace sector, especially in the heat exchangers.

I developed multi-layered nanocomposite films by spray coating the formulated graphene-based polymer conductive inks on textured aluminum substrates, at different graphene nanoplatelets loadings. The fabricated nanocomposite surfaces exhibit a decrease of the roughness and the water static contact angle after hot pressing: in particular we obtained mean surface roughnesses lower than 1 μm and SCA greater than 90°, showing that thermal annealing does not affect the hydrophobic nature of all nanocomposite surfaces on textured aluminum substrate. On the contrary, thermal annealing, does not affect the surface features of the fabricated nanocomposite films: in fact, they remain substantially nearly symmetric with S_{sk} close to 0.0 and nearly Gaussian with S_{ku} close to 3.0.

---

[2] Work in collaboration with Italian Institute of Technology (IIT) under the supervision of Dr. Ilker S. Bayer. This work is part of a European project partnership [H2020 project (HARMoNIC – HierARchical Multiscale NanoInterfaces for enhanced Condensation processes; EU project Grant Agreement 801229)]

Moreover, thermal properties of the developed nanocomposite films were evaluated in terms of thermal conductivity, effusivity and diffusivity changes. We detected that their thermal conductivity increases up to ~ 759% after hot pressing and with increasing of graphene nanoplatelets especially up to 50 wt.% concentration: in particular we obtained that, after thermal annealing, the through-plane thermal conductivity of the nanocomposite films with 3 layers at GnPs loading of 50 wt.% is around ~14.7 W/mK, with an increase of thermal effusivity and diffusivity of 238.0% and 167.6% respectively.

The thermal annealed nanocomposite films were placed into a condensation test chamber, to assess their condensation heat transfer performances. Dropwise condensation was observed in all nanocomposite films and preliminary heat transfer coefficient measurements showed a modest increase of the values, respect to the case of the hydrophilic filmwise uncoated sample.